Bose-Einstein Condensation and Narrow-Line Photoassociation Spectroscopy of Calcium

Von der Fakultät für Mathematik und Physik der
Gottfried Wilhelm Leibniz Universität Hannover
zur Erlangung des Grades

Doktor der Naturwissenschaften
Dr. rer. nat.
genehmigte Dissertation
von

Dipl.-Phys. Oliver Appel
geboren am 12. November 1982 in Holzminden

2014

Referent: Prof. Dr. Wolfgang Ertmer

Korreferent: Prof. Dr. Fritz Riehle

Tag der Promotion: 11. November 2013

Kurzzusammenfassung

Im Rahmen dieser Arbeit wurden zwei wesentliche Fortschritte bei der Erforschung ultrakalter Calciumatome erzielt. Nach einer kurzen Beschreibung der experimentellen Grundlagen wird die erstmalige Realisierung eines Bose-Einstein-Kondensats von Erdalkaliatomen präsentiert. Aufgrund der Abwesenheit eines magnetischen Moments von ^{40}Ca-Grundzustandsatomen muss die Evaporation in einer optischen Dipolfalle durchgeführt werden. Hierbei galt es Schwierigkeiten wie die großen Dreikörperverluste, welche auch im Zuge dieser Arbeit untersucht wurden, zu überwinden.
Der zweite wesentliche Teil dieser Arbeit konzentriert sich auf die Untersuchung schmaler Photoassoziationsresonanzen nahe dem Interkombinationsübergang zwischen Singlett- und Triplettsystem. Vom 2-Atom-Zustand $^1S_0 + {}^1S_0$ kann in die beiden bindenden Molekülpotentiale $a^3\Sigma_u^+$ sowie $c^3\Pi_u$ angeregt werden, welche für größere Kernabstande in 1_u beziehungsweise 0_u^+ übergehen und asymptotisch den 2-Atom-Zustand $^1S_0 + {}^3P_1$ bilden. In diesen Molekülpotentialen wurde im Zuge dieser Arbeit der jeweils schwächstgebundene Zustand entdeckt und auf Verbreiterungsmechanismen sowie die Kopplung an externe Magnetfelder untersucht. Auf Basis der gemessenen Bindungsenergien und theoretischer Modelle bezüglich der Quantisierung der gebundenen Zustände werden Vorhersagen über die Bindungsenergien tiefer gebundener Zustände getroffen.
Das Wissen über die Photoassoziationsresonanzen mit vormals unerreichter Präzision ermöglicht die Bestimmung der Van-der-Waals-Koeffizienten sowie den Test von Quantisierungsformeln für nahasymptotische Molekülzustände. Desweiteren lässt sich das Streuverhalten der Atome durch Ankopplung an die Molekülzustände mittels optischer Feshbach-Resonanzen manipulieren. Zusammen mit der experimentellen Expertise zur Erzeugung von Bose-Einstein-Kondensaten lässt sich diese Manipulation des Streuverhaltens anschaulich nachweisen, da Stöße die relevante Energieskala innerhalb des Kondensats darstellen.

Schlagworte: ultrakalte Calcium-Atome, optische Dipolfallen, Bose-Einstein-Kondensation, Photoassoziations-Spektroskopie schmaler Linien, optische Feshbach-Resonanzen

Abstract

This thesis presents two significant contributions to the understanding of ultracold calcium atoms. After a short introduction on the basics of the experiment the first realization of a Bose-Einstein condensate of alkaline earth atoms is described. Due to the absence of a magnetic moment of ^{40}Ca ground state atoms the evaporation has to take place in an optical dipole trap. It was necessary to cope with difficulties like the large three-body losses, which has also been investigated in the course of this thesis.
The second integral part of this thesis is focussed on the investigation of narrow photoassociation resonances close to the intercombination transition between singlet and triplet states. Starting from an unbound atom pair of $^1S_0$ atoms one can excite into the two binding molecular potentials $a^3\Sigma_u^+$ and $c^3\Pi_u$, which change their character to 1_u and 0_u^+ for larger interatomic separation, respectively, and asymptotically form the two-atom state $^1S_0 + {}^3P_1$. In both molecular potentials the weakest bound state has been found in the course of this thesis. The resonances have been investigated in terms of broadening mechanisms and the coupling to an external magnetic field. On the basis of the measured binding energies and theoretical models regarding the quantization of bound states, predictions have been made for the binding energies of deeper bound states.
The knowledge about the photoassociation resonances with formerly unachieved precision allows for the determination of van der Waals coefficients and the test of quantization rules of near-asymptotic molecular states. Furthermore an optical coupling to these molecular states can be exploited in an optical Feshbach resonance to tune the scattering behaviour of the atoms. Together with the experimental proficiency of the realization of a Bose-Einstein condensate these manipulation of the scattering behaviour can be visualized due to the fact, that collisions represent the relevant energy scale inside Bose-Einstein condensates.

Keywords: ultracold calcium atoms, optical dipole traps, Bose-Einstein condensation, narrow-line photoassociation spectroscopy, optical Feshbach resonances

Contents

1 Introduction **9**

2 Laser Cooling of ^{40}Calcium **13**
2.1 Preparation of cold calcium atoms using the main fluorescence line . 13
2.1.1 Generation and stabilization of blue light 14
2.1.2 Repump laser for the first stage MOT 15
2.2 Approach to μK temperatures - second MOT stage on the intercombination line 16
2.2.1 Quench cooling 16
2.2.2 Setup of the red laser system for the second MOT stage 16

3 Characterisation of the Dipole Trap Setup **19**
3.1 The ac-Stark effect - light shifts and differential light shifts 19
3.1.1 Dressed states and light shifts 19
3.1.2 Differential light shift and magic wavelength 20
3.1.3 Yb:YAG laser setup 21
3.1.4 Measurements for the determination of the magic wavelength 22
3.2 Dimensions of the dipole trap 23
3.2.1 Measurement of radial trap frequencies 24
3.2.2 Measurement of axial trap frequencies 26

4 Bose-Einstein Condensation of Calcium **29**
4.1 Theoretical description of a BEC 29
4.1.1 Peculiarities of calcium 31
4.2 Three-body losses of dense calcium ensembles 32
4.3 Forced evaporation scheme in a crossed dipole trap 34
4.4 Creation of a BEC 38
4.4.1 Bose-Einstein condensation in a crossed dipole trap 38
4.4.2 Bose-Einstein condensation in a single-beam dipole trap . . . 42

5 Photoassociation at the Intercombination Line **47**
5.1 Basic theory of Ca_2 molecules and their light assisted generation . . . 47
5.1.1 Multipole expansion of molecular potentials 47
5.1.2 Hund´s coupling cases in homonuclear molecules 48
5.1.3 Selection rules 49

5.1.4 Molecular potentials a and c 51
5.1.5 Photoassociation spectroscopy near the intercombination transition 53
5.2 Setup for photoassociation on the intercombination line 54
5.3 Results of the photoassociation measurements 55
5.3.1 Magnetic splitting and identification of the molecular state . . 56
5.3.2 Exact position of the photoassociation resonances 57
5.3.3 Broadening effects of the PA resonances 60
5.3.4 Measurement of the line shape 64
5.4 Quantization formulae for near-asymptotic bound states 66
5.4.1 WKB method 69
5.4.2 Le Roy-Bernstein formalism for level spacing near the dissociation limit 69
5.4.3 Raab-Friedrich formalism 72
5.4.4 Prediction of deeper bound states 73
5.5 Summary 74

6 Conclusion and Outlook 77

Chapter 1

Introduction

Atomic physics has been a fast-growing field in modern physics during the last decades both due to significant improvements in the development of lasers as well as the wide range of opportunities the field holds. The applications of laser cooled ensembles range from precision spectroscopy [For07, Eyl07] over optical clocks [Did04, Fal11] and the fundamental understanding of quantum-mechanical behaviour in Bose-Einstein condensates [Ang02] to the generation and investigation of weakly bound molecules [Kno10, Osp10].
The technique of laser cooling of neutral atoms has been first proposed by Hänsch and Schawlow [Hän75], which resulted in the first realization of an optical molasses [Chu85], in which the atoms experience a velocity dependent force from the scattered photons. The combination with a spatial dependent scattering force in a magnetic quadrupole field resulted in the magneto-optical trap (MOT) [Raa87], which is a standard tool in most of today´s experiments in atomic physics. Also in the late 1980s the most important conservative traps for neutral atoms, the magnetic trap [Mig85] and the optical dipole trap (ODT) [Chu86], have been developed.
The laser cooled atom ensembles can have densities in the order of 10^{10} cm^{-3} (compared to $3 \cdot 10^{19}$ cm^{-3} at room temperature and atmospheric pressure). The achieved temperatures range from several 10 μK to a few mK inside a MOT, depending mainly on the width of the used cooling transition. At these temperatures the atoms still behave like classical point-like particles. Louis de Broglie predicted a wave-like nature of particles at a scale of the thermal de Broglie wavelength $\lambda_{DB} = h/\sqrt{2\pi m k_B T}$ [Bro24]. In classical gases this length scale however is much smaller than the interatomic separation and is thus of no physical importance. To see an influence of the quantum mechanical wavefunction of the atoms it was a motivation to further lower the temperature and thus increase the de Broglie wavelength and at the same time lower the interatomic distance by increasing the density. To overcome the limits in density and temperature stated by Doppler cooling techniques, the atoms are therefore loaded from the MOT into a conservative potential as provided by a magnetic trap or an optical dipole trap. The cooling in these traps is typically done by evaporation, meaning that the trap depth is lowered and the high energy atoms leave the trap effectively cooling the remaining ensemble. The phase space density, given by the number of atoms in a phase space volume of $\hbar^3$,

can be written as $\rho_{PSD} = \rho \cdot \lambda_{DB}^3$. If the phase space density becomes in the order of unity, the atoms will interact as waves rather than point-like particles. For the case of undistinguishable bosons, Albert Einstein predicted the formation of a new matter state called Bose-Einstein condensate (BEC) for a phase space density larger than 2.6 in free space [Ein25] based on the statistical works of Satyendranath Bose [Bos24]. In a qualitative picture the wave packages of the atoms overlap and build one macroscopic wavefunction of ground state atoms. Quantum mechanical effects like interferences and entanglement become visible on macroscopic scale. Moreover BECs are an adequate tool for the investigation of quantum-mechanical manybody effects like superfluidity [Lim08] and solitons [Bec08].
Most of the early laser cooling and laser cooling based experiments were performed with alkali atoms due to the availability of suitable lasers. In addition the magnetic moment of ground state alkali atoms permits the usage of magnetic traps for the evaporative cooling. It is therefore not a surprise that the first Bose-Einstein condensates were achieved with rubidium [And95], lithium [Bra95] and sodium [Dav95] in 1995.
Alkaline earth atoms however had many difficulties connected to them. The first difficulty was the absence of suitable easy-to-handle lasers. The strong fluorescence lines of alkaline earth atoms are in the blue part of the spectrum, for which dye lasers were less efficient. The development of blue diode laser just brought acceptable results a few years ago, so for long time one had to use infrared lasers like Titanium:Sapphire with a consecutive frequency doubling stage and all its complications. The Doppler limit of the main fluorescence line is in the order of one millikelvin and the absence of a nuclear or electronic spin of the bosonic isotopes prohibits sub-Doppler cooling mechanisms. To reach ultracold temperatures a second MOT stage has to be applied. The ultranarrow intercombination lines between the singlet and the triplet system, a feature based on the two valence electrons, offers a low Doppler limit. The intercombination line of calcium is too narrow to permit strong enough forces so that the linewidth has to be artificially broadened by quench cooling [Bin01, Meh03]. An alternative scheme is the use of a MOT for metastable atoms in the triplet system [Grü01, Kul12].
The novel opportunities alkaline earth atoms yield in comparison to alkali atoms however are worth the trouble. The absence of a magnetic spin of bosonic alkaline earth isotopes simplifies the electronic structure and therefore the theoretical description of collisions [Mac01, Der03] and excitations to molecular states [Zin00, Ciu04]. The narrow intercombination transitions can be used as frequency standards [Deg05b, Hoy05, Tak06, Fal11] or for precision experiments using atom interferometry [Mor96, Yan02]. For a closer look on atom-atom interactions the realization of a BEC of alkaline earth atoms was of great interest. Here another difficulty came up. The absence of a magnetic moment in the ground state also prohibits the confinement in a magnetic trap. Magnetic traps have emerged to a powerful tool for alkali atoms due to the large trap depths achieved and the large volume of the trap. The storage of excited metastable calcium atoms in a magnetic trap was achieved [Han03], but the inelastic losses made the evaporation down to a BEC impossible [Han06]. The generation of quantum degenerate alkali gases with the help of opti-

cal dipole traps [Bar01, Gra02] paved the way to all-optical BECs of alkaline earth atoms. The rare earth isotope ^{174}Yb, which has also two valence electrons and thus shares the electronic structure with most of the connected difficulties and opportunities, was condensed in 2003 [Tak03]. The intercombination line $^1S_0 - {}^3P_1$ though, which is a valuable tool for the probing of shift and broadening effects in ultracold gases, is relatively broad in ytterbium (180 kHz [Toj06]) compared to calcium (374 Hz [Deg05b]) and strontium (7.4 kHz [Xu03]). Experiments aiming for a BEC of ^{88}Sr failed due to a very small scattering length and thus a very low evaporation and thermalization rate. Loading of calcium into an ODT turned out to be difficult. The differential light shift between the $^1S_0$ and $^3P_1$ state was much larger than the linewidth of the transition effectively tuning the cooling laser out of resonance at the position of the ODT. This demanded for an ODT at the magic wavelength [Kat99]. In the course of this thesis finally a BEC of an alkaline earth element was achieved [Kra09], although huge three-body losses connected to the large ground state scattering length between $340\ a_0$ and $700\ a_0$ [Vog07] marked another difficulty. The calcium BEC presented in this work was closely followed by a condensate of ^{84}Sr [Ste09, Mar09]. Recently an alternative route for the condensation of calcium atoms has been developed at the Universität Hamburg [Hal12]. Using a MOT of metastable triplet atoms with consecutive depumping into the ground state, this scheme might be well suited for lighter alkaline earth elements like magnesium. The achieved atom number inside the BEC is 5-fold smaller than in our experiment though.

While a BEC is a good tool for the investigation of interatomic and multibody interactions, one might also want to have the opportunity to manipulate the interaction. The interatomic interaction is strongly dependent on the existence of a molecular state close to the diatomic asymptote [Fed96b]. Magnetic Feshbach resonances are a common tool to shift a nearby magnetically sensitive molecular state into the resonance of the scattering wave. Magnetic Feshbach resonances were first observed in 1998 [Ino98]. With the help of these resonances it was possible to change the scattering length of chromium to a value appropriate for evaporation down to a BEC [Gri05]. It was also possible to form weakly bound molecules by slowly ramping the magnetic field over the Feshbach resonance [Köh06]. In alkaline earth atoms however magnetic Feshbach resonances can not be applied, again due to the absence of a magnetic spin in the ground state. Optical Feshbach resonances have been proposed [Fed96a] as an alternative way to influence the scattering length by coupling the ground state atoms to a molecular excited state optically. It has first been observed in sodium [Fat00], but was accompanied by large photoassociative losses. Theory predicts the ratio of losses due to photoassociation and the achieved modulation of the scattering length to be proportional to the natural lifetime divided by the detuning from a photoassociative resonance [Ciu05]. A narrow natural linewidth like the intercombination line in alkaline earth metals is therefore a good precondition for the application of low loss optical Feshbach resonances. This line has a width of 374 Hz in calcium compared to typically several MHz for singlet-singlet transitions and 7.4 kHz for the intercombination line in ^{88}Sr, which is the next heavier atom with a similar electron structure.

Optical Feshbach resonances in calcium can be used for reducing the naturally large scattering length, and thereby optimize the production and lifetime of Bose-Einstein condensates (compare chapter 4). Additionally they can be used to introduce spatially small regions of an altered scattering length inside a BEC for example to excite solitons.
The exploitation of optical Feshbach resonances demands for the knowledge of molecular states consisting of one ground state and one excited state atom. The most established tool for the detection of molecular energy levels close to the diatomic asymptote is photoassociation spectroscopy [Tho87]. A pair of unbound ground state atoms can be excited into an excited molecular state by a photon. This leads to a loss of trapped atoms if the photon energy coincides with the energy gap between the ground state and the molecular state. The spacing between the molecular energy levels close to the diatomic asymptote is subject of many theoretical investigations (e.g. [Le 70, Le 80b, Com04, Raa08]). There are also some theoretical calculations about the loss coefficient of photoassociation spectroscopy [Ciu04]. The small linewidth of the transition entails a low coupling strength to the molecular state, which demands for a dense atomic ensemble of low temperature to achieve well detectable trap losses. The technique of generating ensembles with high phase space density as developed for the Bose-Einstein condensation supplies us with the necessary conditions for photoassociation spectroscopy.
This thesis will present the first achievement of a Bose-Einstein condensate of ^{40}Ca atoms as the first alkaline earth BEC worldwide. In addition the first steps towards optical Feshbach resonances were done by finding the weakest bound molecular levels in the 0_u^+ and 1_u potentials near the $^1S_0 - {}^3P_1$ asymptote via photoassociation spectroscopy. The broadening and shift mechanisms as well as the coupling to an external magnetic field have been investigated and a reliable prediction of deeper bound levels is performed on the basis of established theoretical models.

Chapter 2

Laser Cooling of ^{40}Calcium

The main tool for the generation of cold and ultracold ensembles in atomic physics experiments is the magneto-optical trap (MOT). It consists of 6 pairwise counter-propagating beams, which are red-detuned to an electronic transition in the order of its linewidth, and a magnetic quadrupole field. The magnetic field is zero at the centre of the MOT with a constant gradient in all directions. The laser beams are circularly polarised in a way, that an atom displaced in a given direction mainly absorbs the laser beam, which is pushing it back into the centre by radiation pressure, effectively representing a harmonic trapping potential. In addition, an atom with a velocity into one direction preferably absorbs the counterpropagating beam, which is closer to resonance than the copropagating one due to the Doppler effect. This way the MOT also creates a velocity-selective force, which cools the atoms down to a temperature limited by the heating due to statistical scattering of photons, the so-called Doppler limit. A more detailed and analytic description of Doppler cooling and magneto optical traps can be found in [Met99, Mey01].
In this chapter I will shortly outline the laser cooling schemes in our experiment and the setup of the corresponding laser systems.

2.1 Preparation of cold calcium atoms using the main fluorescence line

The low vapour pressure of calcium at room temperature makes loading of a MOT from a background gas very inefficient. We therefore heat calcium inside an oven to a temperature of $610°$ C and decelerate the hot atoms with a Zeeman slower. The slow atoms are then deflected by a 2D-molasses into our trapping region. This setup avoids collisions between trapped atoms and the beam of hot atoms by geometric separation (see fig. 2.3).
The ground state of ^{40}Ca is a $^1S_0$ state with a fully populated $4s$ orbital. The strongest fluorescence line is connecting the $^1S_0$ to the $^1P_1$ state (see figure 2.1). This line has a wavelength of 423 nm and a linewidth of 34 MHz. This transition is used for the Zeeman slower beam and the molasses as well as a first MOT stage.
The absence of a nuclear as well as electronic spin in the ground state prohibits sub-

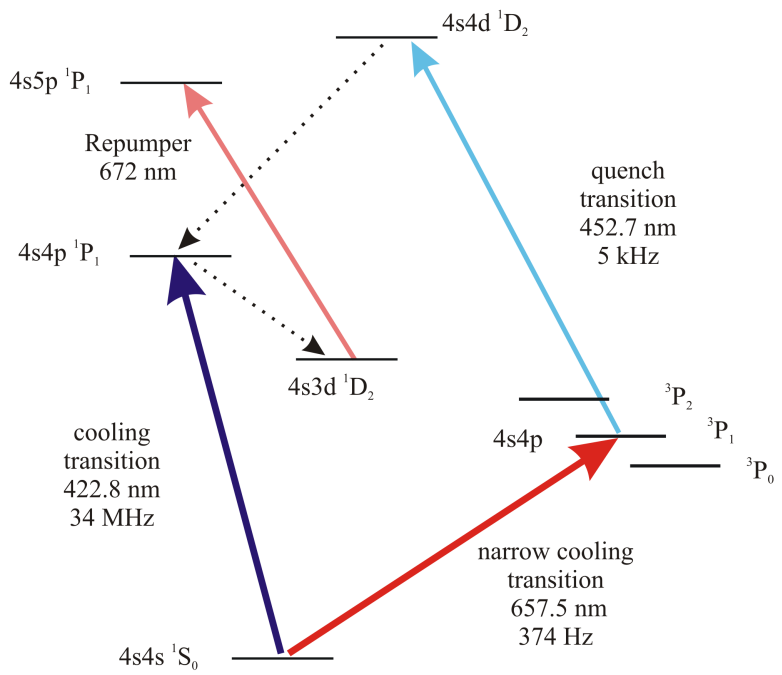

Figure 2.1: Level scheme of ^{40}Ca showing the atomic levels relevant for this work. Cooling transitions as well as the repump and the quench transition are displayed.

Doppler cooling mechanisms such as polarisation gradient cooling. We reach atom numbers of about $2 \cdot 10^8$, without the repumper explained later in this section, at a temperature of 1-2 mK, not much higher than the Doppler limit of 0.8 mK. The magnetic field is generated by a pair of coils in anti-Helmholtz configuration. Its gradient is 2.55 mT/cm at a current of 17 A [Naz07].

2.1.1 Generation and stabilization of blue light

To generate laser light at 423 nm we use a frequency-doubled Titanium:Sapphire (Ti:Sapphire) laser[1] pumped by a frequency doubled Nd:YAG[2]. The Ti:Sapphire has a bow tie configuration and an optical isolator selecting one direction of circulation and can therefore be operated in single mode. The Ti:Sapphire has an output power of 1.45 W at a wavelength of 845 nm when pumped with 9.5 W.
The frequency doubling of the light is done in a Lithium triborate crystal placed in a ring cavity which is further described in [Deg04a]. It is stabilised to the incoming infrared light via Hänsch-Couillaud [Hän80] locking technique. We achieve 520 mW of blue light. Most of the power is used for the Zeeman slower beam. To be on resonance with the high velocity atoms out of the oven, the Zeeman slower beam is red-detuned by 512 MHz via an acusto-optic modulator. About 22 mW of the blue light is used for the 6 MOT beams at a detuning of 42 MHz, which enter the chamber

[1] Coherent MBR - 110
[2] Coherent Verdi V10

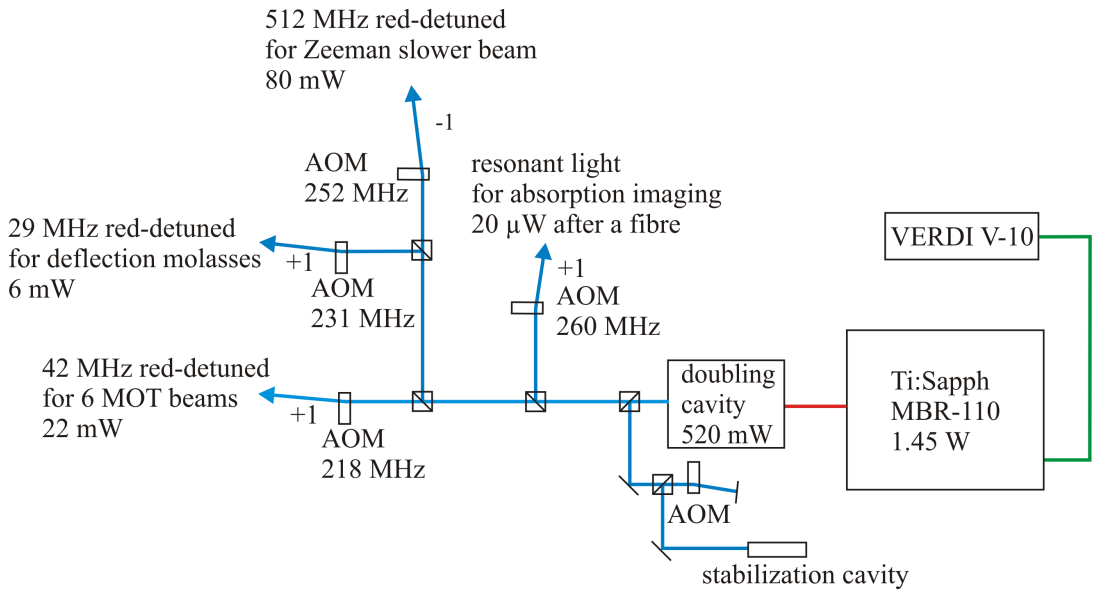

Figure 2.2: Schematic overview of the frequency synthesis and the distribution of blue light into the experiment. There are additional beam paths for example an additional reflection at the surface of the Lithium triborate crystal, which were not used in the experiments of this thesis though. The abbreviations are AOM = acousto-optic modulator, Ti:Sapph = Titanium:Sapphire laser

circularly polarized. Each beam is enlarged with a telescope to a $1/e^2$-radius of intensity of 1.2 cm. Further application of the blue light is the deflection molasses as well as absorption imaging of ground state atoms with a CCD-camera[3]. A small fraction of the laser power is used to stabilise the laser frequency to a passive cavity via lock-in technique, in which the frequency modulation is done by an acousto-optic modulator (AOM). An overview of the distribution of the blue light is given in fig. 2.2.

2.1.2 Repump laser for the first stage MOT

The MOT-transition $^1S_0$ - $^1P_1$ is not perfectly closed. Atoms in the $^1P_1$ state can alternatively decay to the $4s3d\,^1D_2$ level with a relative strength of 10^{-5} [Bev89]. From this level the atoms can decay back to the ground state via the $^3P_1$ state or into the metastable $^3P_2$ state with a lifetime of 2 hours [Der01]. To avoid this loss channel we shine in a repump laser beam. This repump laser transfers the atoms from the $^1D_2$ state to the $4s5p\,^1P_1$ state, from where the atoms efficiently decay back to the ground state. The repump laser is a diode laser[4] operated at 672 nm and stabilized to a passive cavity.
Via a fibre we get $150\ \mu$W into the vacuum chamber from one direction and retroreflect the beam to achieve a higher intensity. This way we can increase the atom

[3]Roper Scientific CoolSNAP ES
[4]Toptica DL 100

number in our first MOT stage by a factor of three. We can store up to 10^9 (typically $5 \cdot 10^8$) atoms in the MOT with the repumper being applied.

2.2 Approach to μK temperatures - second MOT stage on the intercombination line

The achieved temperatures in the order of millikelvin are too high for efficient loading into an optical dipole trap. For further cooling we use the intercombination transition to the triplet state $^3P_1$. The transition between singlet and pure triplet states is strictly forbidden for dipole radiation, however a small mixing with singlet states, mainly the $^1P_1$ state, allows the transition, giving it a linewidth of $\gamma = 2\pi \cdot 374$ Hz [Deg05b]. The Doppler limit $T_{Doppler} = \frac{\hbar\gamma}{2 \cdot k_B}$ of this transition is 9 nK, when no broadening techniques are applied and the temperature of the atoms would therefore be limited by the recoil limit of 0.55 μK [Cas89].

2.2.1 Quench cooling

The force applied by the scattering of photons on the intercombination transition at the capture radius of the MOT, where the detuning is cancelled by the Zeeman shift, can be calculated to $F = \hbar k\gamma/2 = 1.2 \cdot 10^{-24}$ N for intensities much larger than the saturation intensity, which results in an acceleration of $F/m_{Ca} = 18$ m/s^2. This force is hardly enough to compensate gravity.
To increase this force and prevent the atoms from falling, we increase the rate of scattered photons artificially. This is done by applying a quench laser[5] at a wavelength of 453 nm. The quenching light is shined in from the bottom of the chamber circularly polarized and retroreflected after passing a $\lambda/4$-plate twice. The quench laser couples the excited $^3P_1$ state to the faster decaying $4s4d$ $^1D_2$ state. Due to this mixing of states, the rate of photon scattering and thus the cooling force increases, but at the cost of higher temperatures [Bin01].
In this second MOT stage we achieve atom numbers of up to 10^8 (typically $4 \cdot 10^7$) atoms at 12 μK with a half-life time of around 300 ms.

2.2.2 Setup of the red laser system for the second MOT stage

The 657 nm light for the second MOT stage is generated by diode lasers in master-slave-configuration. Since the transition was formerly used as a frequency standard [Wil01] the master laser is Pound-Drever-Hall [Dre83, Bla01] stabilized with about 1 Hz linewidth to a passive cavity with a noise, vibration and thermally isolated mounting [Naz06]. The drift of the cavity and therefore of the laser frequency is 35 mHz/s. It is compensated by a double-pass AOM, which is permanently frequency sweeped via a direct digital synthesizer (DDS). The light from the master is amplified by a series of injection locked slave lasers (see fig. 2.4). The light is

[5] Toptica TA/DL-SHG 110

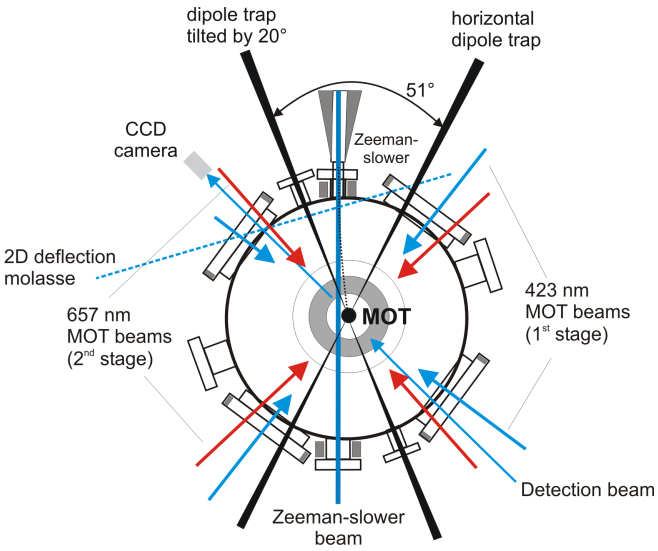

Figure 2.3: Schematic drawing of the vacuum chamber and the arrangement of laser beams for optical cooling, detection and the dipole trap. The drawing represents a top view onto the horizontal plane, whereas one of the dipole trap beams is tilted by $20°$ with respect to that plane.

used in the experiment for Doppler free spectroscopy as well as cooling. The light for cooling is frequency modulated to have a broader spectrum. The spectrum can be approximated by a rectangle in frequency space with a full width of 3.4 MHz, and the nearest resonant edge red-detuned from the atomic resonance by 320 kHz. The light enters the chamber from 3 directions and is retroreflected after passing through. The total power of all 3 beams is 18 mW, the $1/e^2$-radius of intensity is 4.9 mm. An overwiew of the distribution of the red light is given in figure 2.4.

From the second MOT stage we load the atoms into a dipole trap at a wavelength of 1031 nm, in which most of our experiments are performed. The dipole trap is further described in chapters 3 and 4. A schematic overview of the vacuum chamber and the arrangement of laser beams is shown in fig. 2.3. The optical cooling transitions are displayed in fig. 2.1.

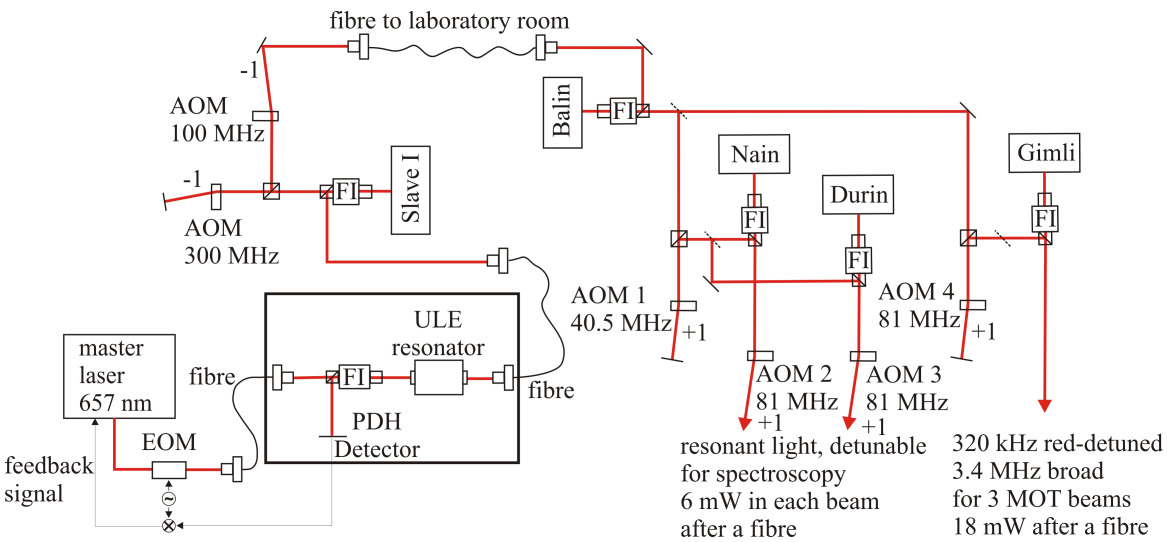

Figure 2.4: Schematic overview of the frequency synthesis and the distribution of red light to the experiment. The left side shows the stabilization to an ultrastable cavity [Naz06] as well as a slave laser and a sweepable 300 MHz AOM for the compensation of the cavity drift. The right side shows the slave system in the laboratory room. The four slave lasers are named after characters from the novel "The Hobbit, or There and Back Again" [Tol37] for better distinction. AOM 2 and AOM 3 can be sweeped for spectroscopy scans. AOM 4 is used to modulate a cooling comb onto the light, broadening the laser spectrum to 3.4 MHz. The abbreviations are FI = Faraday Isolator, EOM = electro-optic modulator, AOM = acousto-optic modulator, PDH = Pound-Drever-Hall, ULE = ultra-low expansion glass.

Chapter 3

Characterisation of the Dipole Trap Setup

Photon scattering represents a severe limitation to laser cooling down to quantum degeneracy. Only one group has reported on laser cooling down to a BEC by deliberately making atoms transparent to the cooling radiation [Ste13]. In the usual approach the laser cooled ensemble is loaded into a conservative trapping potential and evaporatively cooled, meaning that the high energetic atoms are selectively released from the trap effectively cooling the remaining ensemble. While the first choice for a conservative trapping potential for neutral atoms is the magnetic trap due to its simple applicability and large trapping volume, this kind of trap is only practicable for atoms with a magnetic moment, which is not given for the ground state of ^{40}Ca among all other bosonic alkaline earth metals. Instead the atoms are loaded into an optical dipole trap at a wavelength of 1031 nm. This chapter will give an overview of the setup and present some experiments on the characterisation of the trap parameters, which has been helpful for the achievement of a BEC as well as the description of atomic ensembles above and below the critical temperature.

3.1 The ac-Stark effect - light shifts and differential light shifts

3.1.1 Dressed states and light shifts

The principles of the dipole force can be well explained in the dressed state model (see e.g. [Gri00]). In a two-level system the atomic states Ψ_g and Ψ_e are no longer eigenstates of the Hamiltonian in the presence of a light field. When writing the Hamilton operator in matrix form with the basis vectors Ψ_g and Ψ_e, the light interaction will appear as off-diagonal entries and the new eigenstates are found by diagonalization of the matrix. It can be shown, that for red-detuned light the lower state is shifted to lower energies by the presence of the light proportional to its intensity, while the upper state is shifted to higher energies by the same amount. For non-excited atoms a Gaussian shaped red-detuned laser beam thus represents

a conservative Gaussian shaped trapping potential. The trapping potential can be approximated to [Gri00]

$$U_{dip}(r) = \frac{3\pi c}{2\omega_0^3}\frac{\Gamma}{\Delta}I(r) \tag{3.1}$$

where ω_0 is the transition angular frequency, Γ its linewidth and Δ the detuning from resonance. $I(r)$ is the intensity profile of the trapping laser.
For a more realistic multi-level atom the total light shift of the ground state is given by the sum of the light shifts arising from all possible transitions, each calculated with its corresponding transition strength and detuning. The shift is often referred to as the ac-Stark effect.
Note that different magnetic sublevels generally experience different shifts, since the transition strengths to other levels scale with the Clebsch-Gordan coefficients. Also the polarization of the dipole trap light determines which transitions will contribute to the light shift. Thus traps of the same wavelength but different polarizations result in different light shifts for the sublevels.

3.1.2 Differential light shift and magic wavelength

As mentioned above not only the ground state experiences a shift, but also the excited states. Thus a probe beam will be absorbed at a different frequency compared to in absence of a dipole trap. I will call this shift of the transition, which is the difference between the shifts of the ground and excited state, a differential light shift. In a two-level system this differential shift is twice the shift of the ground state. While transitions which are very strong compared to all other transitions can be well described as a two-level system, this is not the case for the intercombination transitions between singlet and triplet states in calcium. The light shift of the ground state is mainly given by the coupling to other singlet states, whereas the light shift of the triplet state is dominated by transitions in the triplet system. The light shifts of the $^1S_0$ and the $^3P_1$ sublevels in dependence of the dipole trap wavelength are shown in figure 3.1. For a certain wavelength of the trapping laser one can achieve an identical shift for the ground and excited state (red circles in fig. 3.1). In this case the transition frequency is not influenced by the intensity of the light, while the potential depth is. The wavelength for which this is the case is called "magic wavelength". In our calcium experiment the transition $^1S_0 - ^3P_1$ is of critical importance. The loading of the dipole trap takes place during the second MOT stage. Since the dipole trap is a conservative trap, atoms are accelerated when entering the trap and can only stay in the trap, if the gained energy is dissipated inside the dipole trap. This dissipation can be provided by the MOT beams. Since the light shift is large compared to the detuning of the cooling beam, efficient cooling inside the trap can only be achieved in a dipole trap close to a magic wavelength. The importance of a magic wavelength trap for the transfer into the dipole trap has been pointed out by [Gra07] and characterised by [Vog09]. Two magic wavelengths have been determined by [Deg04b]. At a wavelength of $800.8(22)$ nm of a $\pi(\sigma)$-polarized dipole trap beam the $m = \pm 1$ ($m = 0$) sublevel experiences the same light shift as the ground state. In a

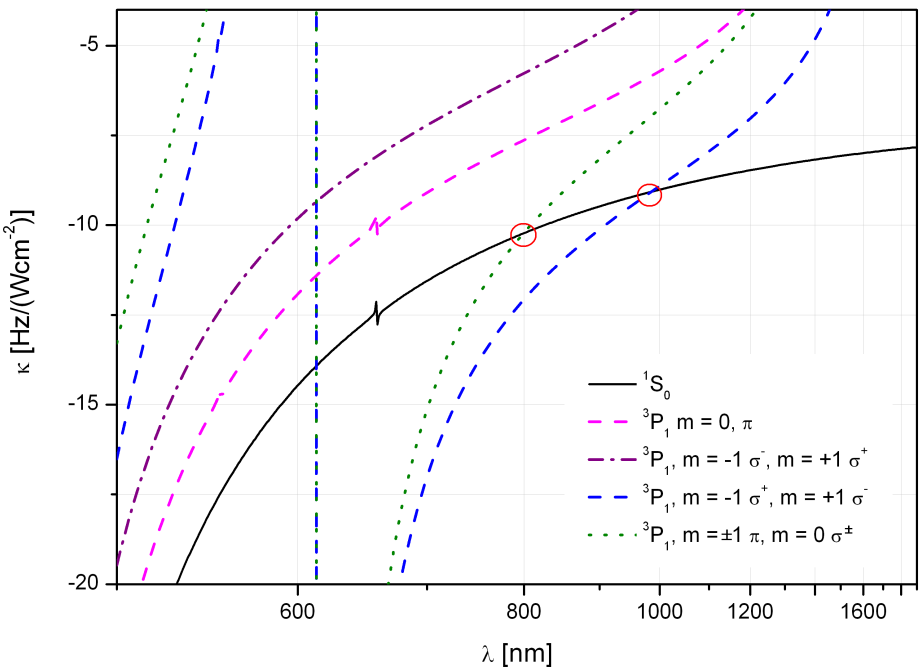

Figure 3.1: The light shift per intensity for the calcium ground state and for the $^3P_1$ m-sublevels in dependence of the dipole trap laser wavelength. The light shift of the m-sublevels also depends on the polarization of the trap laser. From [Deg04b], modified.

$\sigma^{\pm}$-polarized dipole trap the differential light shift to the $m = \mp 1$ sublevels vanishes at a wavelength of $983(12)$ nm.

3.1.3 Yb:YAG laser setup

The magic wavelength at 983 nm is preferred over the one at 801 nm due to the fact, that the non-magic magnetic subcomponents are tuned out of resonance rather than into resonance. We decided to use a diode pumped Yb:YAG disk laser[1] with a maximum output power of 25 W for our trapping beam for several reasons. The exact wavelength of the laser was measured[2] to be (1030.86 ± 0.15) nm, which is close to the magic wavelength. The high power and good beam profile enable us to generate a well-shaped deep trapping potential.
The light is split into two beams and each is sent through a photonic crystal fibre for the generation of a horizontal and a tilted dipole trap. The tilted dipole trap is intersecting the horizontal one at an angle of $51°$ in the horizontal plane and $20°$ tilted downwards to the horizontal plane. The total angle between the traps is thus

[1]prototype from the Institut für Strahlenwerkzeuge, Stuttgart; loan from Prof. Dr. Ertmer and Prof. Dr. Rasel, Leibniz Universität Hannover

[2]measured with Yokogawa AQ6317C Optical Spectrum Analyzer. The calibration was done at the day of measurement

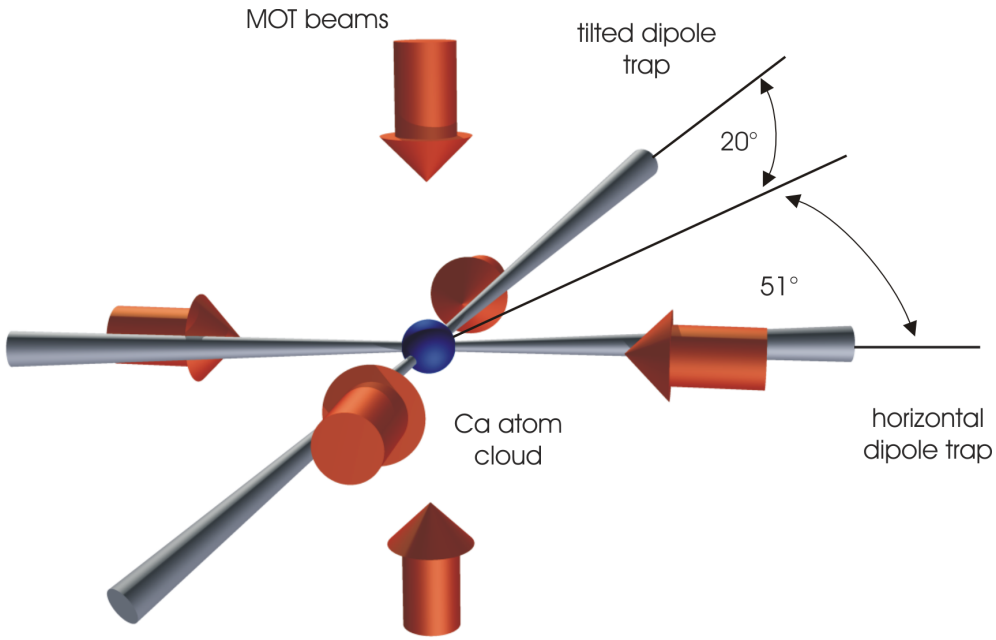

Figure 3.2: Sketch of the dipole trap and MOT beams arrangement at the position of the atomic cloud. The dipole trap beams intersect at an angle of $54°$, where one beam is tilted towards the horizontal plane by $20°$.

$54°$ (see fig. 3.2). The power of each beam is stabilized via a feedback loop to a power that can be set by the experiment control computer. The feedback signal is fed to an AOM in front of the fibre, which is also used for switching the dipole trap beams. Further details of the laser setup can be found in [Vog09].

3.1.4 Measurements for the determination of the magic wavelength

The knowledge of the magic wavelength is not just important for the loading of the dipole trap but also for some experiments of high precision spectroscopy inside the dipole trap. Thus it is useful to determine the magic wavelength as exactly as possible. The previous determination of the magic wavelength by [Deg04b] was done by measuring the shift at different wavelengths and extrapolating according to formula (3.1). The differential light shift at 1030.9 nm was measured in the course of this thesis to get a more precise knowledge of the magic wavelength.
For this we measured the transition frequency of the ${}^1S_0 - {}^3P_1$ intercombination line at different light intensities in a single-beam horizontal dipole trap. In the absence of a magnetic field the direction of the dipole trap beam represents a good quantization axis. The circularly polarised light for excitation was applied in the horizontal plane at an angle of $51°$ and could thus excite all three m_J components. The frequency of this excitation pulse was varied from shot to shot and the ground state atom number was measured by absorption imaging right after the excitation. For the evaluation of the light shift one has to account for the thermal distribution inside the trap. The atoms thus do not experience the peak intensity $I = \frac{2P}{\pi w_0^2}$, but a

Dipole trap polarization	Δm_J	light shift Hz/(W/cm^2)	interpolated from [Deg04b]
σ^+	$+1$	5.46 ± 0.32	5.68
σ^+	0	2.29 ± 0.17	2.52
σ^+	-1	0.45 ± 0.09	0.30
$\sigma + \pi$	0	3.08 ± 0.20	2.99
π	0	3.87 ± 0.30	3.46

Table 3.1: Differential light shift of the m_J-subcomponents. The first four values are the fit coefficients of the graphs in figure 3.3, where the fourth value represents a measurement with an external magnetic field applied. The last value is calculated from the measured values following geometric consideration about the polarization (see text). The uncertainty consists of the fit uncertainty as well as uncertainties in the ensemble temperature, power calibration and beam waist of the dipole trap.

reduced value according to their mean distance from the trap center. The average energy of the particles is $\overline{E_{pot}} = \overline{E_{kin}} = \frac{3}{2}k_B T$. The temperature of the atoms in a trap with a peak intensity of $1.4 \cdot 10^4$ W/cm^2 (trap depth of $k_B \cdot 5.9$ μK) was measured to be 1.0 μK, which leads to an effectively experienced intensity of $0.75 \cdot I_{peak}$. For higher intensity values we ramped down to the same low intensity first and then increased the power to enforce an accumulation closer to the peak intensity. Since the ramping was done adiabatically the temperature can be calculated to be $T = \sqrt{U/U_0} \cdot T_0$, where $U_0 = k_B \cdot 5.9$ μK and $T_0 = 1.0$ μK. In addition to the measurement without magnetic field there was done a series of scans with an applied Helmholtz field of around 0.27 mT perpendicular to the dipole trap and the differential shift of the $\Delta m_J = 0$ transition was measured. The magnetic field gives the quantization axis in good approximation. In a geometric model one can then think of the circularly polarized dipole trap beam as half π-polarized and half linearly polarized perpendicular to the quantization axis, which again can be decomposed into $\sigma^+ + \sigma^-$-light. We can thus separate the observed differential light shift $\Delta_{observed}$ into $\frac{1}{2}\Delta_\pi(m=0) + \frac{1}{2}\Delta_\sigma(m=0)$ and calculate $\Delta_\pi(m=0)$ from this with $\Delta_\sigma(m=0)$ measured independently in absence of the Helmholtz field.
The differential light shift in dependence of the dipole trap intensity is displayed in figure 3.3. The shift coefficients are summarized in table 3.1. The measured differential light shifts show a fair agreement with former values, originating from measurements of [Deg04b] and interpolated to the wavelength of 1031 nm.

3.2 Dimensions of the dipole trap

The dimensions of the dipole trap are of crucial interest. Since the density of the atoms can not be observed directly due to resolution limits, it has to be calculated from the temperature and the trap dimensions. A harmonically approximated trap centre will be occupied by an atomic ensemble of temperature T following a Maxwell-

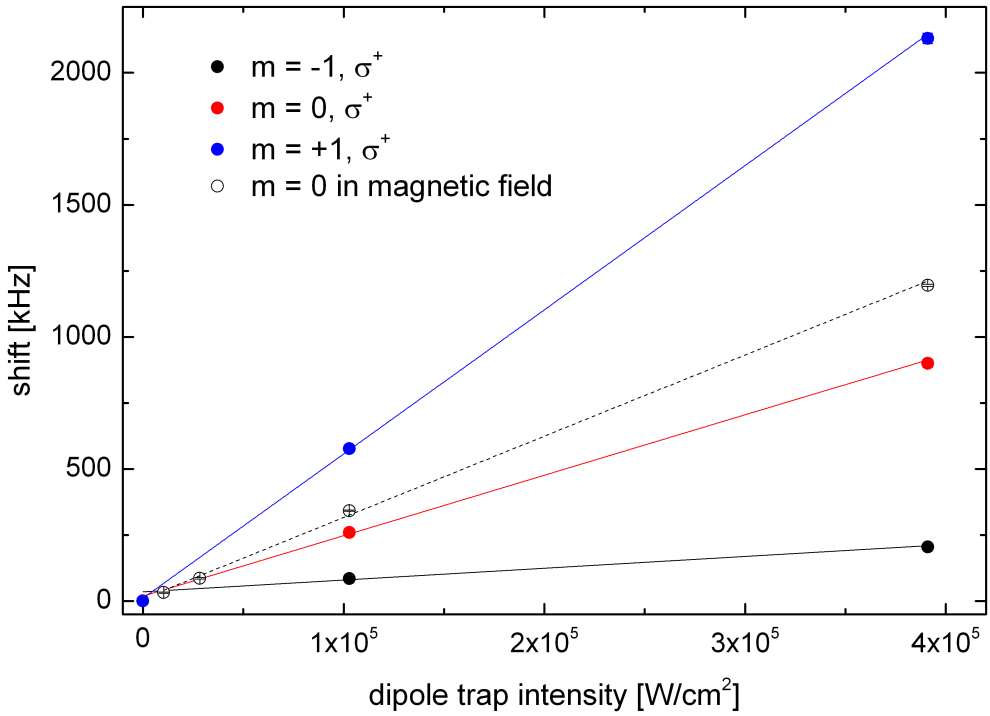

Figure 3.3: Differential light shift of the m_J-subcomponents in dependence of the dipole trap intensity. The solid circles represent a measurement without an external magnetic field. The empty circles represent the differential light shift of the $m_J = 0$ component in a magnetic field of around 0.27 mT. The shift is given relative to the frequency measured in absence of the trap beam. Thus (0 | 0) is not a distinguished point. In fact it shows a higher uncertainty due to a possible unresolved splitting by stray magnetic fields. However the disagreement of some fits with (0 | 0) contributes significantly to the uncertainty budget.

Boltzmann distribution with a density profile

$$\rho = \rho_0 \cdot e^{\left(-\frac{x^2}{2\sigma_x^2} - \frac{y^2}{2\sigma_y^2} - \frac{z^2}{2\sigma_z^2}\right)} \tag{3.2}$$

with $\sigma_i = \frac{1}{\omega_i}\sqrt{\frac{kT}{m}}$, ω_i the trap frequencies and

$$\rho_0 = N \cdot \omega_x \omega_y \omega_z \left(\frac{m}{2\pi kT}\right)^{3/2}. \tag{3.3}$$

The knowledge of the trap frequencies thus allows for the determination of the density profile from the easily accessible atom number N and temperature T.

3.2.1 Measurement of radial trap frequencies

The beam profile of our dipole trap laser beam is assumed to be rotationally symmetric. Eq. (3.2) can thus be simplified by the substitution $r^2 \equiv x^2 + y^2$, and

$\sigma_x = \sigma_y \equiv \sigma_r$. The potential of a single laser beam is strongly elongated along its direction of propagation. The trap thus has two strongly different trap frequencies ω_r and ω_z. The trap frequencies can be measured by inducing oscillations. For the measurement of the radial trap frequencies I decided to use a release-recapture method, which has also been used by [Deg04a].
The atoms are stored in a single-beam dipole trap. The dipole trap is then switched off to release the atoms. After a short time $t_{release,1}$ the dipole trap is switched on again. Most of the atoms are recaptured if $t_{release,1}$ is short enough, but they have expanded and are thus farther away from the trap centre and at a higher potential energy. This potential energy leads to an acceleration towards the centre of the trap. The atoms start to oscillate inside the conservative trapping potential. After a variable time of t_{osc} the dipole trap is switched off again. This time the expansion rate of the atoms depends on the phase of the oscillation. Another recapture after the time $t_{release,2}$ followed by an excitation of the atoms and fluorescence detection of the atom number via a photomultiplier is used to observe the oscillation phase in dependence of t_{osc}. For reference the fluorescence signal of the atom cloud is taken in another experimental cycle without the second switch-off. Also the dark count rate of the photomultiplier is measured.
Figure 3.4 shows the normalized atom number after the second recapture in dependence of the duration of the oscillation t_{osc}. Due to the symmetry of the oscillation, the signal is periodic with twice the trap frequency. The release times for this measurement were $t_{release,1} = 200$ μs and $t_{release,2} = 280$ μs.
The fast decay of the oscillation with a time constant of 0.25 ms can have different causes. One possible explanation is given by collisions between the atoms. The collisions will give the atoms a random direction of momentum, which makes the colliding atoms move out of phase of the other atoms. However, a repetition of the experiment with less atoms and otherwise unchanged conditions results in a similar damping time, even though collisions should be more than an order of magnitude less frequent. Thus collisions can not explain the fast decay of the oscillation. Another explanation involves the oscillation of atoms with different frequencies. The oscillations will wash out due to the dephasing of slower or faster oscillating atoms. A method of investigating this effect is the variation of the first release time $t_{release,1}$. For longer release times, more atoms will populate the outer anharmonic regions of the dipole trap when recaptured. Those atoms will perform a slower anharmonic oscillation. When increasing the first release time from $t_{release,1} = 100$ μs to $t_{release,1} = 280$ μs, the damping time of the oscillation decreases from 0.3 ms to around 0.19 ms, which proves the influence of anharmonic oscillations. The measurement shows, that the contribution of anharmonic oscillations does not influence the trap frequency determined by the fit significantly though.
In addition a possible ellipticity of the trap will lead to different oscillation frequencies along the two radial dimensions. This will again lead to a dephasing.
The trap frequency was determined several times with different release times $t_{release,1}$ and $t_{release,2}$ and different atom numbers. The trap frequency was calculated to be $\omega_r = 2\pi \cdot 1576(31)$ Hz in average. The power of the dipole trap beam was 5.75 W before entering the chamber and around $P = 4.95$ W at the position of the atoms.

The uncertainty of the power can be estimated by the calibration uncertainty (2.5 %) and possible fluctuations of the power during the measurement (1 %) to be 2.7 %. Using the measured trap frequency ω_r and assuming a Gaussian beam profile the beam waist can be calculated with the formula

$$\omega_r = \sqrt{\frac{4U_0}{m_{Ca} w_0^2}} \tag{3.4}$$

with w_0 the beam waist and $U_0 = \alpha \frac{I_0}{2\epsilon_0 c}$ [Deg04a] the trap depth. Here $I_0 = \frac{2P}{m w_0^2}$ is the peak intensity of the laser beam and $\alpha = h \cdot 47.25 \cdot 10^{-7}$ Hz/(V^2/m^2) the polarizability of the calcium ground state atoms at a dipole trap wavelength of 1031 nm as extrapolated from data of [Deg04b]. Following equation (3.4) we determine a beam waist of of $w_0 = 32.7(4)$ μm. The uncertainty results mainly from the trap frequency measurement itself, but also the uncertainty of the dipole trap power is accounted for.
The same measurement has been performed for the tilted dipole trap resulting in a trap frequency of $\omega_r = 1854(24)$ at a dipole trap power of 7.38 W. Assuming a Gaussian intensity profile again, this leads to a beam waist radius of $w_0 = 33.3(3)$ μm.

3.2.2 Measurement of axial trap frequencies

The atoms do not expand significantly along the axial direction of the dipole trap during the release times of around $t_{release,1} = 250$ μs. Much longer expansion times are not possible without losing the atoms. Thus the abovementioned release-recapture method is not suitable for the measurement of the axial trap frequencies.
One opportunity for the measurement of the axial trap frequencies is given by the experimental realization of a dipole trap wavelength, which is near the magic wavelength for only one m_J-subcomponent. Since the MOT beams have opposite polarizations the beam counterpropagating to the dipole trap beam is still absorbed by the atoms, while the MOT beam along the dipole trap beam is not absorbed. This results in an effective force, which dislocates the atoms from the dipole trap centre, as long as the MOT beams are switched on. After the loading of the dipole trap the MOT beams are switched off and the atoms start to oscillate along the weak axis of the dipole trap. Since the spatial amplitude of the oscillation is large enough, it can be observed directly as a change of the position on the absorption image. The oscillation is shown in figure 3.5. In this measurement the damping of the oscillation can most probably be attributed to collisions, since the atomic ensemble is in the hydrodynamic regime along the axial direction of the trap. The oscillation leads to a trap frequency of $\omega_z = 2\pi \cdot 6.6(1)$ Hz at a dipole trap power of 6 W in front of the chamber (around 5.16 W at the position of the atoms).
This value can be compared to the measurement of the radial trap frequency. Considering a waist radius of $w_0 = 32.7$ μm and a purely Gaussian beam, we can calculate the Rayleigh length to be $z_R = 3.25$ mm. The axial trap frequency would then

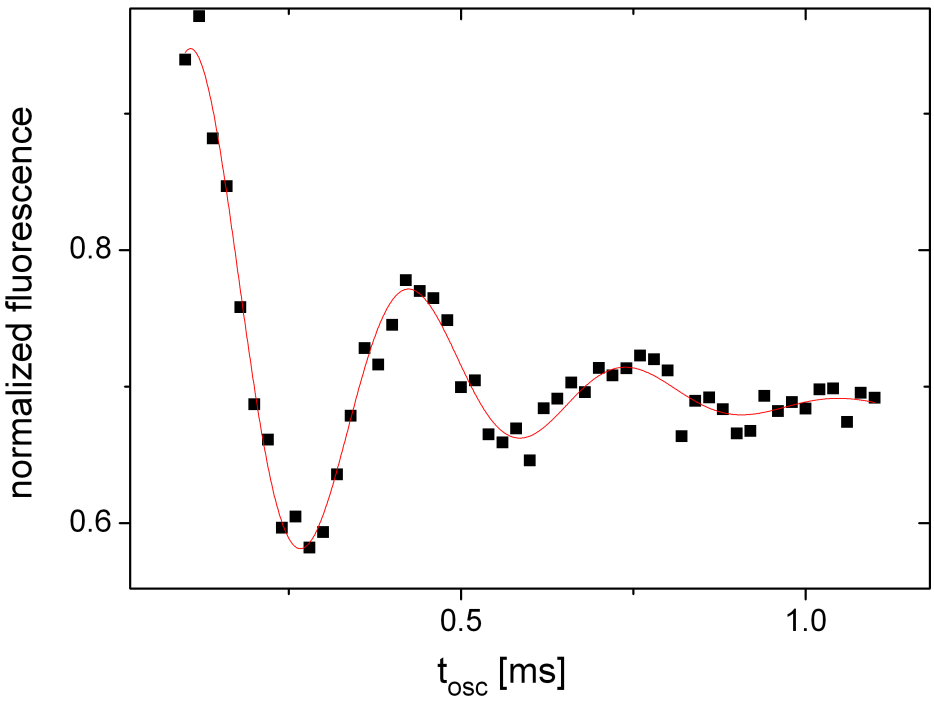

Figure 3.4: Oscillation of the atoms along the radial dimension of the dipole trap measured with the release-recapture method as described in the text. Plotted is the normalized fluorescence of the recaptured atoms against the duration of the oscillation t_{osc}. The fit represents a damped oscillation with a linear drift. The oscillation frequency represents twice the trap frequency. The trap frequency obtained from this measurement is $\omega_r = 2\pi \cdot 1577(22)$ Hz.

be

$$\omega_z = \sqrt{\frac{2U_0}{m_{Ca} z_R^2}} = 2\pi \cdot 11.4 \text{ Hz}. \tag{3.5}$$

The discrepancy might arise from an astigmatism. The beam profile has been observed with a camera at different positions along the dipole trap axis. The positions of the waists in the x- and y-direction of the beam differ by about $1.6(8)$ mm. This astigmatism reduces the curvature of the trap around the minimum by a factor between 1.07 and 1.8, resulting in a lowering of the trap frequency of a factor between 1.03 and 1.36. Even though this does not explain the discrepancy quantitatively, the trap frequency measurements represent a good understanding of the trap geometry, which helps determining the density and phase space density – important quantities on the way to quantum degeneracy and the description of the BEC presented in the next chapter.

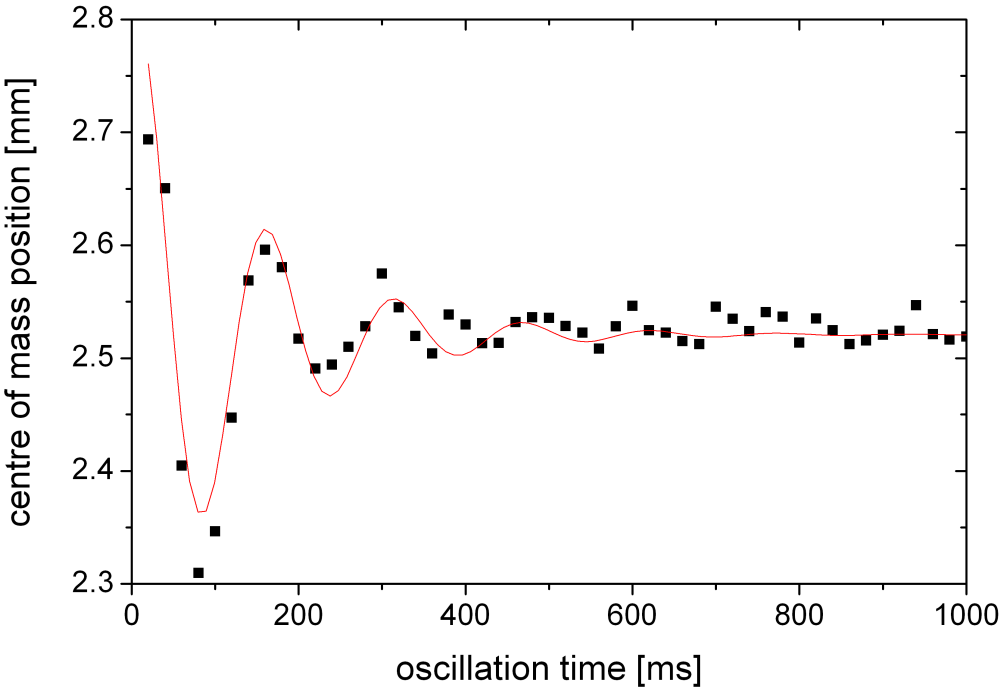

Figure 3.5: Oscillation of the atoms along the axial direction of the dipole trap. The centre of mass position of the atom ensemble is plotted against the time after switching off the second MOT stage. The fit represents a damped oscillation. The trap frequency gained from this measurement is $\omega_r = 2\pi \cdot 6.5(1)$ Hz.

Chapter 4

Bose-Einstein Condensation of Calcium

In this chapter the first realization of a Bose-Einstein condensate (BEC) of alkaline-earth atoms will be presented. As mentioned earlier the applied cooling scheme is evaporative cooling in an optical dipole trap. This scheme will be described in this chapter and the peculiarities associated with calcium atoms are pointed out. Finally the Bose-Einstein condensate and experiments showing its characteristical behaviour are presented.

4.1 Theoretical description of a BEC

A qualitative picture of the behaviour of bosonic atoms at different temperatures is sketched in the often cited drawing of W. Ketterle et al. [Ket99] (figure 4.1). A necessary condition for the formation of a BEC is the overlap of the wave packets of the atoms. A measure for this overlap is the phase space density ρ_{PSD} defined as the number of atoms in a phase space volume of $\hbar^3$. It can be written as $\rho_{PSD} = n \cdot \lambda_{DB}^3$, where n is the atomic density and $\lambda_{DB} = \frac{h}{\sqrt{2\pi m k_B T}}$ is the de Broglie wavelength. The critical phase space density for the formation of a BEC is 2.6 in free space and 1.2 in a harmonic trapping potential as approximately given by a Gaussian optical dipole trap. Rearranging the formula $\rho_{PSD} = 1.2$ results in a formula for the critical temperature T_c. An advanced theory also takes into account the finite atom number and interaction and leads to [Gio96]

$$T_C = 0.94\frac{\hbar\bar{\omega}}{k_B}N^{1/3}(1 - 0.73\frac{\omega'}{\bar{\omega}}N^{-1/3} - 1.33\frac{a_{sc}}{\sqrt{\hbar/(m_{Ca}\cdot\bar{\omega})}}N^{1/6}) \tag{4.1}$$

where $\bar{\omega} = (\omega_1 \cdot \omega_2 \cdot \omega_3)^{\frac{1}{3}}$ is the geometric average and $\omega' = (\omega_1 + \omega_2 + \omega_3)/3$ the arithmetic average of the angular trap frequencies and a_{sc} is the ground state s-wave scattering length.
While the kinetic and potential energies inside a BEC are comparatively low the densities can get very high. The interaction between the atoms can thus no longer be neglected and has to be included in the Schrödinger equation. This is usually done

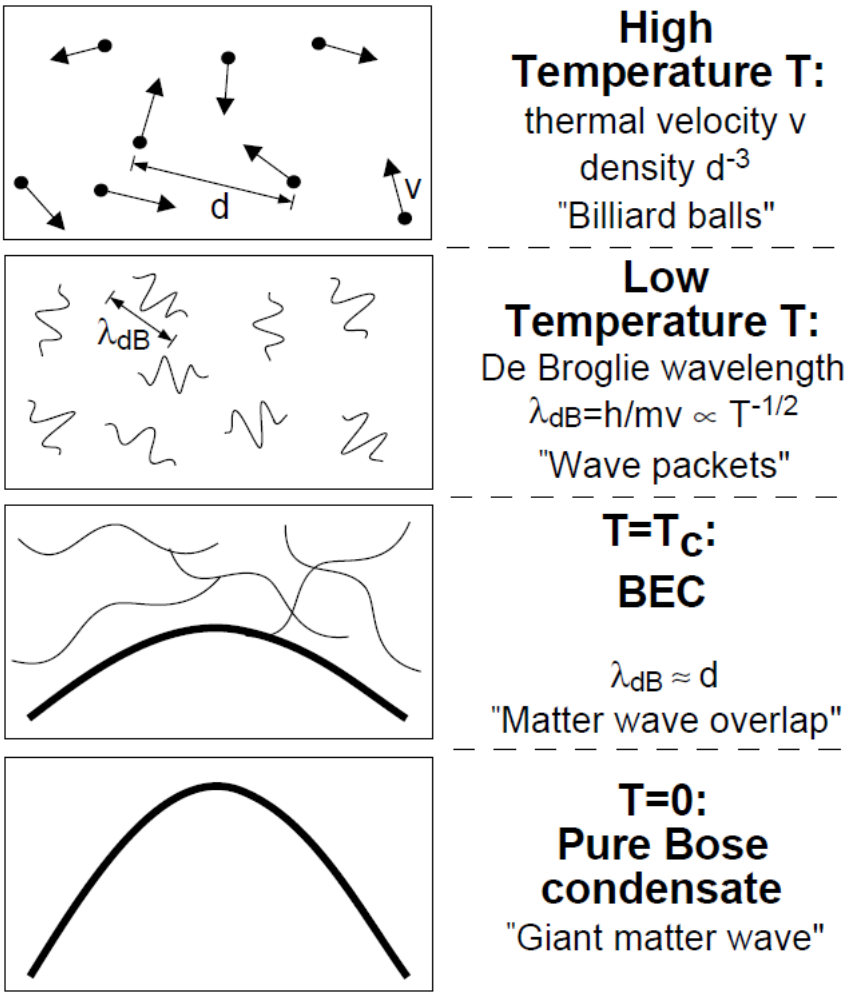

Figure 4.1: Schematic drawing of the atomic behaviour at different temperatures. The uppermost frame shows a classical gas at high temperature, in which the atomic interactions can be described analogously to billiard balls. At lower temperatures and high enough densities, the de Broglie wavelength becomes a relevant measure of the system (second frame), until at the critical temperature the matter waves overlap and build a Bose-Einstein condensate in the vibrational ground state of the system (third frame). A pure condensate as in the fourth frame only exists in the hypothetical case of zero temperature, but very high condensate fractions can already be achieved at finite temperatures (from [Ket99]).

by a mean-field approximation. The interaction is thence no longer the sum over all particle pairs, but is rather approximated by each particle experiencing the density distribution of the other particles, resulting in the effective single-particle non-linear Schrödinger equation, also called Gross-Pitaevskii equation [Gro61, Pit61]

$$\left(-\frac{\hbar^2}{2m}\Delta + V(r) + \frac{4\pi\hbar^2 a_{sc}}{m}|\Psi(r)|^2\right)\Psi(r) = E\Psi(r), \tag{4.2}$$

in which the third term of the energy sum represents the mean-field interaction. Δ is the Laplace operator. While a negative scattering length a_{sc}, denoting an attractive interaction, leads to a fast collapse of the condensate, atoms with a positive scattering length as in the case of calcium push each other apart due to the mean-field force. Thus the atoms are pushed into regions with higher potential energy and at the same time the kinetic energy due to Heisenberg uncertainty principle is reduced. This gives rise to the Thomas-Fermi approximation, which neglects the kinetic energy term:

$$\left(V(r) + \frac{4\pi\hbar^2 a_{sc}}{m}|\Psi(r)|^2\right)\Psi(r) = \mu\Psi(r). \tag{4.3}$$

The energy is then given by the chemical potential μ describing the energy needed to add one atom to the ensemble. This simplified equation allows for analytic solutions for the density distribution of the BEC in the form of

$$n(r) = |\Psi(r)|^2 = \frac{\mu - V(r)}{\frac{4\pi\hbar^2 a_{sc}}{m}}, \tag{4.4}$$

representing an inverse parabola for the approximately parabolic potential of a Gaussian trapping beam. The density reaches zero at the so-called Thomas-Fermi radius R_0, for which $V(R_0) = \mu$.
When the trapped ensemble is released, the atoms will be pushed apart by the mean field repulsion resulting in an expansion from which the chemical potential can be determined. Since the mean field repulsion is dependent on the gradient of the density distribution [Dav95], the atoms will expand faster along the stronger confined axis. This leads to a characteristic inversion of the aspect ratio during expansion, while thermal ensembles would approach an isotropic density distribution at large expansion times.

4.1.1 Peculiarities of calcium

Bose-Einstein condensates have been first achieved in 1995 with rubidium [And95], Lithium [Bra95] and sodium [Dav95]. Since then many experiments on phenomena such as interference [And97, Bon99], superfluidity [Mat99] and the Mott insulator transition [Gre02] have been performed. Also several more atom species have been condensed over the years: hydrogen [Fri98], metastable helium [Rob01], potassium

[Mod01], chromium [Gri05], caesium [Web03a] and ytterbium [Tak03]. However, until the BEC presented in this thesis no one ever achieved a BEC with an alkaline earth metal. Alkaline earth atoms are interesting candidates for condensation, because the two valence electrons lead to very narrow transitions between the singlet and the triplet system. These can be used for precise spectroscopy inside the condensate as well as the application of low loss optical Feshbach resonances [Ciu05] with the prospect to tune the scattering length. One has to mention ytterbium here, which has a similar electronic structure and thus shares the features of alkaline earth elements to some extend. However the width of the $^1S_0 - {}^3P_1$ intercombination transition in ^{174}Yb is 180 kHz [Toj06] and thus about 500-fold broader than in ^{40}Ca (374 Hz) [Deg05a], which reduces the suitability of ytterbium for the above-mentioned applications.
The reasons for not having achieved condensation with alkaline earth elements are just as numerous as the opportunities. The strongest cooling lines have wavelengths, which are not easily accessed with the simplest diode lasers, but rather demand for frequency doubling systems. The absence of sub-Doppler cooling mechanisms demand for a second MOT stage. Also magnetic traps, which achieve high trapping volumes, are not working for the zero-spin alkaline earth elements. ^{88}Sr features a vanishing scattering length, which prevents evaporation, whereas calcium in the metastable $^3P_2$ state shows high inelastic collisions [Han06], also making evaporation down to a BEC impossible. Finally, the trapping of calcium ground state atoms inside a dipole trap in 2007 has proven to be a promising precondition for successful evaporation [Gra07, Yan07]. In the next section I will discuss another difficulty occurring during evaporation: Large three-body losses compete with the evaporation process.

4.2 Three-body losses of dense calcium ensembles

A good precondition for the realization of a BEC is a repulsive interaction, which is represented by a positive scattering length a_{sc}. At ultracold temperatures most collisions between bosons are s-wave collisions and the collisional cross section can be written as $\sigma_{s-wave} = 8\pi a_{sc}^2$. The larger the scattering length the more collisions will take place and thus the faster thermalisation of the ensemble will happen. A large scattering length will thus make evaporation more efficient due to the fast evaporation and thermalisation rates. On the other hand a large scattering length typically leads to large three-body losses described by the differential equation

$$\dot{\rho} = -L_3 \cdot \rho^3 \tag{4.5}$$

with ρ the local atomic density. The three-body loss parameter L_3 scales with the fourth power of the scattering length for large a_{sc} [Fed96b, Nie99]. It fulfils the equation

$$L_3 = n_l \cdot C \frac{\hbar}{m} a_{sc}^4 \tag{4.6}$$

with $\hbar$ the reduced Planck constant, m the atomic mass and C varying between 0 and 68.4 due to interference effects of different scattering channels [Nie99] and n_l

denotes the number of lost atoms per scattering event.
We first observed three-body losses in a deep crossed dipole trap in an ensemble with a peak density of $\rho_0 = 1.4 \cdot 10^{14}$ cm^{-3}. We observed a faster than exponential decay (fig. 4.2a)). The measured points can be explained by a two-body decay as well as a three-body decay. Due to the absence of spin-changing collisions in the ^{40}Ca ground state, the only two-body loss effect would be evaporation, which can be ruled out due to the constant temperature of (27 ± 2) μK (see figure 4.2b)). The differential equation of the atom number is thus

$$\dot{N} = -\gamma N - \epsilon N^3 \tag{4.7}$$

with

$$\epsilon = L_3 \cdot \frac{< \rho^2 >}{N^2} \tag{4.8}$$

connected to L_3 via an atom number independent geometry factor. However the small amount of data points does not justify a fit with two loss parameters, so the atom number was just corrected for the amount of background losses that occurred during the measurement. A simple three-body loss function was then fitted to the points. The three-body loss coefficient was determined to be $L_3 = (3.2 \pm 1.6) \cdot 10^{-27}$ cm^6/s. This measurement has already been presented by [Vog09].
A later measurement with more data points was done. In this measurement however, atoms remained in the single beam wings of the crossed dipole trap and were constantly refilling the region of the crossed dipole trap during the first 500 ms. A fit considering three-body as well as background losses was performed only for data points of longer storage times (fig. 4.2 c)). The fit results in a three-body loss coefficient of $L_3 = (5.5 \pm 2.6) \cdot 10^{-27}$ cm^6/s, which is in agreement with the abovementioned measurement within the combined uncertainty. The measurement has been previously published in [Kra09]. Since evaporation could not be ruled out in this measurement, the value should be considered as an upper boundary and the value of the former measurement seems more trustworthy.
To illustrate the importance of three-body losses, a few comparisons can help. At the abovementioned peak density of $\rho_0 = 1.4 \cdot 10^{14}$ cm^{-3} the three-body losses are as high as they would be in a vacuum with about 5 ms lifetime due to background collisions. Also a comparison with the coefficients of other atom species can illustrate the importance of this loss mechanism. In ^{87}Rb it is $L_3(\text{Rb}) = 4.3 \cdot 10^{-29}$ cm^6/s [Bur97], in a condensate[1] of ^{23}Na atoms it was measured to be $L_3(\text{Na BEC}) = 1.1 \cdot 10^{-30}$ cm^6/s [Sta98]. Weber et. al. measured the three-body loss coefficient of ^{133}Cs. Using magnetic Feshbach resonances they varied the ground state scattering length. At a field of 7.5 mT they measured $L_3(\text{Cs}) \approx 1 \cdot 10^{-24}$ cm^6/s at a scattering length of 1200 a_0 [Web03b]. For the generation of the BEC they had to alter the scattering length to a lower value [Web03a]. The comparison of L_3 for the different atom species in dependence of their scattering length is displayed in figure 4.3. A fourth power fit similar to the fit in [Vog09] is shown along with the data, even though the scaling

[1] In Bose-Einstein condensed ensembles the three-body loss coefficient L_3 is predicted to be 8-fold smaller. This factor was experimentally confirmed by [Bur97].

should only be valid for large a_{sc}. The loss coefficient of calcium is lower than expected from the fit. A link between the constant $C = C(a_{sc})$ in equation (4.6) and Efimov physics has been recently developed [Kno12b], which is able to describe the three-body losses in metastable helium, ^{86}Sr and ^{168}Yb. However the same model still predicts larger three-body losses in ^{40}Ca than we observed [Kno12a], if reasonable values for the ground state scattering length are used.
Despite the loss coefficient being lower than expected, it is still very large, especially compared to other species with which Bose-Einstein condensates were achieved. Along with the typically higher densities in optical traps compared to magnetic traps, three-body losses pose a huge challenge for the successful evaporative cooling. Some methods to cope with these losses will be presented in the next section.

4.3 Forced evaporation scheme in a crossed dipole trap

The principle of evaporation is based on a thermally distributed ensemble in a trap of finite depth. High energetic atoms not confined by the trapping potential will leave the trapping volume. The energy distribution can be well-described by a truncated Maxwell-Boltzmann-distribution. Due to thermalising collisions further atoms can gain high enough energies to leave the trap. The trap depth is usually much larger than the average thermal energy, so each atom leaving the trap takes away more than average energy effectively cooling the remaining ensemble. This leads to the so-called plain evaporation, where the temperature decreases monotonically in a trap of constant depth and might eventually form a BEC. However, the rate of evaporation gets slower the lower the temperature gets compared to the trap depth. Since there are competing loss mechanisms like background gas collisions and three-body collisions, the cooling due to evaporation has to take place sufficiently fast. This can be assured by continuously lowering the trap depth to keep the evaporation rate high.
The design of the dipole trap and the ramping scheme for our experiment was motivated by several considerations. Firstly the tilted dipole trap was displaced by 7 mm along the axis to achieve a larger beam diameter of around 77 μm at the crossing region. This leads to lower densities and thus lower three-body losses, while the horizontal trap still forms a deep trapping potential. Secondly, to achieve a large trapping volume and a rather low density to avoid light assisted collisions during loading [Vog09] we start with an almost pure horizontal single-beam trap with negligible power in the tilted trapping beam. We then transform the trap into a crossed one by ramping down the power of the horizontal beam linearly by a factor of 3.6 and thus lowering the ratio of the intensities. The trap frequencies in this crossed dipole trap are high enough in all directions, enabling us to employ adiabatic ramps faster than the lifetime due to background gas collisions of about 5 s (at a pressure of $2 \cdot 10^{-9}$ mbar). The following ramps were chosen to be linear ramps of both beams with each ramp lowering the power by a factor of about 3. The duration of each ramp was optimized experimentally as follows:
For the optimization of the first ramp we chose a setup with two ramps with the

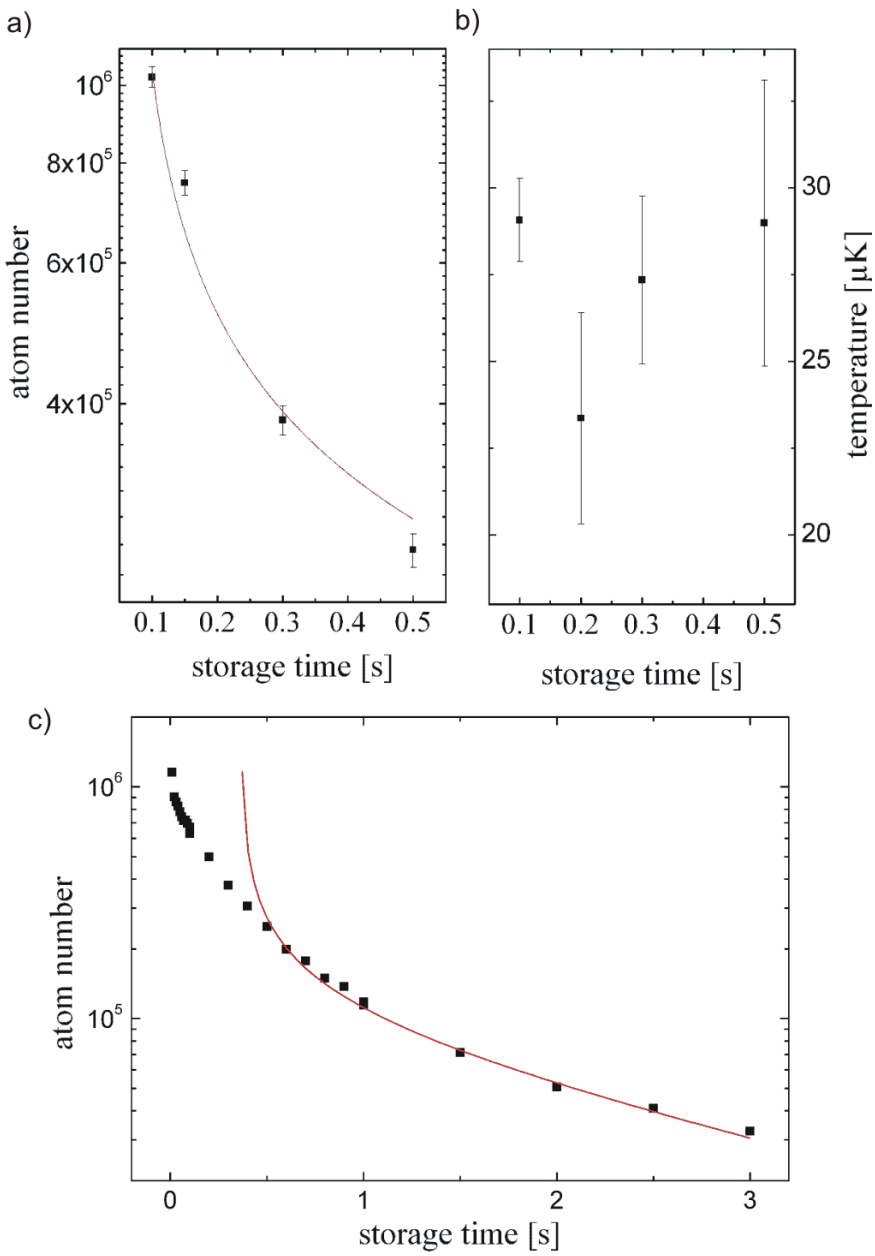

Figure 4.2: Different decay curves for the determination of the three-body loss coefficient L_3. In the first measurement (figure section a) and b)) the temperature of the ensemble was monitored as well to rule out losses due to evaporation. In the second measurement (figure section c)) many atoms were caught in the single-beam wings of the trap, constantly reloading the crossed region during the first 500 ms. To account for this effect the fit starts at 500 ms. The results of both measurement agree within their uncertainties. Since the upper measurement was done with less disturbing effects, its value of $L_3 = (3.2 \pm 1.6) \cdot 10^{-27}$ cm^6/s represents the better estimate.

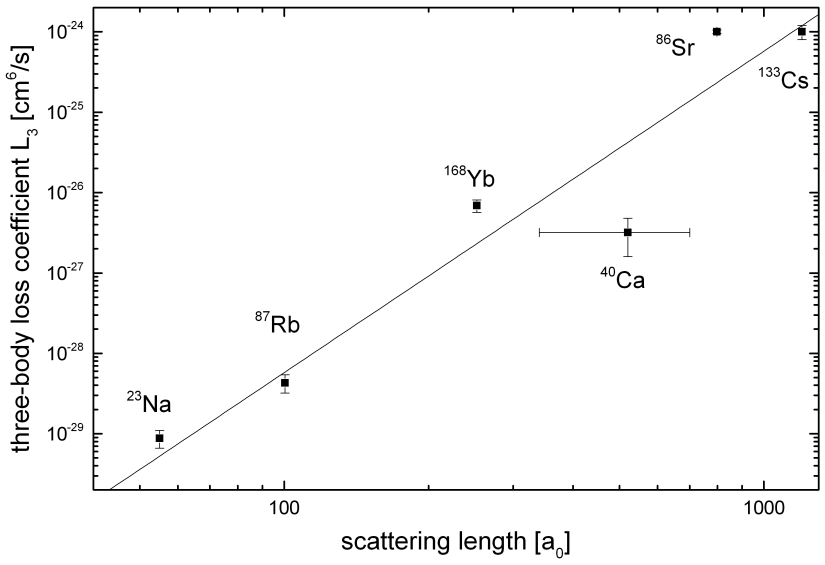

Figure 4.3: Comparison of the three-body loss coefficient L_3 for different atomic species in dependence of their ground state scattering length a_{sc}. $L_3(^{23}\text{Na})$ and $L_3(^{168}\text{Yb})$ have been multiplied by 8 to compensate for the fact, that they were measured inside a BEC. The scattering length of ^{133}Cs was tuned by a magnetic Feshbach resonance in a magnetic field of 7.5 mT. The solid line represents a scaling of L_3 with a power of 4 of the scattering length following equation (4.6), as predicted for large scattering lengths [Fed96b]. The values for the loss coefficients were taken from [Sta98] for ^{23}Na, [Bur97] (^{87}Rb), [Sug11] (^{168}Yb), [Fer06] (^{86}Sr), and [Web03b] (^{133}Cs).

second ramp sufficiently slow to assure thermal quasi-equilibrium at all times. The ramping time of the first ramp is then varied and optimized with respect to the maximum atom number after both ramps. This assures the first ramp to be as fast as possible to minimize competing background and three-body losses and as slow as necessary to ensure thermalisation and adiabaticity. An example of such an optimization is shown in figure 4.4. This procedure was done for each ramp where for each ramp except the first one both laser powers were reduced.

Figure 4.5 and table 4.1 show the results of the optimization of four consecutive ramps. The table also lists the corresponding parameters of the atom cloud. From the experience with BECs of other elements, one would expect the optimum ramping scheme being not very different from an exponential. Here this has been proven approximately right for all ramps except the second one. To get a qualitative view of the processes occurring during the second ramp, one has to take a closer look on the three-body collisions, which include dynamics that are rather unique in the case of ^{40}Ca.

In a three-body loss event a collision of three atoms result in the formation of a weakly bound dimer and the binding energy is released into kinetic energy. One third of this energy is taken away by the molecule and two thirds by the free atom to fulfil energy and momentum conservation. In a standard approach the molecule

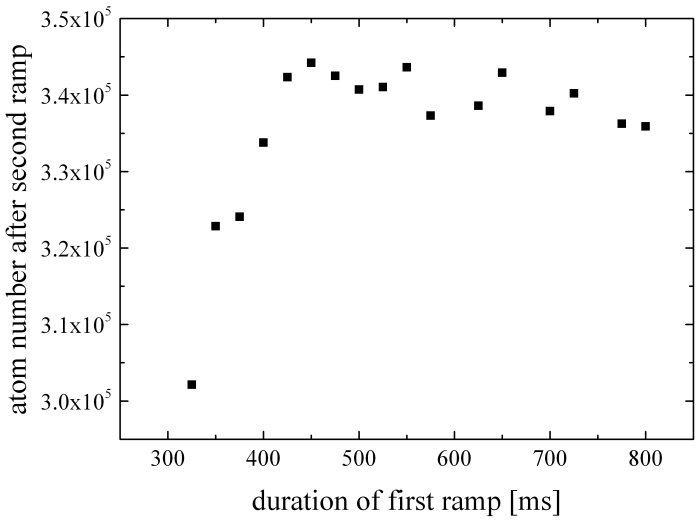

Figure 4.4: Example for the optimization of a ramping step. While the time for the first ramp was altered, the atom number after a second ramp was monitored. An optimum was found for about 450 ms. Faster ramps result in a non-adiabatic behaviour, which leads to a strong spilling of atoms and evaporational losses during the second ramp. For ramp times longer than 450 ms the atom number starts to decrease due to background gas collisions.

as well as the free atom are considered to be lost resulting in the loss of three atoms per scattering event accompanied by a slight heating effect due to the so-called "anti-evaporation" [Web03b]. However, the assumptions of the molecule as well as the atom being lost is only true for binding energies much larger than the trap depth. Connected to the large ground state scattering length, a ^{40}Ca dimer features a weakest bound level between $h \cdot 0.1$ MHz and $h \cdot 2$ MHz below the diatomic asymptote [All03]. In a deep trapping potential the atom and the molecule will be trapped, whereupon the highly excited molecule usually collides inelastically with another atom resulting in a total loss of three atoms. Before the inelastic collision the molecule as well as the atom will distribute the binding energy of the weakest bound level among the remaining ensemble. This will lead to additional evaporative losses, which are highest if the trap is only slightly deeper than the binding energy. In our experiment the second ramp lowers the trap depth from $h \cdot 0.9$ MHz to $h \cdot 0.3$ MHz, which is in the order of the binding energy. It is thus favourable to remain as short as possible in this regime, where three-body collisions lead to this additional losses.

trap parameters...	...after loading	...after 1st ramp	...after 2nd ramp	...after 3rd ramp	...after 4th ramp
duration of the ramp [ms]	350 (loading of ODT)	400	150	500	400
power (hor.) [W]	8	2.2	0.67	0.27	0.12
power (tilt.) [W]	2.5	2.5	0.83	0.35	0.13
trap depth [μK]	175	48	14.6	6.0	2.6
atom number	$2.6 \cdot 10^6$	$6.5 \cdot 10^5$	$4.4 \cdot 10^5$	$2.3 \cdot 10^5$	$1.2 \cdot 10^5$
temperature [μK]	21	6.8	2.4	0.7	0.23
phase space density	$1.4 \cdot 10^{-3}$	$3.6 \cdot 10^{-2}$	$9.7 \cdot 10^{-2}$	$5.4 \cdot 10^{-1}$	2.2

Table 4.1: Parameters of the dipole trap and the atomic ensemble after loading from the second stage MOT and after each ramping step. Each ramp was optimized as described in the text.

4.4 Creation of a BEC

4.4.1 Bose-Einstein condensation in a crossed dipole trap

As noted in table 4.1, the critical phase space density of 1.2 was achieved and surpassed after the fourth ramp. The formation and growth of the BEC could be observed during a fifth ramp. On the day of the first realization of a BEC we were using a different ramping scheme than described in section 4.3, which featured more power in the tilted trap. The power at the edges of the five ramps was 6 W/2 W/0.67 W/0.27 W/0.12 in the horizontal trap and 5 W/5 W/ 1.67 W/0.56 W/0.19 W/0.06 W in the tilted trap. The optimization led to significantly shorter ramping times than presented in section 4.3 of 500 ms/60 ms/100 ms/ 125 ms and 350 ms. The condensate showed up as a small dot in the centre of the density distribution on the absorption images. Interpreting this slowly expanding dot as a thermal cloud would require to assume very low temperatures of around 10 nK and hence phase space densities of more than 1000. Additionally a Gaussian fit does not represent the density distribution well. Figure 4.6 shows the optical column density in a 3D false colour plot, which clearly reveals the bimodal nature of the density distribution. The picture was taken after ramping down 65 % of the fifth ramp.

Figure 4.7 shows absorption images at different final values of the dipole trap powers. The corresponding optical density distributions along the vertical axis are displayed together with a Gaussian fit to the thermal fraction of the atoms, from which the temperature was determined. In figure 4.7b) the onset of a BEC is visible. The corresponding atom number is $N = 8.1 \cdot 10^4$ and the angular trap frequencies are 240 s^{-1}, 900 s^{-1} and 1320 s^{-1}, leading to a critical temperature of $T_C = 170$ nK according to equation (4.1), which is in excellent agreement with the measured 170 nK. While the typical atom number is $7 \cdot 10^4$ to $1 \cdot 10^5$, when the critical temperature is reached, the actual number of atoms, that populate the ground state and represent the BEC fraction hardly exceeds $1.5 \cdot 10^4$.

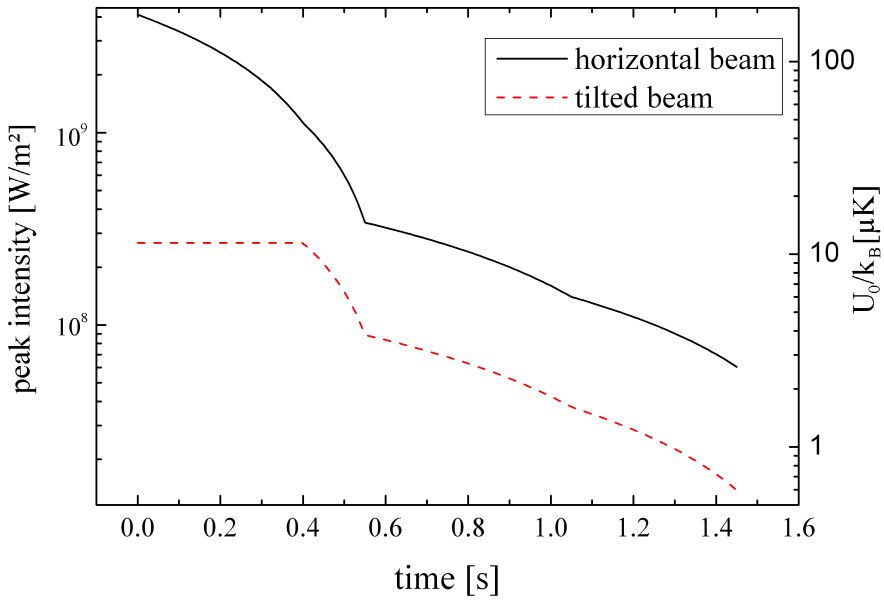

Figure 4.5: Dipole trap beam intensities during the ramp down to quantum degeneracy after optimization as described in the text. We attribute the deviation from an exponential ramp during the second step to additional losses resulting from the energy gained during a three-body collision being in the order of the trap depth (see text).

The ramping scheme on the day of the first realization of a BEC led to a large number of condensed atoms within an evaporation time of 1.1 s. However a large amount of three-body losses made this fast ramping necessary. These three-body losses preclude condensation if the starting atom number is lower. A more robust ramping scheme was applied later, which featured a lower power in the tilted trap. The resulting lower densities result in lower three-body losses and thus grants us more time to run the evaporation at a higher efficiency. The optimization led to the ramps presented in section 4.3. The condensate was formed during a fifth ramp of 50 ms down to the power of 75 mW and 45 mW in the horizontal and tilted trap, respectively. The total evaporation time was 1.5 s. The experiment of the mean-field expansion presented in the next section was done with this optimized ramping scheme and 40 % of the fifth ramp were applied leading to a final power of 98 mW in the horizontal beam and 96 mW in the tilted beam.

Mean-field expansion

Two of the identifying features of a BEC like the high phase space density and the bimodal Gaussian/parabolic density distribution have already been presented above. Another strong evidence for a BEC is the inversion of the aspect ratio during expansion. We measured the radii of the BEC fraction (the cutting edge of the parabolic part of the density distribution) of an expanding atomic ensemble (figure 4.8). The

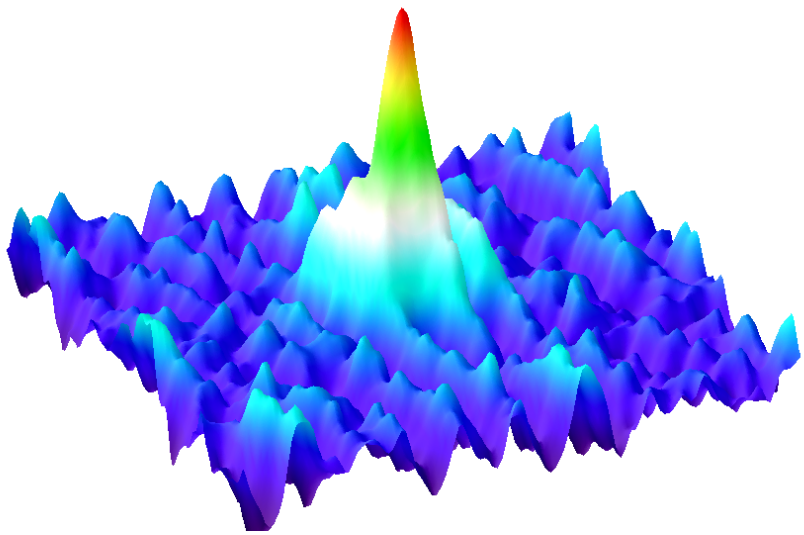

Figure 4.6: False colour 3D plot of the atomic density distribution after 7 ms of expansion. Plotted is the optical column density in dependence of the position in the imaging plane. A clear bimodal distribution is visible with a Gaussian distributed thermal underground and a striking parabolic peak representing the BEC fraction. The rippled underground structure is a result of speckles and interferences in the absorption laser beam.

atoms along the formerly tighter confined vertical axis are expanding with a velocity of 4.8 mm/s and thus faster than the atoms along the horizontal axis (2.1 mm/s). This leads to the typical inversion of the aspect ratio. The dipole trap powers are 98 mW in the horizontal beam and 96 mW in the tilted beam. In contrast to the horizontal axis of the image, the vertical axis corresponds approximately to a vibrational axis of the trap and can be used for further quantitative investigation. Considering the gravitational sag the vertical trap frequency can be calculated to $\omega_v = 870$ s^{-1}. The ordinate intercept of 6.5 μm represents the Thomas-Fermi radius inside the trap, which can be calculated by

$$R_0 = \sqrt{\frac{2\mu}{m_{Ca}\omega_v^2}}. \tag{4.9}$$

From this we can calculate the chemical potential to be $\mu/k_B \approx 75$ nK. A more exact way to determine the chemical potential is considering the expansion rate, which can be observed with higher accuracy than the radius inside the trap. The radius of the parabolic part of the density distribution should expand according to [Ket99]

$$R(t) = R_0 \cdot \sqrt{1 + \omega_v^2 t^2} \approx \sqrt{\frac{2\mu}{m_{Ca}}} \cdot t, \tag{4.10}$$

where the approximation is valid for long expansion times and cigar-shaped BECs, which is only roughly given in our case of the crossed dipole trap. The expansion rate of 4.8 mm/s thus leads to a chemical potential of $\mu/k_B = 55$ nK. This value will

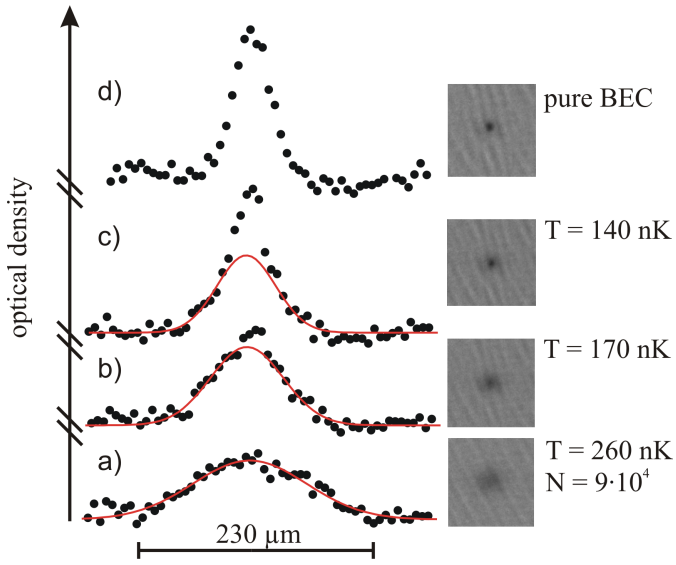

Figure 4.7: Absorption images of the atomic ensemble 7 ms after release from a crossed dipole trap of different trap powers. The plots show the optical density distribution along the vertical axis after integration along the other two dimensions. a) The lowest picture shows a thermal cloud of $9 \cdot 10^4$ atoms. For this picture we ramped down 10 % of the fifth ramp to a final power of 0.12 W/0.17 W in the horizontal/tilted dipole trap beam, resulting in a trap depth of $k_B \cdot 0.8$ μK. b) After applying 40 % of the fifth ramp down to 0.10 W/0.14 W the ensemble shows the onset of a BEC at a temperature of 170 nK. The trap depth is $k_B \cdot 0.6$ μK. c) After applying 70 % of the fifth ramp, a clear bimodal distribution is visible at a temperature of 140 nK. The final powers and trap depth are 90 mW/99 mW and $k_B \cdot 350$ nK. d) Further lowering the trap depth to $U_0/k_B = 140$ nK (final power 75 mW/62 mW) results in an almost pure BEC of $1.5 \cdot 10^4$ atoms.

be used for the following calculations.
The chemical potential is connected to the scattering length via the Gross-Pitaevskii equation (4.3) to

$$a_{sc} = \frac{(2\mu)^{5/2}}{15N\hbar^2\bar{\omega}^3\sqrt{m_{Ca}}} = 440a_0, \tag{4.11}$$

which is in good agreement with values from photoassociation [Vog07] and classical molecular spectroscopy [All03]. Due to the large uncertainties in atom number, chemical potential and furthermore the trap frequencies, this confirms the previous results, but should not be seen as an improvement on the value of the scattering length.
Another length scale, that can be derived from the chemical potential is the healing length of the BEC. It describes the smallest length scale of patterns and structures inside the BEC, before these patterns wash out. It can be calculated to [Ket99]

$$\xi = \frac{\hbar}{\sqrt{2m_{Ca}\mu}} = 330 \text{ nm}. \tag{4.12}$$

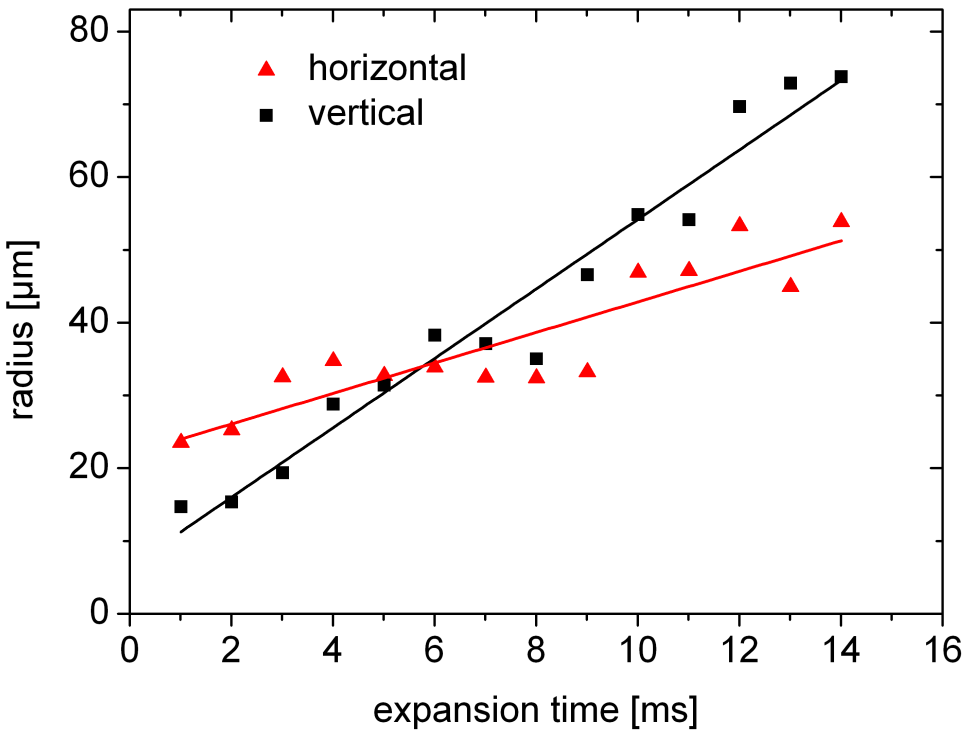

Figure 4.8: Expansion of the radii of the condensate along the vertical and horizontal direction after release from a crossed dipole trap. While a thermal ensemble would approach an isotropic distribution for long expansion times, the inversion of the aspect ratio caused by the mean-field force is a typical signature of Bose-Einstein condensates. From the fits we get expansion rates of 4.8 mm/s and 2.1 mm/s along the vertical and horizontal direction, respectively.

4.4.2 Bose-Einstein condensation in a single-beam dipole trap

The achievement of the calcium BEC in the crossed dipole trap was a great breakthrough and has proven the possibility of the condensation of calcium. While the crossed trap has advantages like the fast ramping due to high trap frequencies, a BEC in a single beam trap promises some advantages on its own: On the one hand the larger trapping volume enables higher atom numbers without inducing excessive three-body losses. The other advantage of a single beam trap is the clearly defined quantization axis in the absence of magnetic fields. The vectorial fraction of the light shift can be described as a fictitious magnetic field along $\vec{E} \times \vec{E}^*$, where $\vec{E}$ is the complex polarization vector. In a circularly polarized laser beam it points along the propagation axis. In the crossed dipole trap with slightly different optical frequencies the direction of the vector is not only dependent on the angle between the traps but also on the ratio of intensities of the traps, which is spatially varying. Spectroscopy inside the trap using the narrow intercombination line thus demands for a condensate in a single beam trap for a simplification of the geometrical effects involved.

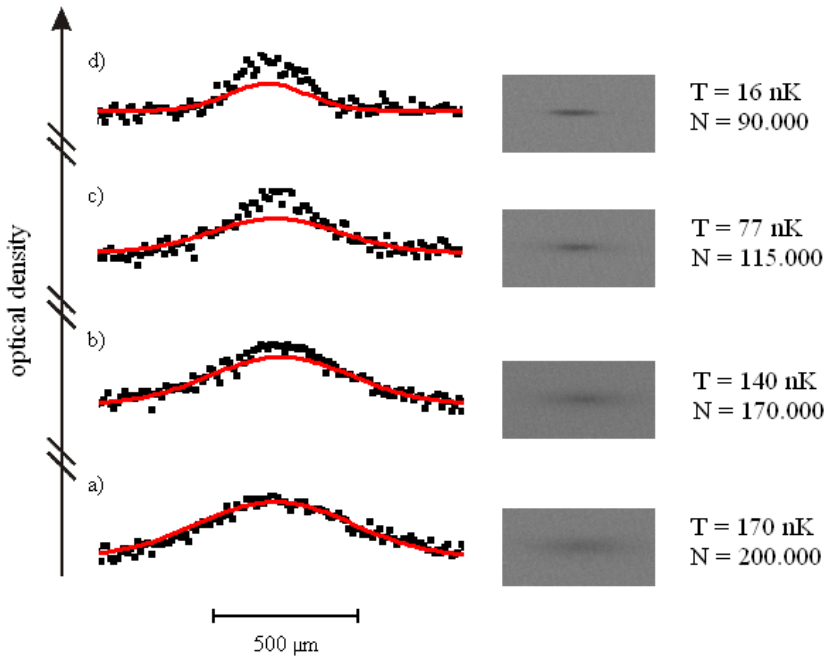

Figure 4.9: The plots show the optical density distribution along the dipole trap axis after integration along the two radial dimensions. The (red) solid lines indicate the Gaussian fraction of a bimodal fit. The corresponding absorption images are displayed as well. a) shows a thermally distributed ensemble at 170 nK. The final power of the ramp was 0.3 W, resulting in a trap depth of $k_B \cdot 2.7$ μK. In b) the onset of a BEC is visible at a temperature of 140 nK in a $k_B \cdot 1.9$ μK deep trap (final power 0.25 W). c) shows a clear bimodal distribution of 77 nK in a $k_B \cdot 0.9$ μK deep trap (final power 0.18 W). The BEC fraction is about 20 %. In d) the density distribution is still bimodal in a trap of 0.12 W, resulting in a trap depth of $k_B \cdot 230$ nK. Around $40\,000$ atoms form the BEC fraction. The measured temperature of 16 nK has a high uncertainty, because the fit routine had problems to distinguish the thermal and BEC fraction along the tightly confined axis.

We achieved a condensate in a single-beam trap using the same technique for the optimization of the evaporation scheme. The ramping scheme was dependent on the desired final power. We applied two ramps from 9 W to 2 W and further down to 0.6 W within 1.5 s each and a third ramp to the desired final power within 1.2 s followed by a thermalization stage of 1.2 s. For final powers lower than 0.2 W we ramped down to 0.2 W in the third ramp followed by a fourth ramp of 1 s and a thermalization stage of 0.2 s. The slower ramps compared to the crossed dipole trap setup are a consequence of the low axial trap frequency. Thermalization along the axis can only be assured by a sufficiently slow ramping scheme. The beam waist of the trap was around 38 μm and thus wider than in the previous experiments (33 μm). Fig. 4.9 shows the optical density distribution along the dipole trap axis above and below critical temperature along with the Gaussian fraction of a bimodal fit. While the optical density could also be fitted by a Gaussian distribution alone to reasonable

accuracy, the resulting temperatures would be extremely low and result in a phase space density of up to 100. This physically unlikely result justifies the assumption of a bimodal distribution. The onset of a BEC is visible at a temperature of 140 nK, whereas the calculated critical temperature according to formula (4.1) is 80 nK. The difference of about 40 % between the two values can result from uncertainties in the atom number or the temperature measurement itself. In addition some approximations had to be made calculating the trap frequencies in a potential significantly distorted by gravity.

As in the crossed trap we measured a high phase space density and a bimodal distribution as clear evidence of a BEC. Figure 4.10 shows the radii during the expansion of the BEC. The cloud expands a lot faster along the more strongly confined direction. This would lead to an inversion of the aspect ratio for longer expansion times. The inversion could not be observed as the Thomas-Fermi radius along the dipole trap axis is more than 200 μm even before the expansion starts. The stronger confined dimension of the ensemble expands a lot faster, but reaches only 100 μm after 25 ms before it falls out of the region that we can observe with our absorption imaging setup.

If we estimate the chemical potential from the expansion rate of 3.9 mm/s in the vertical direction, we obtain $\mu/k_B = 36$ nK according to formula (4.10), which would lead to a scattering length of $a_{sc} = 1640\ a_0$ with formula (4.11). The strong deviation from the value in the crossed trap as well as independently determined values [All03, Vog07] can be attributed to the high density of thermal atoms, which also contribute to the mean-field, but has been neglected in the calculations. In addition the trap geometry has changed since the determination of the trap frequencies (chapter 3.2) and its actual parameters are less well known.

In conclusion we achieved a Bose-Einstein condensate in a crossed as well as in a single-beam dipole trap. While the advantages of the single-beam setup are a clear quantization axis as well as a higher condensate atom number due to the larger trapping volume, it comes at the price of longer evaporation times. Additionally the critical temperature is lower due to the lower density. This makes a ramping down to lower trap powers necessary and results in a stronger distortion by the gravitational force, which complicates the geometric modelling of the trapping region.

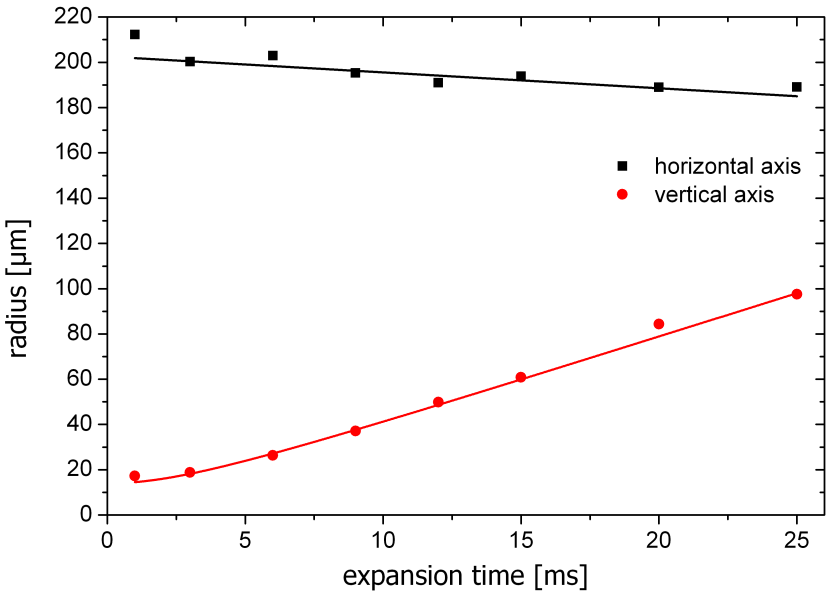

Figure 4.10: Expansion of the radii of the condensate along the vertical and horizontal axis after release from a single beam trap. The expansion along the vertical axis can be determined to 3.9 mm/s from the fit. An inversion of the aspect ratio could not be observed due to the condensate falling out of the imaging area after 25 ms. The slight contraction along the horizontal axis might result from fit uncertainties of the bimodal fit or indicate a collapsing condensate due to atom losses in the central region.

Chapter 5

Photoassociation at the Intercombination Line

Some of the most interesting future applications and experiments above and below quantum degeneracy of calcium employ optical Feshbach resonances. A measure of the applicability of optical Feshbach resonances is the achieved variation of the scattering length in comparison to the light induced losses. This ratio is predicted to be larger for Feshbach resonances close to a narrow atomic transition [Fed96a]. Calcium is a very good candidate for efficient variation of the scattering length due to the narrow 374 Hz intercombination line $^1S_0 - {}^3P_1$, which is about 20-fold narrower than the correspondent line in ^{88}Sr, but still strong enough for nearby molecular states to be excited. For the application of Feshbach resonances a detailed understanding of the coupling between pairs of free ground state atoms and excited molecular states via laser light is mandatory, which can preferentially be investigated by photoassociation spectroscopy. In the course of this work, the weakest bound molecular states in two attractive molecular potentials near the $^1S_0 + {}^3P_1$ asymptote have been found. In this chapter I will present the measurement of the frequency difference between those states and the diatomic asymptote and discuss their coupling to an external magnetic field as well as the line shape of the transition to these states.

5.1 Basic theory of Ca_2 molecules and their light assisted generation

5.1.1 Multipole expansion of molecular potentials

Neutral atoms at a given distance to each other can interact by several mechanisms. The longest range interaction is the dipole-dipole interaction with a scaling law of $1/R^3$, with R being the interatomic distance. This interaction is based on the exchange of a photon between the atoms and thus only exists between ground and excited state atoms of the same species. It directly scales with the square of the dipole matrix element between the wavefunctions of the two interacting atoms and

is thus proportional to the transition rate between the two states. In the case of two calcium atoms in the $^1S_0$ and $^3P_1$ state, respectively, this interaction is weak, connected to the narrow linewidth of the transition of 374 Hz.
The next higher orders of interactions can be summarized as van der Waals interactions. They origin from spatial fluctuations of the electron cloud and spontaneous generation of multipoles, which can induce other multipoles in neighbouring atoms. The most relevant terms at large interatomic separation are the induced dipole-dipole interaction, scaling with $1/R^6$, and the induced quadrupole-dipole interaction with a scaling of $1/R^8$. The long range molecular potential can be approximated as a sum of inverse powers

$$V(R) = -\sum \frac{C_n}{R^n}. \tag{5.1}$$

The leading coefficients C_3, C_6 and C_8 can be calculated by theoretical models [Mér01, Ciu04, Mit08], some of them using experimentally determined oscillator strengths. Higher order coefficients and the short distance potentials can not be derived so easily due to the overlap of the electronic clouds and the connected complexity of the interactions. For the short and medium range interactions the potential is usually modelled by a fit to the results of bound-state bound-state molecular spectroscopy as done e. g. by [All05] for Ca_2.

5.1.2 Hund´s coupling cases in homonuclear molecules

The molecular axis of a diatomic molecule is breaking the rotational symmetry of the atomic wavefunctions. Especially aspheric components of the wavefunction such as the p orbital of the excited state can assume certain orientations with respect to the molecular axis. At long interatomic distances this gives rise to two dipole-dipole potentials. At shorter distances the coupling of various angular momenta becomes more complex. Depending on the strength of the Hamiltonian that couples the angular momenta, a set of approximately conserved quantities can be chosen to describe the molecular state. The sets of approximately conserved quantities correspond to the various Hund´s coupling cases, which are discussed in [Bro03, p. 224 ff.]. For homonuclear molecules as investigated in this thesis Hund´s coupling cases (a), (c) and (e) are of relevance. They will be summarized shortly in the following text and visualized in figure 5.1.

Hund´s coupling case (a)

In Hund´s coupling case (a), the total atomic angular momenta $\vec{L}$ and $\vec{S}$ each precess around the molecular axis. Due to the strong anisotropic electric field of the two nuclei, $\langle \vec{L}^2 \rangle$ is no longer a preserved quantity, but its projection Λ to the molecular axis. The spin quantum number S as well as its projection Σ to the molecular axis are preserved. The sum of the projections to the molecular axis is $\Omega = \Lambda + \Sigma$. Ω and the angular momentum of the molecule´s nuclear rotation $\vec{R}$ sum up to the total angular

momentum $\vec{J}$, which should not be confused with the total atomic angular momentum $\vec{L} + \vec{S}$, which is here denoted $\vec{J}_a$ and which does not lead to a good quantum number in Hund´s case (a). The molecular states are denoted ${}^{2S+1}\Lambda^{+/-}_{\Omega_{g/u}}$, where g/u is the $gerade$ or $ungerade$ parity of the wavefunction when substituting $\vec{r}$ by $-\vec{r}$ and $+/-$ denotes the parity when mirroring the wavefunction on a plane in which the molecular axis lies. The parity $+/-$ is only relevant for $\Lambda = 0$ states and the index Ω is not always denoted.
While in atomic physics the states of angular momenta $L = 0, 1, 2, ...$ are denoted $S, P, D, ...$, in molecular physics the states of different angular momentum projections $\Lambda = 0, 1, 2, ...$ are denoted analogously in capital Greek letters $\Sigma, \Pi, \Delta, ...$, where Σ should not be confused with the spin projection also denoted Σ.
Hund´s coupling case (a) states are a good representation of molecules, if the binding energy is large compared to the spin-orbit coupling. It also holds only for small rotational energies, which is usually well satisfied for molecules at low temperatures.

Hund´s coupling case (c)

In Hund´s coupling case (c) the asymmetric potential along the molecular axis is not strong enough to break the L-S-coupling. This is the case if the spin-orbit coupling, represented by the coupling constant A is large compared to the binding energy of the molecule. In Hund´s case (c) the atomic angular momentum J_a represents a good quantum number as well as its projection to the molecular axis Ω. Ω and the molecular rotation $\vec{R}$ then sum up to the total angular momentum $\vec{J}$. Due to Λ, S and Σ not defined well in Hund´s case (c) the molecular states are denoted $\Omega^{+/-}_{g/u}$ with the symmetry quantum numbers $gerade/ungerade$ and $+/-$ as described above.
As the molecular states examined in this thesis are comparably weakly bound, they can be well described by Hund´s case (c). The states of Hund´s coupling case (a) however build a basis system, so that the near-asymptotic states can be developed in case (a) states as done by [Mie78].

Hund´s coupling case (e)

Though not identified by Friedrich Hund, another coupling case is named after him, Hund´s coupling case (e). In this case the molecular binding energy is so weak, that there is no precession of $\vec{J}_a$ around the molecular axis. Instead $\vec{J}_a$ and the molecular rotation $\vec{R}$ sum up to the total angular momentum $\vec{J}$. A symbolic drawing of the vector coupling in Hund´s cases (a), (c) and (e) is shown in figure 5.1.

5.1.3 Selection rules

The electronic selection rules known from atomic transitions are also valid for molecules. This leads to singlet-triplet transitions being spin-forbidden and thus very

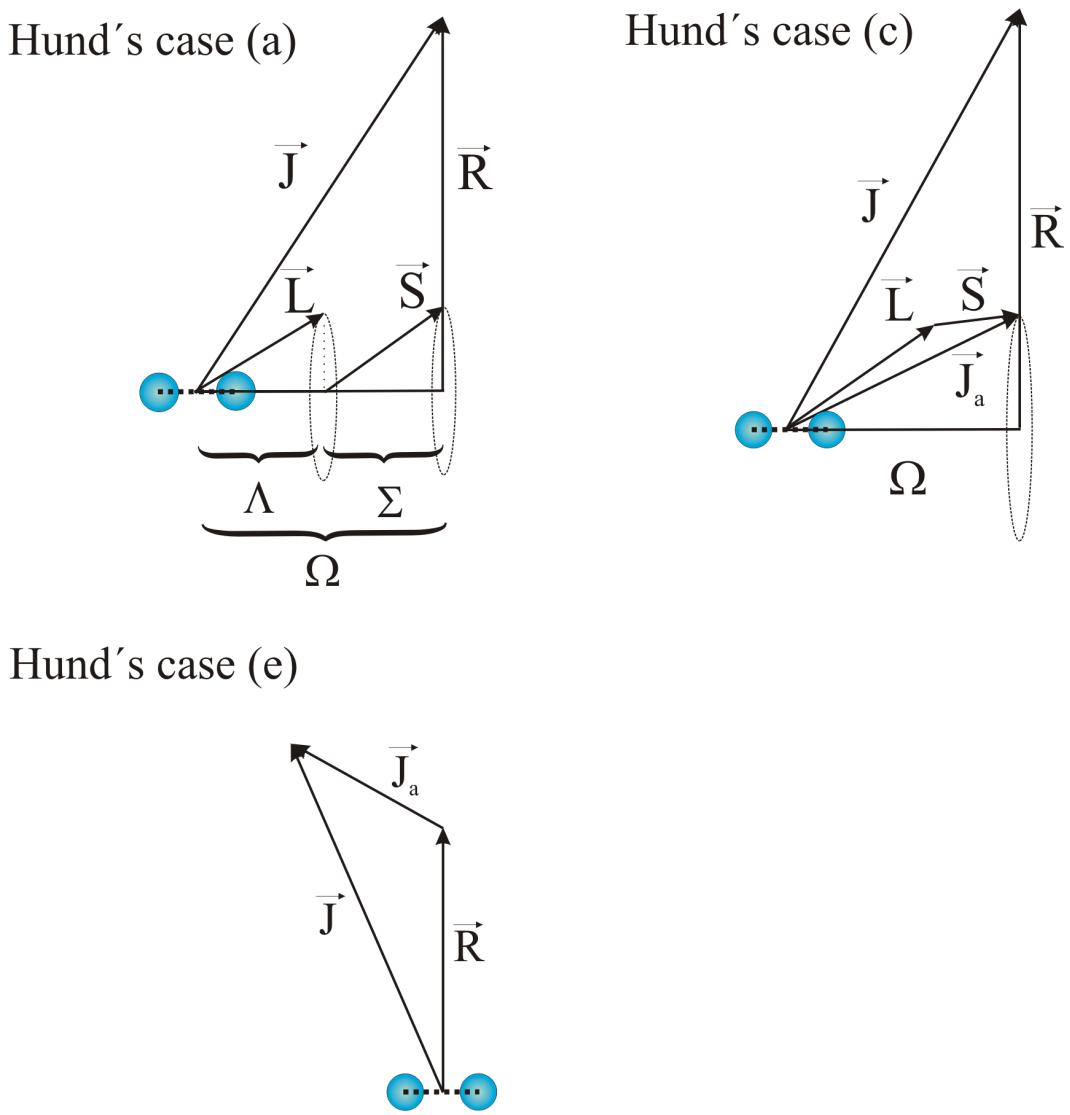

Figure 5.1: Schematic overview of the coupling of angular momenta in a molecule for different Hund´s coupling cases. In Hund´s coupling case (a) the atomic orbital and spin angular momenta $\vec{L}$ and $\vec{S}$ precess around the molecular axis. The projections to the axis are called Λ and Σ, respectively, and their sum is Ω. This projected angular momentum Ω and the rotation of the molecule $\vec{R}$ sum up to the total angular momentum $\vec{J}$. In Hund´s coupling case (c) $\vec{L}$ and $\vec{S}$ couple to the total atomic angular momentum $\vec{J}_a$. Its projection Ω to the molecular axis and the rotation $\vec{R}$ sum up to $\vec{J}$. In Hund´s coupling case (e) the total atomic angular momentum $\vec{J}_a$ couples directly with the rotation $\vec{R}$ to the total angular momentum $\vec{J}$.

narrow. Molecules however have some additional selection rules.
The rotational barrier for d-wave scattering is in the order of $k_B \cdot 2$ mK and thus much larger than the thermal energy at $1\ \mu$K. Hence only s-wave scattering between unbound ground state atoms is possible. The angular momentum between two ground state atoms as well as their electronic angular momentum being zero, a photon (with an angular momentum of 1) can only excite into molecular states, which have a total angular momentum of $J = 1$. Additionally, since the ground state is a $gerade$ state, we can only excite $ungerade$ states by electric dipole transitions [Her50].

5.1.4 Molecular potentials a and c

As said in section 5.1.1, the interaction potential depends on the ability of the atoms to induce a multipole in the neighbouring atom. This polarizability however depends on the orientation of nonspheric components of the atoms such as p-orbitals and can thus differ depending on the quantum numbers Λ and Ω.
Two attractive $ungerade$ potentials exist near the diatomic asymptote $^1S_0 + {}^3P_1$. They are historically denoted with small letters a and c. These molecular potentials are $a^3\Sigma_u^+$ and $c^3\Pi_u$ in Hund´s coupling case (a). The potential curves have been determined by [All05] by molecular spectroscopy and are schematically presented in figure 5.2. Since in Hund´s coupling case (a) there is no spin-orbit splitting, the molecular potential $a^3\Sigma_u^+$ does not coincide with an atomic energy at long interatomic distance. The near-asymptotic behaviour is better described by Hund´s case (c). The diatomic state $^1S_0 + {}^3P_1$ splits into the molecular states 0_u^+ and 1_u. The 0_u^+ can be expressed as $^3\Pi_{0_u}$ in the basis of Hund´s case (a) eigenvectors [Mie78]. While the 1_u changes its character to $^3\Sigma_u^+$ at small nuclear separations, near the asymptote it can be expressed as $1/\sqrt{2} \cdot ({}^3\Sigma_{1_u}^+ - {}^3\Pi_{1_u})$.
In the energy range investigated in this work, the relevant terms in the potentials are long range terms proportional to $1/R^3$, $1/R^6$ and $1/R^8$. The two potential curves will be denoted as

$$V_{0_u} = D - C_{3,0_u}/R^3 - C_{6,0_u}/R^6 - C_{8,0_u}/R^8 \tag{5.2}$$

and

$$V_{1_u} = D - C_{3,1_u}/R^3 - C_{6,1_u}/R^6 - C_{8,1_u}/R^8. \tag{5.3}$$

D denotes the molecule dissociation energy and is thus the energy of the diatomic asymptote. The coefficients C_3 are directly related to the dipole matrix element of the $^1S_0 - {}^3P_1$ transition and can be expressed in terms of the lifetime τ and the transition angular frequency ω [Zel06] as $C_{3,0_u} = -2 \cdot C_{3,1_u} = \frac{3\hbar c^3}{2\tau\omega^3} = h \cdot 6.42 \cdot 10^8$ Hz nm^3. The coefficients C_6 are derived by various authors [Ciu04, Mit08] with theoretical methods based on experimentally determined line strengths. Though using different methods of calculation the results differ by only about 3 %. In this work I will use the values of [Mit08], who also gave values for the C_8 coefficients. An overview of the coefficients for the different potential curves is given in table 5.1. Several units are used for the C_n coefficients such as atomic units $E_H\ a_0^n$ with the Hartree energy $E_H = 4.38 \cdot 10^{-18}$ J and the Bohr radius $a_0 = 0.053$ nm, or spectroscopic units

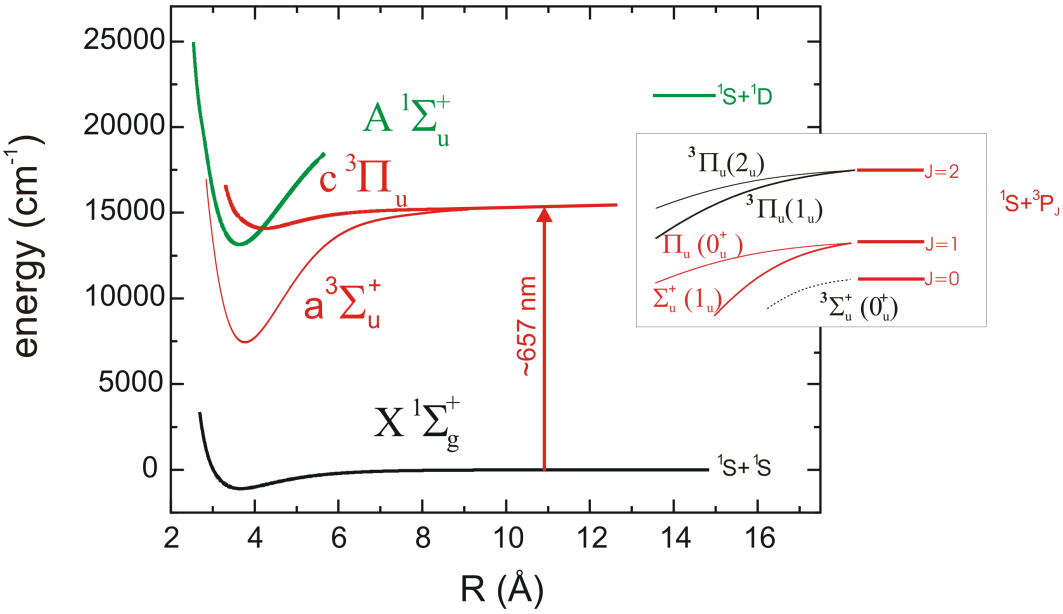

Figure 5.2: Molecular potentials relevant for this work sketched from the potential parameters given in [All05]. The inlay on the right side schematically shows the splitting of the ^3P manifold into different *ungerade* molecular potentials near the atomic asymptote.

	C_3 / (h·Hz nm^3)	C_6 / (h·Hz nm^6)	C_8 / (h·Hz nm^8)
0_u^+	$6.4 \cdot 10^8$	$3.7 \cdot 10^{11}$	$7.8 \cdot 10^{10}$
1_u	$-3.2 \cdot 10^8$	$3.9 \cdot 10^{11}$	$2.0 \cdot 10^{10}$

Table 5.1: Potential coefficients for the molecular states 0_u^+ and 1_u. C_6 and C_8 are given by [Mit08] for Hund´s case (a) and are calculated for case (c) by $C_{n,0_u^+} = C_{n,^3\Pi}$ and $C_{n,1_u} = \frac{1}{2}(C_{n,^3\Pi} + C_{n,^3\Sigma})$ according to [Mie78]. For a list of C_n coefficients calculated by other authors see [Mit08].

cm$^{-1} \cdot \mathring{A}^n$ using the wavenumber as an energy scale. I decided to use the unit $h \cdot$ Hz nm^n, which is closest to the international system of units.
In addition to the potential energy, the molecules have a rotational energy, which can be included in an effective potential. The energy of the nuclear rotation is

$$E_{rot} = \frac{\hbar^2}{2\mu R^2} \cdot \langle \vec{R}^2 \rangle \tag{5.4}$$

where μ is the reduced mass and $\vec{R}$ is the angular momentum operator, which can be written as [Ves74, Lef04]

$$\langle \vec{R}^2 \rangle = \langle (\vec{J} - \vec{J}_a)^2 \rangle = J(J+1) + J_a(J_a+1) - 2\Omega^2. \tag{5.5}$$

Since $J_a = 1$ the effective potentials are then

$$V_{0_u} = D - C_{3,0_u}/R^3 - C_{6,0_u}/R^6 - C_{8,0_u}/R^8 + \frac{\hbar^2}{2\mu R^2} \cdot (J(J+1) + 2) \tag{5.6}$$

and

$$V_{1_u} = D - C_{3,1_u}/R^3 - C_{6,1_u}/R^6 - C_{8,1_u}/R^8 + \frac{\hbar^2}{2\mu R^2} \cdot J(J+1). \tag{5.7}$$

5.1.5 Photoassociation spectroscopy near the intercombination transition

The possible energies in the molecular potential are quantized. While the molecular potentials can reach depths of more than 100 THz, in photoassociation spectroscopy typically the weakest bound states are excited. The reason is the overlap between the ground state scattering wavefunction and the molecular state, the so-called Franck-Condon density. Classically the ground state atoms with relatively low velocity are strongly accelerated by the attractive molecular potential, effectively reducing the time, during which the atoms have a low interatomic separation. Quantum mechanically this results in a low amplitude of the wave function for small distances. The wavefunctions of deeply bound molecules however have their maximum amplitude at small distances. With the overlap of the wavefunctions the excitation probability of deeper lying states gets smaller.
In photoassociation spectroscopy a laser red-detuned to the atomic transition is applied to the atom cloud and sweeped in frequency. If the laser frequency fulfils the resonance condition, some pairs of atoms will be excited to a bound molecular state. This molecules might then decay into the continuum of motional states, generally resulting in a loss of the atoms due to a high kinetic energy. Another decay channel is given by the formation of ground state molecules, which can not be detected by absorption imaging and are thus also seen as a loss. This atom loss is dependent on the intensity I and frequency ν of the laser as well as the density ρ of the atomic cloud, since a higher density results in more atom pairs being in the correct atomic distance to form a molecule. The loss can be described by the differential equation

$$\dot{\rho} = -K(\nu, T, I) \cdot \rho^2, \tag{5.8}$$

where $K(\nu, T, I)$ is the photoassociative loss coefficient. The magnitude can be calculated with the Franck-Condon density between the scattering wave function of the ground state and the molecular wave function of the excited state. This calculation was done by [Ciu04] for the intercombination transition examined in this thesis.
The challenge of photoassociation spectroscopy near the intercombination line compared to photoassociation near strong singlet-singlet transitions lies in the weak transition strength. To achieve well detectable losses, high densities and low temperatures are necessary. In addition the natural linewidth is very small and at low temperatures like 1 μK the expected Doppler and thermally induced full width at half maximum (FWHM) is about 50 kHz (see section 5.3.3), so we have to scan in small steps. We decided to vary the frequency of the spectroscopy laser by 10 kHz from shot to shot. The binding energies of the weakest bound states were previously unknown. According to quantization formulae as discussed in section 5.4 the weakest bound states are supposed to be up to 1.1 GHz away from the asymptote. The large range of possible binding energies and the small width of the expected signal

thus demands for more than $100\ 000$ single measurements, each of a few seconds duration.

5.2 Setup for photoassociation on the intercombination line

The dipole trap and the evaporative scheme developed in chapter 4 provide us with high-density ensembles at low temperatures. Similar to the scheme presented in chapter 4 we start with an almost pure single beam trap with a power of 5.7 W (1.6 W) in the horizontal (tilted) dipole trap and a beam radius of 36 μm (77 μm) at the crossing region. By ramping down only the power of the horizontal beam we force the atoms to accumulate in the crossing region and end the ramp with a power of 0.6 W and 1.6 W in the horizontal and tilted trap, respectively. The trap depth is about $k_B \cdot 8$ μK and the atoms have a temperature of 1 μK. The peak density reaches up to $2.6 \cdot 10^{13}$ cm^{-3} at atom numbers of $200\ 000$. According to the temperature we expect a linewidth of around 53 kHz (FWHM) due to the convolution of Doppler and thermal broadening.
To resolve details of the molecular spectrum we require a laser with a linewidth much smaller than the typical broadening effects. In addition we want to know the exact laser frequency or rather the exact energy distance of the bound levels from the diatomic asymptote. Since we already use an ultranarrow cavity-stabilized diode laser for our second MOT stage as well as for atomic spectroscopy, we chose to use a second diode laser, whose frequency is stabilized to the first one by a beat lock. The beat lock setup is displayed schematically in figure 5.3. Note that the frequency of "Master II" does not correspond to the atomic resonance, but the light is tuned into resonance by a series of AOMs as shown in figure 2.4. Thence the photoassociation light after the slave laser is resonant with the atomic transition, if "Master I" is red detuned of "Master II" by around 621 MHz, and the beat frequency is mixed down by a synthesizer frequency of around 596 MHz. A phase-frequency comparator stabilizes the mixed down frequency to a stable 25 MHz reference[1]. The exact distance to the atomic resonance will be determined by a reference measurement of the atomic transition at the same day as the photoassociation measurement.
With "Master II" having a linewidth of around 1 Hz [Naz06] and the beat lock losing the phase very seldom (probably a few times a day), the laser "Master I" should also be stable to around 1 Hz. Monitoring the mixed-down beat signal with a spectrum analyser[2], I found the laser to be narrower than 100 Hz. In all cases the linewidth was less than 2 kHz and thus much smaller than the width of the observed molecular lines.
The spectroscopy laser is applied as a single beam with a waist radius of 44 μm. Since it can not be assured, that the atomic ensemble is positioned exactly inside the focus, for the calculation of the intensity I assume the beam radius to be (50 ± 6) μm.

[1] The reference is given by an H-Maser stabilized to the caesium atomic fountain clock of PTB.
[2] Anritsu MS2601B

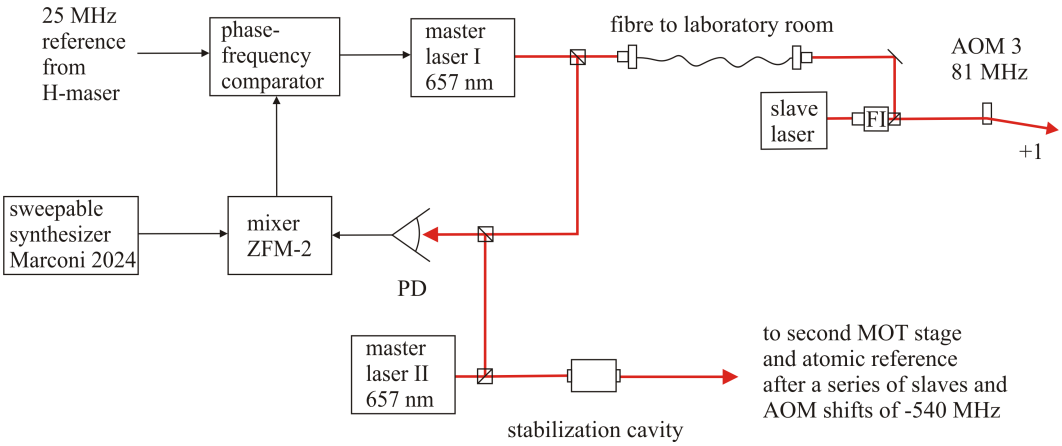

Figure 5.3: Schematic drawing of the beat lock setup between our two master lasers. "Master I" is generating the light for photoassociation spectroscopy. It is beat locked to "Master II", which is the same as in figure 2.4. The 540 MHz of AOM shifts are not constant, but include the cavity drift compensation. The scan is performed by setting a different value to the synthesizer frequency from shot to shot. The deflecting AOM 3 can be used to alter the photoassociation laser power. FI = Faraday isolator, PD = photo diode.

The intensity of the light can be altered by changing the RF-power applied to a deflecting acousto-optic modulator (AOM 3 in figure 5.3).

5.3 Results of the photoassociation measurements

The scan was done in the absence of a magnetic field to maximize the losses at the molecular resonances. After having found the resonances, we investigated them with a magnetic field of about 0.28 mT applied. The frequencies in the following text refer to the position of the $m = 0$ component.
We found photoassociative resonances at synthesizer frequencies of 905.402 MHz and 1579.716 MHz. At the same day the atomic resonance was measured at a synthesizer frequency of 596.676 MHz. This results in one resonance about 309 MHz and the other one 983 MHz below the atomic resonance.
However, the frequencies were measured inside the dipole trap and with finite temperature and thus include several shifts, that will be discussed later. The first step will be the assignment of the measured resonances to the molecular potentials 0_u^+ and 1_u.

5.3.1 Magnetic splitting and identification of the molecular state

The magnetic splitting of a particle´s energy is characterized by the g-factor. While an approximation for g_J^{atom} with the common Landé formula

$$g_J^{atom} = 1 + \frac{J(J+1) + S(S+1) - L(L+1)}{2J(J+1)} \tag{5.9}$$

yields $g_J^{atom}(^3P_1) = 1.5$, a measurement for the calcium $^3P_1$ state results in $g_J^{atom}(^3P_1) = 1.5010829(28)$ [Bev98]. This value is also expected for Hund´s coupling case (e) for non-rotating molecules.
Similar formulae also exist for other coupling cases. Herzberg [Her50] deduced the g-factor for Hund´s coupling case (a) to be

$$g^{(a)} = \frac{|\Lambda + 2\Sigma| \cdot |\Lambda + \Sigma|}{J(J+1)}, \tag{5.10}$$

which results in $g^{(a)}(^3\Sigma_{1_u}) = 1$ and $g^{(a)}(^3\Pi_{0_u^+}) = 0$ for $J = 1$. Using a similar approach as [Her50] we can calculate the g-factor for Hund´s coupling case (c) to be

$$g^{(c)} = g_J^{atom} \frac{\Omega^2}{\sqrt{J(J+1)}\sqrt{J_a(J_a+1)}} \tag{5.11}$$

which results in $g^{(c)}(1_u) = 0.75$ and $g^{(c)}(0_u^+) = 0$ for $J = J_a = 1$.
To measure the magnetic splitting, the molecular resonance was scanned with a magnetic field applied. The field is generated by a current of 5.7 A sent through a pair of Helmholtz coils with four windings each [Naz07], wrapped around the MOT coils. The magnetic field was calibrated by measuring the splitting of the atomic resonance. The atomic resonance showed a splitting of $5.849(11)$ MHz, corresponding to a magnetic field of $2.784(5) \cdot 10^{-4}$ T. The uncertainty results from the uncertainty of the determination of the line centre and the difference between the $m = 1/m = 0$ splitting and the $m = -1/m = 0$ splitting.[3]
The molecular resonance at 309 MHz shows a splitting of $1.075(4)$ MHz, corresponding to a g-factor of $g = 0.276(1)$. The resonance can be attributed to the $c0_u^+$ potential. The molecular resonance at 983 MHz shows a splitting of $4.184(12)$ MHz, corresponding to a g-factor of $g = 1.074(4)$. The resonance can be attributed to the $a1_u$ potential. The splitting is larger than predicted for Hund´s coupling case (c). The g-factor of the resonance at 983 MHz is close to that of Hund´s case (a). The criterion for Hund´s case (a) is a binding energy larger than the atomic spin-orbit coupling constant $A \approx h \cdot 1.5$ THz, which is clearly not given in our experiment. The measured g-factors thus indicate the coupling of the angular momenta being in an intermediate regime between Hund´s cases (c) and (e)[4]. The clear difference in the splitting of the atomic and molecular levels is displayed in figure 5.4.

[3]The difference in the splitting has not been measured on that day, but on a later day with a slightly larger magnetic field. It has been 20 kHz.

[4]This assumption has been confirmed later by my colleague Max Kahmann, who measured g-factors closer to the prediction for Hund´s case (c) for deeper bound molecular levels.

Several weeks later the measurement was repeated for the 0_u^+ resonance. The magnetic splitting of the atomic resonance was $6.13(1)$ MHz, corresponding to a magnetic field of $2.919(5) \cdot 10^{-4}$ T and thus 4.8 % larger than in the previous measurement. This reveals a significant drift in the magnetic field, even if the current is not manually altered. The resulting g-factor of the 0_u^+ resonance was determined to be $g = 0.276(1)$ and thus consistent with the previous measurement within its uncertainties. The consistency of the results proves, that the magnetic field drifts over weeks, but is stable over a day. The drift thus does not distort the measurement as long as the calibration is done on the same day.

5.3.2 Exact position of the photoassociation resonances

The atomic and photoassociation resonances were observed at the synthesizer frequencies mentioned in the beginning of this section. While the position of the loss peak can be determined with an uncertainty of about 2 kHz, it does not represent the actual binding energy of the molecular state; in fact several effects influence the measured frequencies. In the following I will present and quantify the shifts of the atomic as well as the molecular resonance.

Influence of the differential light shift of the dipole trap

While I described the dipole trap wavelength in section 3.1.4 as being approximately magic, this is only true for the $m_J = -1$ component in a single beam dipole trap of σ^+-polarized light. The light shift of the atomic ground state and excited state is generally different in the used crossed beam. In addition the light shift of molecules is not necessarily the same as for atoms due to the different coupling strengths to other states. The differential light shift of the photoassociative transition is thus generally non-zero and will be determined via a measurement.
Due to the necessary long exposure times, it is not possible to observe the molecular resonance in the absence of the trapping beam, i.e. during free fall of the ensemble. To determine and account for the dipole trap light shift I measured the atomic as well as the molecular resonances in a dipole trap with a power of 0.6 W/1.6 W in the horizontal/tilted beam and repeated the measurement for trap powers of 0.3 W/0.8 W. From the different resonance frequencies, the resonance frequencies in absence of the dipole trap light shift can be extrapolated linearly.
I determined the resonance of the atomic $m = 0$ resonance to be shifted by (122 ± 2) kHz towards higher photon energies inside the trap of 0.6 W/1.6 W, whereas the molecular $c0_u^+$ state at 309 MHz and the $a1_u$ state at 983 MHz show shifts of (80 ± 3.6) kHz and (82 ± 2.4) kHz, respectively. This value however is not the light shift alone, but includes another effect, that will be discussed in the following.

Thermal shift

The motion of a pair of atoms can be divided into a centre of mass motion and a relative motion. The relative motion represents a kinetic energy, which contributes

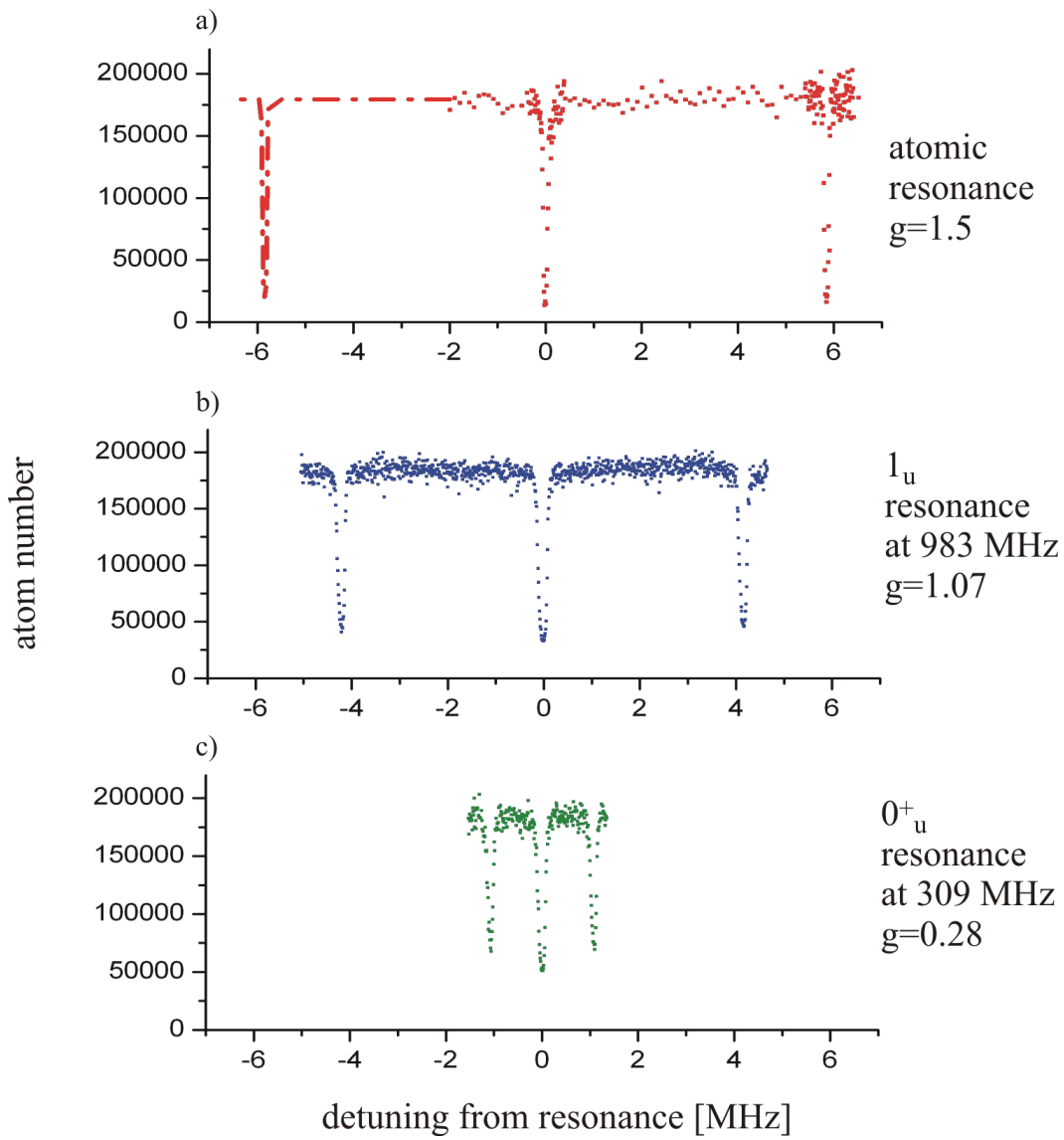

Figure 5.4: Splitting of the atomic and molecular resonances in the presence of a magnetic field of $B = 2.784(5) \cdot 10^{-4}$ T. a) The atomic resonance shows a splitting of $5.849(11)$ MHz, which has been used for the calibration of the magnetic field. The $m = -1$ component was extrapolated. A measurement on a later day showed the absolute value of the shift of the $m = 1$ and $m = -1$ to differ by about 20 kHz. b) The magnetic splitting of the weakest bound molecular state in the $a1_u$ potential 983 MHz below the atomic asymptote shows a significantly smaller splitting than the atomic line. The g-factor is $g = 1.074(4)$. c) The weakest bound state of the $c0_u^+$ potential at 309 MHz below the asymptote features a g-factor of $g = 0.276(1)$. The splittings are larger than predicted for Hund´s case (c) by equation (5.11) and indicate an intermediate regime between Hund´s cases (c) and (e).

to the excitation of the molecule. The resonance condition neglecting all other shifts is thus

$$E_e = \hbar\omega + \epsilon_r(\vec{v}_r) \tag{5.12}$$

with E_e the energy of the excited molecular state relative to the ground state diatomic asymptote, $\hbar\omega$ the photon energy and $\vec{v}_r$ and $\epsilon_r = \frac{1}{2}\mu\vec{v}_r^2$ the relative velocity between the atoms and the corresponding kinetic energy, respectively. Although the relative motion features velocity components in all three dimensions, all atom pairs with a notable relative motion perpendicular to the internuclear axis are precluded from forming a molecule for geometric reasons. The thermal velocity relevant for the formation of a molecule thus follows the one dimensional Maxwell-Boltzmann distribution along the internuclear axis

$$f(v_r) \propto exp(-\frac{\mu v_r^2}{2k_BT}). \tag{5.13}$$

In quadratic average the atom pairs carry a relative velocity of

$$\sigma_{v_r} = \sqrt{2}\sqrt{\frac{3k_BT}{m_{Ca}}}. \tag{5.14}$$

Even though the energy distribution of the atom pairs is an exponential, the line shape will be a bit different. The collision of an atom pair with high relative velocity will happen much faster than of an atom pair with low relative velocity. Thus more collisions will happen at faster velocities, resulting in an additional factor proportional to $\sqrt{\epsilon_r}$. The energy distribution among all collisions thus follows

$$f(\epsilon_r) \propto \sqrt{\epsilon_r}\, exp(-\frac{\epsilon_r}{k_BT}). \tag{5.15}$$

This leads to a shift of the resonance of

$$\overline{\epsilon_r} = \frac{\int_0^\infty \epsilon \cdot f(\epsilon_r)\mathrm{d}\epsilon_r}{\int_0^\infty f(\epsilon_r)\mathrm{d}\epsilon_r} = \frac{3}{2}k_BT = h \cdot 31 \text{ kHz} \tag{5.16}$$

at a temperature of $T = 1\ \mu$K.
For the determination of the light shift, as presented above, I measured the resonance frequency at trap powers of 0.6 W/1.6 W and 0.3 W/0.8 W and extrapolated linearly to the absence of a trapping beam. When lowering the power and thus the trap depth by a factor of 2, one can assume the temperature to be reduced by a factor of 2 as well. The method of extrapolating to the absence of a trapping beam thus represents also an extrapolation to a temperature of $T = 0$. I assume this to be true within a temperature uncertainty of around 10 %, which leads to an additional 3.1 kHz uncertainty for the resonance frequency.
The kinetic energy of the atom pair leads to the resonance being shifted towards lower photon energies. Considering this shift effect, the effect of the light shift alone can be approximated to $111(5)$ kHz and $113(4)$ kHz for the molecular $c0_u^+$ state at 309 MHz and the $a1_u$ state at 983 MHz, respectively, and thus quite similar to the light shift of the atomic resonance.

Influence of the photoassociation laser

The peak intensities of the dipole trap lasers are about $4.3 \cdot 10^8$ W/m^2 and lead to the abovementioned differential light shift in the order of 100 kHz. The intensity of the photoassociation laser has been $5.8 \cdot 10^5$ W/m^2 or less and thus much lower. However, the photoassociation laser frequency is not far-detuned from the atomic resonance in contrast to the dipole trap laser frequency. The photoassociation laser can thus induce a significant differential light shift to the resonance. This light shift has been investigated by scanning over the molecular resonance with different probe beam intensities. The photoassociation laser power was varied between 230 nW and 2.3 mW, which corresponds to an intensity of 60 W/m^2 and $5.8 \cdot 10^5$ W/m^2, respectively. Depending on the fit routine for the determination of the center peak of the losses I determined the differential light shift to be between $55 \cdot 10^{-3}$ Hz/(W m^{-2}) and $85 \cdot 10^{-3}$ Hz/(W m^{-2}) for the 0_u^+ resonance, which can result in a shift of about 50 kHz for the high intensities. The determination of the exact position of the resonance was done at low laser intensities, so that this light shift could be neglected. However, from the observed scattering of points I assume an additional statistic uncertainty of 2.7 kHz and 1.9 kHz for the $c0_u^+$ and the $a1_u$ resonance, respectively.

Photon recoil shift

The photon used for the excitation carries a momentum of $\hbar k$. During the excitation the atom or atom pair has to absorb this momentum, resulting in a kinetic energy of $\frac{\hbar^2 k^2}{2M}$, where M represents the atomic mass in the case of an absorbing atom, and twice the atomic mass in the case of an absorbing atom pair and formation of a molecule. This kinetic energy has to be provided by the photon energy in addition to the electronic excitation energy. Since the recoil energy is $h \cdot 11.6$ kHz at the atomic and only $h \cdot 5.8$ kHz at the molecular resonance, this difference has to be taken into account.
Considering all of the above effects I calculated the molecular resonance of the 0_u^+ and 1_u state to be $(308\ 670 \pm 5.7)$ kHz and $(982\ 994 \pm 4.6)$ kHz below the atomic asymptote, respectively.

5.3.3 Broadening effects of the PA resonances

While the exact binding energies of the weakest bound molecular states have been determined in the previous section, another interesting topic is the strength, width and shape of the resonances. The natural linewidth of a molecule close to an atomic asymptote is twice as large as the linewidth of the corresponding atomic transition (as described by Dicke [Dic54]). The natural linewidth is the dominant effect at most photoassociation experiments involving singlet-singlet transitions at temperatures lower than a few millikelvin. The situation is different for the narrow intercombination transition of calcium. The natural linewidth of $^1S_0 + {}^3P_1$ molecules is about 750 Hz and thus much smaller than the Doppler width even at temperatures of $1\ \mu$K, which is about 36.5 kHz (FWHM). This and other broadening mechanisms will be

described in this section.

Broadening due to decreasing density

The photoassociation resonances result in a reduced atom number over a certain frequency range, shaped as some kind of peak function. The loss depends on the density of the atomic cloud, since photoassociation is a two body loss process. For low losses the number of lost atoms scales linearly with the time over which the photoassociation laser is applied. For larger losses however there will be a saturation effect due to a decreasing density over time. This effect leads to a broadening of the observed resonance. In fact the depth and width of the drop in atom number is not the physical parameter of relevance. Instead the loss parameter $K(\nu, T, I)$ defined by the loss equation

$$\dot{\rho} = -K(\nu, T, I) \cdot \rho^2 \tag{5.17}$$

is used. Since the observable is the atom number, eq. (5.17) can be expressed as

$$\dot{N} = -\beta(\nu, T, I) \cdot N^2. \tag{5.18}$$

The relation between $\beta(\nu, T, I)$ and $K(\nu, T, I)$ is given by averaging the density in eq. (5.17). The density profile is calculated from the trap parameters as described in section 3.2. We obtain the relation

$$K = \frac{\beta}{(\frac{m\omega_m^2}{2\pi k_B T})^{3/2}/\sqrt{8}}, \tag{5.19}$$

where $\omega_m = (\omega_1 \cdot \omega_2 \cdot \omega_3)^{1/3}$ is the mean trap frequency. Solving the differential equation (5.18) leads to the fit function

$$N(t) = \frac{N_0}{1 + t \cdot \beta(\nu, T, I) \cdot N_0}, \tag{5.20}$$

with t the time over which the photoassociation laser is applied and N_0 the atom number at $t = 0$. This equation is only exact in the absence of other losses like background scattering, evaporation and three-body losses, but can be still used, when these losses are small compared to the total atom number. This case is given in our experiment, where three-body and background losses are in the order of $10\,\%$ of the total atom number at a photoassociation time of half a second. We replaced N_0 by the atom number after the photoassociation time in the absence of photoassociative losses.
All following broadening mechanisms are affecting the width of the loss coefficient K.

Natural linewidth and coupling to other molecular states

The natural linewidth of a molecular state close to the asymptote of one exited and one ground state atom is twice the linewidth of the excited atomic state due to the

formation of a superradiant state [Dic54]. This is valid for the unperturbed molecular states. However a molecular state can couple to other molecular states and thus gain a broader linewidth. Allard et al. [All05] observed a coupling between $c^3\Pi_u$ and $A^1\Sigma_u^+$ states (cf. figure 5.2). However this broadening mechanism could not be resolved in the course of this work. The line shape of the natural linewidth is a Lorentzian profile.

Collisional broadening

Another relevant time scale in the atomic ensemble is the collision rate. In ultracold bosonic ensembles s-wave scattering is the dominant collision process. The scattering cross section

$$\sigma_{s-wave} = \frac{8\pi a_{sc}^2}{1 + a_{sc}^2 k^2} \tag{5.21}$$

is not given by the physical size of the particles, but by their scattering length a_{sc} and their relative momentum $\hbar k$. For elastic collisions between two ground state atoms with a scattering length of $a_{sc} = 500\ a_0$, a temperature of $1\ \mu$K and our peak density of $2.6 \cdot 10^{13}$ cm^{-3} the collision time scale is about 0.16 ms. In collisions between ground and excited state atoms, the excited state atom can be deexcited by the collision. This effects a line width, which can be approximated by the inverse of the collision time scale. However, the scattering cross section between ground state atoms and excited molecules and thus the collision time scale is unknown. With extremely high scattering lengths being unlikely, it is not expected that the collisional broadening plays a dominant role over other broadening effects in our experiment.

Differential light shift due to the trapping beam

The trapping beam leads to a differential light shift as described in section 5.3.2. This differential light shift depends on the intensity the atoms experience and thus their position inside the dipole trap. This broadening effect is in the order of $k_B T/U_0$ times the differential shift in the case of atoms, where U_0 is the trap depth.
The width of this broadening mechanism can be approximated by the following considerations. As presented in section 5.3.2 the differential light shift is about 100 kHz although the light shift of the ground state, which represents the trap depth of a pair of atoms in the absence of gravity, is 720 kHz. From this we know the magnitude of the differential light shift at a certain potential energy. In a harmonic trapping potential the potential energy of a pair of atoms follows the Boltzmann distribution of kinetic energy. The full width at half maximum (FWHM) of the energy distribution can be calculated to $2.44\ k_B$T and thus represents a width of 50.8 kHz in the light shift experienced by the atom pairs. The differential light shift between the ground state and the molecular state thus should show a FWHM of $w_{lightshift} = 7$ kHz.

Thermal and Doppler broadening

Atoms see the light detuned depending on their velocity due to the Doppler effect. However to form a molecule at a Doppler detuned frequency both atoms have to move at this velocity. Also the atoms can transform part of their motional energy so that less energy has to be provided by the photon in order to form the molecule. For a quantitative view on these two effects we divide the motion of the pair of atoms into the relative motion and the centre of mass motion.
The centre of mass motion is responsible for the Doppler broadening. The Doppler width is

$$|\vec{k}|\,\sigma_{v,1D}(M) = |\vec{k}| \cdot \sqrt{\frac{k_B T}{M}}, \tag{5.22}$$

where $\sigma_{v,1D}(M)$ is the $1/\sqrt{e}$-width of the Maxwell-Boltzmann velocity distribution in one dimension and $M = 2 \cdot m_{Ca}$ is the mass of the pair of atoms. The Doppler broadening leads to a Gaussian line shape and does not shift the resonance. At a temperature of $1\ \mu$K the FWHM is $w_{Doppler} = 36.5$ kHz.
The relative motion effects a kinetic energy, which contributes to the excitation of the molecule as described in section 5.3.2. The energy distribution follows equation (5.15), leading to a FWHM of $w_{therm} \approx 1.8\ k_B$T $= h \cdot 37$ kHz. The connected shift of the resonance has been examined in section 5.3.2.
The combined width of the abovementioned broadening mechanisms can be approximated by the root of the sum of squares analogous to the law of propagation [Ku66]. It results in a FWHM of 53 kHz at a temperature of $1\ \mu$K in a trap of 0.6 W and 1.6 W in the horizontal and tilted trapping beam, respectively. At half the trap depth and half the temperature we expect a FWHM of 32 kHz.

Power broadening

In a two level system the excitation probability scales linearly with the light intensity for low intensities. As the excitation probability gets higher with higher intensities, the effect of stimulated emission becomes important. The excitation probability in a continuous wave light field thus gets saturated and approaches $1/2$. The excitation probability ρ_e can be calculated to be

$$\rho_e = \frac{1}{2}\frac{s_0}{1 + s_0 + (2\Delta/\gamma)^2} \tag{5.23}$$

with the detuning Δ and the natural linewidth γ in units of Hz. $s_0 = I/I_{sat}$ is the saturation parameter representing the light intensity I in relation to the saturation intensity $I_{sat} = h\ c\ \pi \frac{\gamma}{3\lambda^3}$. Equation (5.23) leads to a power broadened linewidth of $\gamma_{sat} = \gamma \cdot \sqrt{1 + s_0}$ and a Lorentzian line shape.
Power broadening in the case of a transition from atoms to a molecule can generally not be explained by this simple two level system model, since the electronic ground state of free atoms features a continuum of states with distinct relative kinetic energies.

It is reasonable to expect, that light-induced deexitation and dissociation is possible in the case of molecules. The width of the resonance will be investigated with respect to the photoassociation laser intensity. The experimentally observed broadening is displayed in figures 5.6 and 5.7. A quantitative description with a simple two level system model is not possible though.

5.3.4 Measurement of the line shape

The atom loss in dependence on the photoassociation laser frequency has been detected via absorption imaging. The solution of the two-body loss equation as given by equation (5.20) has been fitted to the observed losses. While a fit with a Gaussian shaped loss coefficient $\beta(\nu)$ represents the measurement quite well for scans with low photoassociation laser intensities, at high intensities the observed line features a sharper peak than predicted by a fit with a Gaussian loss coefficient. A Lorentzian shaped loss coefficient, as predicted for power broadened lines, leads to a sharper peak than observed. The observation thus indicated an intermediate line shape between Gaussian and Lorentzian. The convolution of a Gaussian and a Lorentzian line shape results in a Voigt profile. Though a Voigt profile can not be analytically described, there exist approximations. A Voigt profile with the FWHM of w_V can be well approximated by a weighted sum of a Lorentzian and a Gaussian both having the same width w_V [Liu01]. I described the loss coefficient $\beta(\nu)$ by the pseudo-Voigt formula

$$\beta(\nu) = \beta_0 \left(\mu \cdot \frac{1}{1 + \frac{4\cdot(\nu-\nu_0)^2}{w_V^2}} + (1-\mu) \cdot e^{-\frac{4\cdot ln(2)\cdot(\nu-\nu_0)^2}{w_V^2}} \right). \tag{5.24}$$

Figure 5.5 shows a comparison of the fit with a Gaussian, Lorentzian and pseudo-Voigt shaped loss coefficient to a loss curve generated for low and high spectroscopy laser intensities. The weighting factor μ of the Lorentzian and Gaussian fraction of the Voigt profile can principally be used to deduce the line width of the Gaussian and the Lorentzian broadening effect. This deduction can be done by methods given in [Liu01] and [Oli77]. For high laser intensities this would lead to a FWHM of the Gaussian contribution of 136 kHz and 110 kHz for laser intensities of 37 W/cm^2 and 58 W/cm^2, respectively, and thus much larger than the predicted Doppler broadening. However, the fitted weighting factor μ features a large uncertainty and it is thus not possible to achieve accurate quantitative results from the line shape of the loss coefficient $\beta(\nu)$.

Investigation of the line width

The scan over the molecular resonances was repeated for different photoassociation laser intensities. A pseudo-Voigt profile of the loss coefficient as in equation (5.24) was assumed for the loss coefficient $\beta(\nu)$ and equation (5.20) was fitted to the observed atom losses. Apart from the exact energy difference of the molecular levels relative to the diatomic asymptote as discussed in section 5.3.2, we can extract the

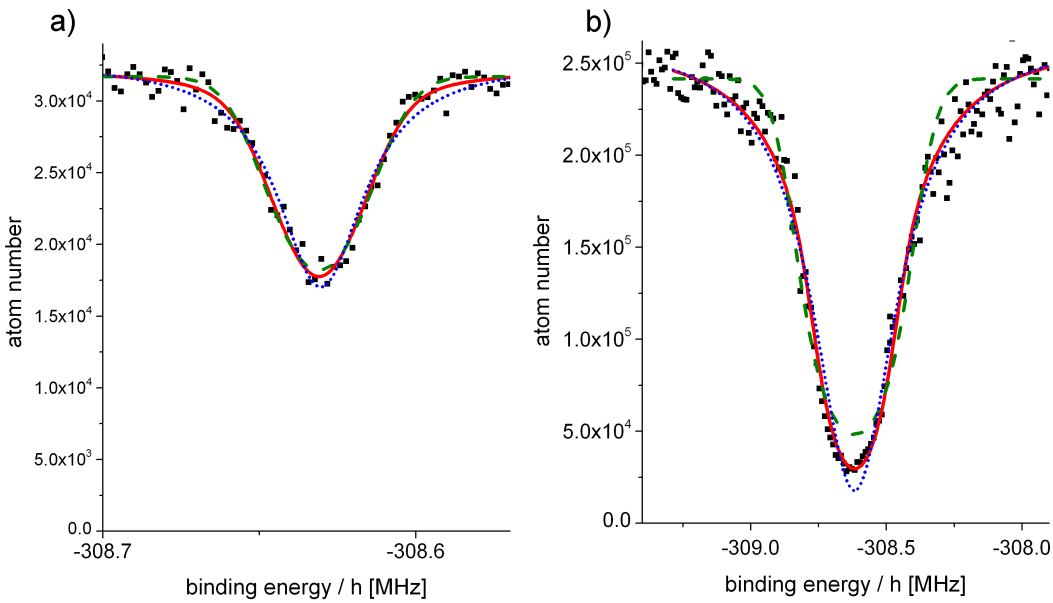

Figure 5.5: Atom number after the application of the photoassociation laser in dependence on the laser frequency. Shown is a scan over the $m = 0$ component of the weakest bound molecular $c0_u^+$ level at different laser intensities. The (red) solid line shows a fit according to equation (5.20) with a pseudo-Voigt distributed loss coefficient $\beta(\nu)$, whereas in the (green) dashed fit the loss coefficient is assumed as a Gaussian and in the (blue) dotted fit as a Lorentzian. a) For low laser intensities as 6 mW/cm^2 the Lorentzian fit is slightly too broad in the wings, but all three fits achieve a reasonable agreement with the data. b) At high laser intensities of 58 W/cm^2 the Gaussian fit underestimates the peak losses, whereas the Lorentzian fit shows a too sharp peak. The good agreement of the pseudo-Voigt fit indicates a convolution of Gaussian and Lorentzian broadening effects.

peak loss coefficient $\beta_0(I,T)$ or $K_0(I,T)$ and the Voigt width w_V. The loss coefficient $K_0(I,T)$ at the $m = 0$ component of the 1_u resonance and its width are displayed in figure 5.6 in dependence on the photoassociation laser intensity. The peak loss coefficient is increasing with the photoassociation laser intensity. A linear fit to the rising slope gives about $1.1 \cdot 10^{-12}$ cm^{3}s^{-1}/(W cm^{-2}). The dipole trap powers were 0.6 W and 1.6 W in the horizontal and tilted beam, respectively. At half the trap power and thus around half the temperature the peak loss coefficient is about four times larger. The FWHM of the loss coefficient is about 57 kHz at low photoassociation laser intensity and increases with the intensity (filled black squares in fig. 5.6). At half the dipole trap power and temperature the width of the loss coefficient was about a factor of 2 smaller for each photoassociation laser intensity (empty red circles in fig. 5.6).
The width of the photoassociation resonance in dependence of the photoassociation laser intensity has been further investigated at the $m = 0$ component of the molecular 0_u^+ resonance at 309 MHz below the diatomic asymptote (figure 5.7). The scan over the resonance was performed with laser intensities of up to 58 W/cm^2. A linear fit to the rising slope of the loss coefficient K_0 results in $2.7 \cdot 10^{-12}$ cm^{3}s^{-1}/(W cm^{-2}), which is larger than predicted by [Ciu04], who calculated the loss coefficient for the sum of all m_J subcomponents. The peak loss coefficient seems to behave linearly to the intensity also for high intensities. However, a linear fit to all data leads to a slope of only $3 \cdot 10^{-13}$ cm^{3}s^{-1}/(W cm^{-2}).
The width of the resonance also increases with the photoassociation laser intensity, but shows a saturation behaviour for high intensities. This saturation behaviour can not be described by the saturation formulas derived from a two-level system model. In addition the linear behaviour of the peak loss coefficient is not consistent with a saturation effect according to the two-level system model.
In conclusion a dependence on the photoassociation laser intensity could be observed revealing a power broadening, which however could not be quantitatively described by a suitable model. The Voigt-width at low intensities was 57 kHz and thus in good agreement with the expected 53 kHz from the combined width of Doppler, light shift and thermal broadening.

5.4 Quantization formulae for near-asymptotic bound states

The prediction of the binding energy of the molecular bound states demands for the exact knowledge of the molecular potential and the numerical solving of the Schrödinger equation. In this part of my thesis I will present theoretical approaches to the quantization of near-asymptotic molecular states. I will then use this quantization formulae to predict deeper bound states on basis of the binding energy of the molecular states described above.

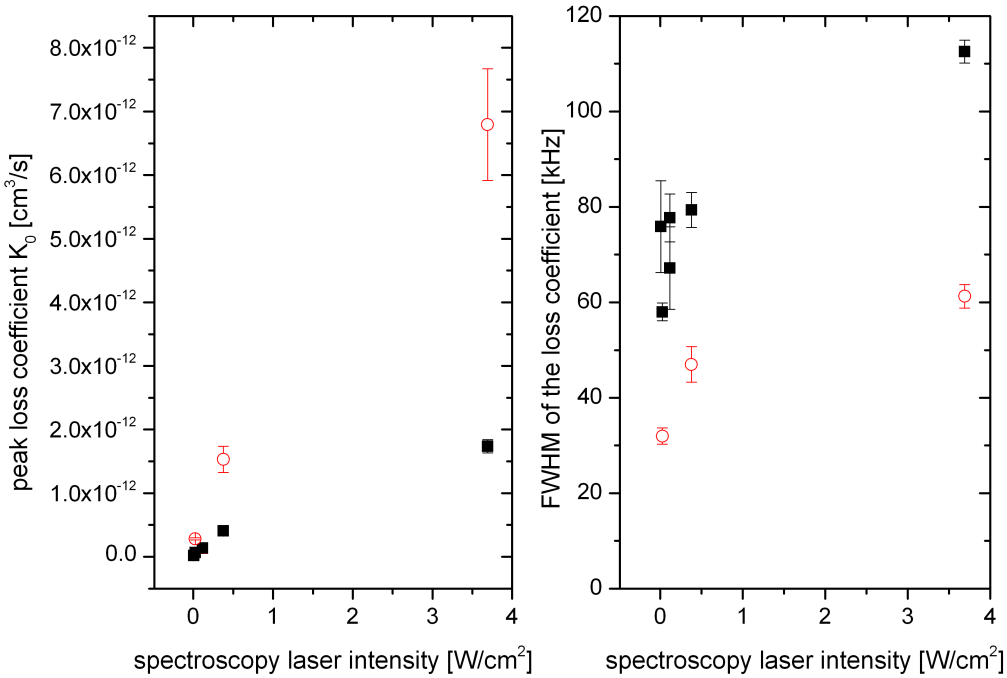

Figure 5.6: Peak loss coefficient K_0 and the FWHM of the loss coefficient at the resonance of the weakest bound 1_u level at a binding energy of 983 MHz in dependence on the spectroscopy laser intensity. The filled black squares represent a measurement at a horizontal and tilted trap power of 0.6 W and 1.6 W, respectively, and a temperature of 1 μK. The empty red circles represent a measurement at a horizontal and tilted trap power of 0.3 W and 0.8 W, respectively. K_0 and the Voigt width of the loss coefficient K increases for higher spectroscopy laser intensities. At half the trap power and temperature K_0 is around four times larger and the width is a factor of about 1.8 smaller for every spectroscopy laser intensity.

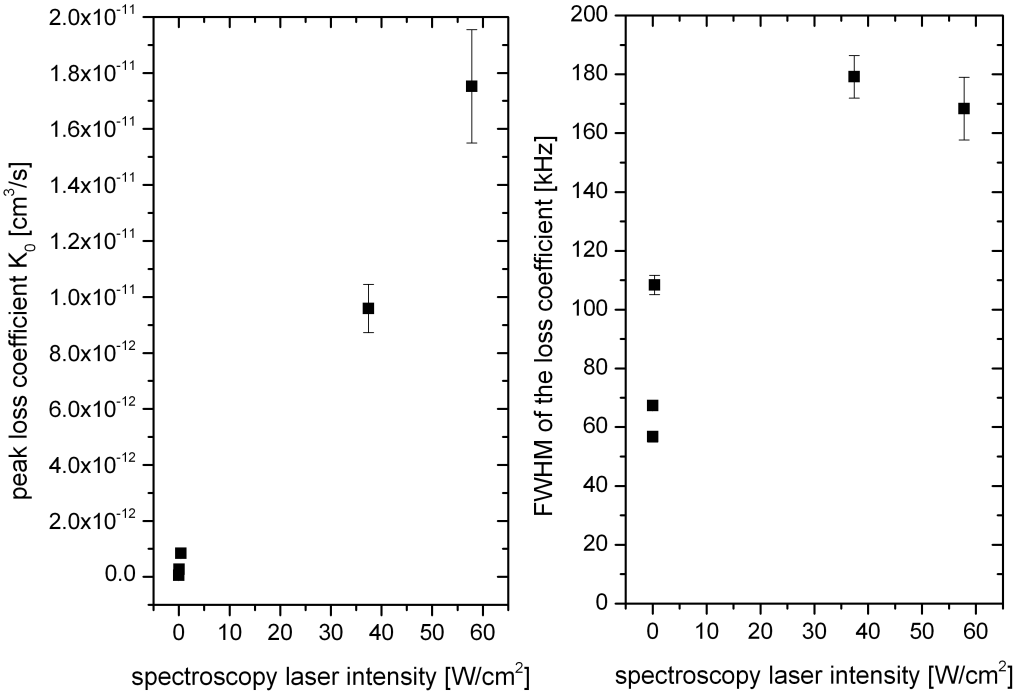

Figure 5.7: Peak loss coefficient K_0 and the FWHM of the loss coefficient at the resonance of the weakest bound 0_u^+ level at a binding energy of 309 MHz in dependence on the spectroscopy laser intensity. The applied spectroscopy laser intensity was up to 15-fold higher than in figure 5.6. The width shows a dependence on the spectroscopy laser intensity, which indicates saturation effects. The data can not be reproduced by the model of saturation in two-level systems though. Also the linear behaviour of the peak loss coefficient K_0 contradicts a classical description of saturation.

5.4.1 WKB method

A simple method of solving the Schrödinger equation for arbitrary potentials and also to deduce a quantization rule for the possible energy levels in a potential was developed independently by Wentzel [Wen26], Kramers [Kra26] and Brillouin [Bri26]. It is based on the assumption, that the kinetic energy $E_{kin}(r) = E_{tot} - V(r)$ is connected to a local momentum $p(r) = \sqrt{2\mu E_{kin}(r)}$ and thus a wavelength $\lambda(r) = h/p(r)$. The total phase accumulated during half an oscillation in the potential can be calculated by

$$\frac{\Phi_{tot}}{2\pi} = \frac{\sqrt{2\mu}}{h} \int_{R_1}^{R_2} \sqrt{E_{tot} - V(r)} dR \tag{5.25}$$

with R_1 and R_2 the classical turning points. They approximated the potential linearly at the reflection points, leading to a reflection phase of $\pi/4$. For a stationary solution the accumulated phase has to be $n \cdot \pi$, which leads to the quantization condition

$$v + 1/2 = \frac{\Phi_{tot}}{\pi}, \tag{5.26}$$

where v is the index of the vibrational level, starting to count from 0.

5.4.2 Le Roy-Bernstein formalism for level spacing near the dissociation limit

While the WKB method requires the full knowledge of the potential and the solution of equation (5.25), Le Roy and Bernstein developed a near-asymptotic quantization formula based on WKB wavefunctions [Le 70]. The method is based on handling the quantum number v as a continuous variable and differentiating the quantization condition given by equations (5.25) and (5.26). For a potential which is basically given by one potential coefficient C_n in the form

$$V \approx D - C_n/R^n \tag{5.27}$$

for large interatomic distances R, they found the rather simple quantization condition

$$E(v) = D - (H_n \cdot (v_D - v))^{\frac{2n}{n-2}} \tag{5.28}$$

for near-asymptotic states for which the largest fraction of the probability density lies in the C_n-dominated region. In this quantization formula

$$H_n(C_n) = \frac{n-2}{2n} \frac{2\pi\hbar^2}{\mu} \frac{\Gamma(1+1/n)}{\Gamma(1/2+1/n)} \frac{n}{C_n^{1/n}} \tag{5.29}$$

is a collection of constants and v_D is the fractional quantum number, which is assigned to the asymptote. v and v_D can not be derived from the near asymptotic potential alone, but depend on the accumulated phase in the inner region. The difference $v_D - v$ however has to be between 0 and 1 for the weakest bound state and

increases by 1 for every deeper bound state. It can thus be considered as a quantization number counting from the high energetic levels downwards instead of from the vibrational ground state upwards. The quantization formula for the last four bound states is plotted in figure 5.8.
The quantization formula of Le Roy and Bernstein is a good approximation for a potential according to the assumption of equation (5.27). Its predictions however become inaccurate for potential tails with more than one relevant C_n coefficient. It also neglects rotational energies of the molecular states and retardation effects, which become relevant for very long range molecules. The molecular potentials investigated in this thesis are mainly dominated by the C_6 coefficient, however the C_8 term should not be neglected for molecular levels deeper bound than the first one. In addition the investigated molecules do have a rotational energy.

Rotational effects in Le Roy-Bernstein formalism

The Le Roy-Bernstein formalism has been successively improved and expanded. The first improvement was an expansion from rotationless to rotating molecules [Le 72]. The calculation of the rotational energy is simple in principle. It is given by $\hbar^2 \cdot \vec{R}^2$ divided by $2\mu R^2$ for a classical particle, where $\vec{R}$ is the angular momentum vector of the nuclear rotation and R is the nuclear separation. For a quantum particle the $1/R^2$ term has to be replaced by the expectation value

$$\left\langle \frac{1}{R^2} \right\rangle = \int \Psi^* \frac{1}{R^2} \Psi \, dR. \tag{5.30}$$

The evaluation of equation (5.30) however would require the precise vibrational wavefunction Ψ. Here again Le Roy uses WKB wavefunctions and the assumption of a potential tail dominated by one C_n term. The total energy of a molecular state with rotational component is then quantized by the formula

$$E(v) = D - (H_n(v_D - v))^{\frac{2n}{n-2}} + B_v \langle \vec{R}^2 \rangle \tag{5.31}$$

where $B_v = Q_n \cdot (v_D - v)^{4/(n-2)}$. Here $Q_n(C_n)$ is like H_n a collection of constants, which will not be given here explicitly.
In a later publication [Le 80a] Le Roy developed the rotational quantization formula further to include higher order effects like centrifugal distortion of the potential to a quantization formula of

$$E(v) = D - (H_n \cdot (v_D - v))^{\frac{2n}{n-2}} + B_v \langle \vec{R}^2 \rangle - D_v \langle \vec{R}^2 \rangle^2 + H_v \langle \vec{R}^2 \rangle^3 + L_v \langle \vec{R}^2 \rangle^4 \tag{5.32}$$

with D_v, H_v and L_v again being collections of constants and a power of $v_D - v$ lower by 2 for each higher order coefficient. Though the corrections due to the higher order rotational terms are only a few MHz and thus smaller than many other uncertainties, they will be included in my calculations for completeness.

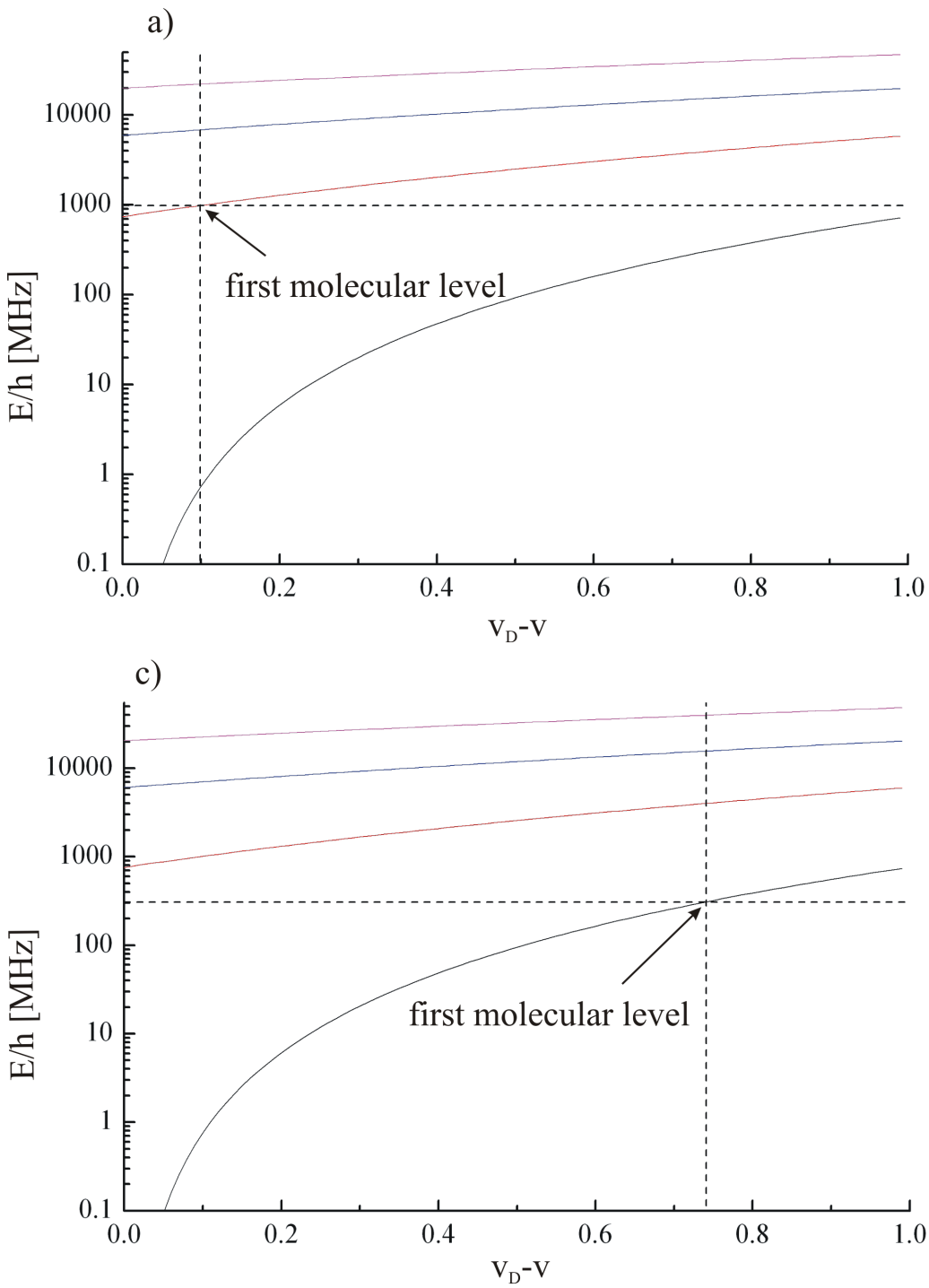

Figure 5.8: Energy of the last four bound states in dependence on the fractional quantum number $v_D - v$ of the weakest bound level according to Le Roy-Bernstein quantization condition [Le 70] in the molecular potentials a) 1_u and c) 0_u^+. According to this formalism the first bound state was expected within 740 MHz and 760 MHz below the asymptote, respectively. The discrepancy of the experimentally found first level at 983 MHz will be resolved later. Note that this quantization condition neglects rotational effects and higher power potential coefficients.

Influence of higher C_n coefficients on the quantization rule

The formalism as mentioned above is deduced from WKB wavefunctions with a potential tail consisting of only one term. In 1980 Le Roy published a modification including the influence of the next than leading term [Le 80b]. However he found the integral for the calculation of the rotational splitting to be unsolvable for some combinations of leading and next-to-leading powers. Comparat reviewed the method used by Le Roy and introduced solvable integrals for the rotational term as well, in which however one term is dependent on the selection of integration boundaries [Com04]. He suggests to use the term as a fit parameter. Thus it cannot be used for the prediction of the rotational energy of the next molecular states. The method can be used though to predict the vibrational energy of the deeper bound states under consideration of next-to-leading potential powers. For the calculation of the vibrational energies of the deeper bound levels I will use the following relation between $v_D - v$ and $D - E(v)$:

$$\begin{aligned} v_D - v = & \frac{\sqrt{2\mu}}{2\pi\hbar}(-C_n)^{\beta-1/2}\frac{B(\beta,1/2)}{n}\frac{(D-E)^{1-\beta}}{1-\beta} \\ & + \frac{\sqrt{2\mu}}{2\pi\hbar}(-C_n)^{\delta-1/2}\frac{C_m}{C_n}\frac{(D-E)^{1-\delta}}{1-\delta}\frac{B(\delta,1/2)}{n}(\delta-1/2) \end{aligned} \tag{5.33}$$

with $n = 6$, $m = 8$, $\delta = \frac{1}{3}$, $\beta = \frac{2}{3}$ and $B(a,b) = \frac{\Gamma(a)\Gamma(b)}{\Gamma(a+b)}$ the Euler Beta function. This quantization formula is taken from [Com04, eq. (35)] disregarding a term, which depends on the potential curvature at the inner turning point.

5.4.3 Raab-Friedrich formalism

Raab and Friedrich [Raa08] further investigated the quantization condition with respect to the outer reflection phase. The curvature of the potential at the outer turning point can change significantly over one de Broglie wavelength for weakly bound levels. Thus the assumption of a linearly approximated potential in the WKB method is no longer valid. The importance of the outer reflection phase has been pointed out in the late 1990s [Tro97, Boi98]. Raab and Friedrich developed a quantization formula including the influence of the outer reflection phase [Raa08]:

$$n_{th} - n = \frac{2b\kappa - (d\kappa)^2}{2\pi(1+(B\kappa)^4)} + \frac{(B\kappa)^4}{1+(B\kappa)^4}\cdot\left[-\frac{1}{8} + \frac{D}{2\pi(\kappa\beta_6)^{2/3}} + \frac{\Gamma(2/3)(\kappa\beta_6)^{2/3}}{4\sqrt{\pi}\Gamma(7/6)}\right]. \tag{5.34}$$

Here $\kappa = \sqrt{-2\mu E}/\hbar$ is the momentum connected to the negative binding energy E, β_6 can be calculated from C_6, and d, b, B and D are numerical constants or numerical multiples of β_6. n_{th} and n play the role of the quantum numbers v_D and v in the Le Roy-Bernstein formalism.

The prediction of the level spacing of deeper bound states with formula (5.34) leads to similar results as the Le Roy-Bernstein formalism. A significant difference appears in the calculation of the least bound state, where the outer reflection phase plays an important role. The Raab-Friedrich formalism predicts the least bound

state to be within 1030 MHz (1060 MHz) rather than within 740 MHz (760 MHz) below the diatomic resonance for the 1_u (0_u^+) potential. This is in agreement with the fact, that the weakest bound state in the 1_u potential has been found 983 MHz below the atomic resonance (see section 5.3.2).
Including rotational effects and the influence of higher power terms of the potential into the Raab-Friedrich formalism demands for a numerical solution of the reflection phases [Kai11] which is not done in the course of this thesis, since the predictions of the analytical rotational energies given by the improved Le Roy-Bernstein formula are accurate enough to get a good overview of the level spacing.

5.4.4 Prediction of deeper bound states

On the previous pages I presented several quantization rules for the binding energies of near-asymptotic bound states. I have used these quantization rules to predict the binding energy of deeper bound states on the basis of the binding energies found in section 5.3.2. I will compare four different prediction methods:

(1) Rotationless Le Roy-Bernstein formalism in a pure $1/R^6$ potential following [Le 70].

(2) Rotationless Raab-Friedrich formalism in a pure $1/R^6$ potential following [Raa08].

(3) Le Roy-Bernstein formalism with rotational terms in a pure $1/R^6$ potential following [Le 80a].

(4) Vibrational energy with an advanced Le Roy-Bernstein formalism under consideration of the $1/R^6$ and $1/R^8$ term following [Com04, eq. (35)] neglecting the short range term, rotational energy following [Le 80a].

Table 5.2 shows the binding energy of deeper bound levels in the 0_u^+ potential predicted by the methods (1)-(4) along with the binding energies measured by my colleague Max Kahmann. The molecular levels were found following the prediction method (4). The predicted and measured binding energies of molecular states in the 1_u potential are presented in table 5.3. While the vibrational levels are usually denoted by the quantum number v counting up from the deepest bound level ($v = 0$) to the weakest bound level ($v = v_{max}$), I will use the alternative denotion $v' = v_{max} - v$. Thus $v' = 0$ denotes the weakest bound state and v' increases by one for every deeper bound vibrational level.
The comparison of the quantization formulae shows, that the consideration of rotational terms generally leads to the largest corrections for the binding energies of the 0_u^+ states, whereas the binding energy of the 1_u states depends strongly on the influence of the C_8 coefficient. Considering both effects, I was able to predict the binding energies of the deeper bound states with a precision of about $70 - 190$ MHz. The predictions strongly restricted the interval to search for the bound states experimentally. A more precise prediction would have demanded for a lot more effort,

	method (1)	method (2)	method (3)	method (4)	measured
E(v′=0)/h	308.670 MHz				
$v_D - v$ or $n_{th} - n$	0.741	0.633	0.860	0.857	
E(v′=1)/h	4.01 GHz	4.08 GHz	4.51 GHz	4.58 GHz	4.65 GHz
E(v′=2)/h	15.65 GHz	15.86 GHz	17.19 GHz	17.71 GHz	17.86 GHz
E(v′=3)/h	39.78 GHz	40.22 GHz	42.92 GHz	44.75 GHz	

Table 5.2: Binding energies of deeper bound 0_u^+ states ($v' = 0$ to $v' = 3$) as predicted by various quantization formulae. The input to the formulae is the binding energy of the $v' = 0$ state and the van der Waals coefficients given by [Mit08]. The last column shows actual binding energies experimentally determined by Max Kahmann [Kah13]. The third row of the table shows the fractional quantum number of the asymptote, which is a parameter of the quantization formulae.

for example the numerical solution of the Schrödinger equation. The gain in precision however is limited by the uncertainty of the van der Waals coefficients as well. Different theoretical calculations [Ciu04, Mit08] result in C_6 coefficients differing by about 3 %. This uncertainty leads to uncertainties in the predictions of about 60 MHz to 250 MHz for the second and third weakest bound state in the 0_u^+ potential, respectively.
The fractional quantum number $v_D - v_{max}$ assigned to the asymptote in the 1_u potential is larger than 1 for the quantization methods (1), (3) and (4), which are all based on Le Roy-Bernstein formulae. A fractional quantum number of larger than 1 indicates another weakly bound molecular state very close to the asymptote (0.7 MHz to 15.7 MHz, depending on the used quantization method), which has not been found. The non-existence of this bound state can be explained by the consideration of the outer reflection phase of the wavefunction [Tro97, Boi98]. The Raab-Friedrich formalism (method (2)) accounts for the outer reflection phase and is the only quantization formula I used, which does not erroneously predict another bound state.
The existence of a bound state close to the asymptote would involve a large positive scattering length between $^1S_0$ and $^3P_1$ atoms, whereas an unbound state would involve a large negative scattering length. In any case a large scattering cross section is indicated, which might explain the light-assisted losses observed by [Vog09]. These losses occurred in dense ensembles in the dipole trap, if the 657 nm cooling light was switched on. A quantitative evaluation is not possible though, because the exact position of this unbound state can not be predicted with these simple quantization formulae.

5.5 Summary

In this chapter, plenty of results of the photoassociation spectroscopy has been presented, which shall be summarized here shortly. The measurement of the g-factors resulted in $g = 0.276(1)$ and $g = 1.074(4)$. The g-factors were used to assign the found molecular states to the 0_u^+ and 1_u potentials, respectively. With the calculated

	method (1)	method (2)	method (3)	method (4)	measured
E(v′=0)/h	982.994 MHz				
$v_D - v$ or $n_{th} - n$	1.099	0.986	1.140	1.129	
E(v′=1)/h	6.85 GHz	6.91 GHz	7.04 GHz	7.34 GHz	7.41 GHz
E(v′=2)/h	22.04 GHz	22.21 GHz	22.62 GHz	24.35 GHz	24.54 GHz
E(v′=3)/h	51.01 GHz	51.35 GHz	52.15 GHz	57.91 GHz	

Table 5.3: Binding energies of deeper bound 1_u states ($v' = 0$ to $v' = 3$) as predicted by various quantization formulae. The input to the formulae is the binding energy of the $v' = 0$ state and the van der Waals coefficients given by [Mit08]. The last column shows actual binding energies experimentally determined by Max Kahmann [Kah13]. The third row of the table shows the fractional quantum number of the asymptote, which is a parameter of the quantization formulae. While method (4) gives the best agreement with the experimental results, method (2) is the only formula, that explains the non-existence of another bound state very close to the asymptote.

g-factors being larger than predicted for Hund´s coupling case (c), the measurement indicates the states to be in an intermediate regime between Hund´s coupling cases (c) and (e).
Section 5.3.2 presents the binding energy of the molecular states relative to the atomic asymptote. After the correction of several shifts, I determined the binding energies of the weakest bound states to be $h \cdot (308\,670 \pm 5.7)$ kHz and $h \cdot (982\,994 \pm 4.6)$ kHz for the 0_u^+ and 1_u state, respectively.
In section 5.3.3 I discussed several broadening mechanisms and their influence on the width and shape of the photoassociation resonance. I calculated the expected linewidth (FWHM) to be around 53 kHz at a temperature of $1\ \mu$K, where the Gaussian shaped Doppler broadening and the thermal broadening are the most dominant effects. The measurement revealed a linewidth of 57 kHz at low photoassociation laser intensities in good agreement with the expectation. At higher intensities the shape of the loss coefficient $K(\Delta)$ is no longer well described by a Gaussian. A pseudo-Voigt fit shows good agreement with the measured line shape and revealed linewidths of up to 180 kHz for intensities of 58 W/cm^2. The power-broadening can not be described by a simple two-level system model. The rising slope of the peak loss coefficient can be approximated as a linear function of the photoassociation laser intensity and was measured to be $2.7 \cdot 10^{-12}$ cm^{3}s^{-1}/(W cm^{-2}) for the 0_u^+ state and $1.1 \cdot 10^{-12}$ cm^{3}s^{-1}/(W cm^{-2}) for the 1_u state at a temperature of about $1\ \mu$K.
Based on the binding energy of the weakest bound states and the long range van der Waals coefficients of the potentials given by theoretical calculations [Mit08] I calculated the binding energies of deeper bound states using various quantization formulae [Le 70, Le 80a, Com04, Raa08]. The most elaborate quantization formula included rotational effects and the influence of the C_8 coefficient to the vibrational energy. The predictions agreed with the experimental results to about $70 - 190$ MHz, strongly limiting the frequency interval, in which to search for the deeper bound states.

Chapter 6

Conclusion and Outlook

In this thesis two milestones in the physics of ultracold calcium ensembles are presented. With the experimental setup and parameters described here, the first realization of a Bose-Einstein condensate of alkaline earth metals could be achieved [Kra09]. The complex cooling scheme and the inapplicability of magnetic traps made condensation of group II elements very difficult. The trapping of ultracold calcium atoms in a dipole trap [Gra07, Yan07] was an important step towards evaporative cooling to quantum degeneracy. In the course of this thesis, large three-body losses were detected. The three-body loss coefficient was determined to be $(3.2 \pm 1.6) \cdot 10^{-27}$ cm^6/s. An optimized ramping scheme has been developed to reduce these losses. Finally a BEC in a crossed dipole trap as well as in a single-beam dipole trap was realized at a critical temperature of 170 nK and 140 nK, respectively. The atom number of the condensed fraction was about $15\,000$ in the crossed dipole trap, whereas the lower densities in the single-beam dipole trap allow for atom numbers of up to $40\,000$ in the condensed fraction.
A high phase space density, a bimodal distribution and an anisotropic expansion have been observed as clear indicators for a condensate being formed. From the anisotropic expansion of the atoms after release from the crossed dipole trap, we were able to determine the chemical potential of the atoms to be $\mu = k_B \cdot 55$ nK. From that we were able to deduce a ground state scattering length of about $440\ a_0$, confirming earlier values of $a_{sc} = 200\ a_0 - 800\ a_0$ [All03] or $a_{sc} = 340\ a_0 - 700\ a_0$ [Vog07].
The BEC presented in this thesis paved the way for the condensation of the similar alkaline earth element strontium [Ste09, Mar09] and the condensation of calcium with an alternative cooling mechanism, that might also be suited for lighter alkaline earth elements like magnesium [Hal12].
The second milestone of this work is the photoassociation spectroscopy near the ${}^1S_0 - {}^3P_1$ intercombination transition, presented in chapter 5. The weak coupling strength demands for an ultracold dense ensemble, which is provided by the crossed dipole trap after evaporation down to a temperature of $1\ \mu$K. In the two accessible molecular potentials $a1_u$ and $c0_u^+$ the weakest bound state was expected within a binding energy of up to 1.1 GHz and the narrow linewidth demanded for a scan with steps of around 10 kHz. After a total of $100\ 000$ single measurements the

weakest bound state in each potential has been found. Considering several shift mechanisms I calculated the binding energy of the weakest bound $c0_u^+$ state to be $h \cdot (308\,670 \pm 5.7)$ kHz. The weakest bound $a1_u$ state lies $h \cdot (982\,994 \pm 4.6)$ kHz below the atomic asymptote.
I measured the g-factor, which describes the Zeeman splitting in an external magnetic field to be $0.276(1)$ for the $c0_u^+$ state and $1.074(4)$ for the $a1_u$ state. Being higher than the g-factor predicted for Hund's coupling case (c), this indicates an intermediate regime between coupling cases (c) and (e).
An investigation of the width of the photoassociation resonance revealed a line width of 57 kHz at a temperature of 1 μK and thus slightly larger than the expected width of around 53 kHz. The difference can be well explained by uncertainties in the fit and the temperature. Thus the introduction of a phenomenological broadening factor as used in PA studies of rubidium [The04] and strontium [Zel06] is not demanded for.
An increase of the width with higher intensities of the photoassociation laser has been observed. The power broadening can not be described quantitatively by a simple two-level model. The rising slope of the peak loss coefficient can be approximated as a linear function of the photoassociation laser intensity. It is about $2.7 \cdot 10^{-12}$ cm^{3}s^{-1}/(W cm^{-2}) for the $0_u^+, m = 0$ resonance and $1.1 \cdot 10^{-12}$ cm^{3}s^{-1}/(W cm^{-2}) for the $1_u, m = 0$ resonance at a temperature of 1 μK. The coupling strength is thus larger than predicted by [Ciu04], indicating a good applicability for optical Feshbach resonances.
Based on the binding energy of the weakest bound molecular states and the near asymptotic potential shape with van der Waals coefficients from theoretical calculations [Mit08] I predicted the binding energy of deeper bound states using various quantization formulae [Le 70, Le 80a, Com04, Raa08]. The achieved accuracy of the most elaborate prediction method was between 70 MHz and 190 MHz for the four next deeper bound states.
Since only the weakest bound molecular states have been found in the course of my thesis, the next step was the observation of deeper bound states. This has already been done by my colleague Max Kahmann on the basis of my predictions. The binding energies and Zeeman splittings of the states will be used to draw conclusions about the van der Waals coefficients and the coupling behaviour of the angular momenta in the molecules [Kah13]. The achieved uncertainty of a few kHz for the binding energies will allow for the test of quantization formulae and molecular potential models to a previously unachieved precision.
Knowing the line shape and loss coefficients of the photoassociation resonances, these can be used to tune the ground state scattering length by optical Feshbach resonances. Several detection methods for a variation of the scattering length have been developed by other groups. Some of these require a Bose-Einstein condensed gas. From the mean field expansion, the scattering length can be determined as done in chapter 4.4.1. Depending on the application of an optical Feshbach laser and its frequency a different mean field expansion can be observed [Yan13]. Alternatively a standing wave optical Feshbach laser can be used to imply a periodic phase shift to the wavefunction of the condensate due to the spatial variation of the mean field

energy. The periodic phase shift transforms into a separation of the cloud into several momentum components, when the ensemble is released from the trap [Yam10]. For both of these methods a Bose-Einstein condensate is mandatory. A third detection method for the variation of the scattering length has been applied in thermal sodium [Fat00]. It uses an optical Feshbach resonance to tune the scattering length and thus the ground state scattering wave function. A probe laser then detects the losses on another photoassociation resonance, which depend on the Franck-Condon density and thus the scattering wave function.
A detection method, which to my knowledge has not been proposed nor used so far, is the shift of the weakest bound ground state molecular resonance, which is connected to the ground state scattering length. This shift could be detected by a 2-photon spectroscopy using two probe lasers.
Photoassociation spectroscopy and optical Feshbach resonances near the singlet-triplet transition have been of interest since quite a while. Several groups reported on photoassociation and optical Feshbach resonances in cold gases of ytterbium [Toj06, Eno08] and strontium [Zel06, Yan13]. The even narrower intercombination line of calcium will further improve the applicability of optical Feshbach resonances [Ciu05].
The optical Feshbach resonances can then be used to alter the scattering length in a small area inside a BEC, for example to excite solitons or soliton trains. If the photoassociative losses are small enough, one can also use optical Feshbach resonances to optimize the generation and lifetime of a BEC by lowering the scattering length and thus the three-body losses as done by [Web03a] with magnetic Feshbach resonances. Due to a strong overlap between the wavefunctions of excited and ground state molecular states [Ciu04], photoassociation can also be used for the generation of ultracold molecular ensembles in the electronic ground state by spontaneous decay.
The application of two photoassociation lasers will enable to determine the binding energy of the weakest bound state in the molecular potential of two ground state atoms. This would result in a more precise value of the ground state scattering length. Another application of two-photon photoassociation is the generation of molecules by *stimulated Raman adiabatic passage* (STIRAP). While this method is predicted to be unsuited for thermal atomic ensembles [Jav98] it has proven to be very efficient in Bose-Einstein condensates [Mac00].
The achievements presented in this thesis and the acquired experimental and theoretical understanding thus paved the way to novel experiments with alkaline earth atoms in the classical as well as the quantum degenerate regime. These novel experiments especially include the manipulation of the scattering behaviour by low loss optical Feshbach resonances.

Bibliography

[All03] O. Allard, C. Samuelis, A. Pashov, H. Knöckel and E. Tiemann, "Experimental study of the Ca_2 ^1S + ^1S asymptote", Eur. Phys. J. D **26**, 155 (2003).

[All05] O. Allard, St. Falke, A. Pashov, O. Dulieu, H. Knöckel and E. Tiemann, "Study of coupled states for the $(4s^2)^1S + (4s4p)^3P$ asymptote of Ca_2^*", Eur. Phys. J. D **35**, 483 (2005).

[And95] M. H. Anderson, J. R. Ensher, M. R. Mattews, C. E. Wieman and E. A. Cornell, "Observation of Bose–Einstein Condensation in a Dilute Atomic Vapor", Science **269**, 198 (1995).

[And97] M. R. Andrews, C. G. Townsend, H.-J. Miesner, D. S. Durfee, D. M. Kurn and W. Ketterle, "Observation of Interference Between Two Bose Condensates", Science **275**, 637 (1997).

[Ang02] James R. Anglin and Wolfgang Ketterle, "Bose-Einstein condensation of atomic gases", Nature **416**, 211 (2002).

[Bar01] M. D. Barrett, J. A. Sauer and M. S. Chapman, "All-Optical Formation of an Atomic Bose–Einstein Condensate", Phys. Rev. Lett. **87**, 010404 (2001).

[Bec08] Christoph Becker, Simon Stellmer, Parvis Soltan-Panahi, Sören Dörscher, Mathis Baumert, Eva-Maria Richter, Jochen Kronjäger, Kai Bongs and Klaus Sengstock, "Oscillations and interactions of dark and dark-bright solitons in Bose-Einstein condensates", Nature Physics **4**, 496 (2008).

[Bev89] N. Beverini, F. Giammanco, E. Maccioni, F. Strumia and G. Vissani, "Measurement of the calcium $^1P_1$-$^1D_2$ transition rate in a laser-cooled atomic beam", J. Opt. Soc. Am. B **6**, 2188 (1989).

[Bev98] N. Beverini, E. Maccioni and F. Strumia, "g_J Factor of neutral calcium ^3P metastable levels", J. Opt. Soc. Am. B **15**, 2206 (1998).

[Bin01] T. Binnewies, G. Wilpers, U. Sterr, F. Riehle, J. Helmcke, T. E. Mehlstäubler, E. M. Rasel and W. Ertmer, "Doppler cooling and trapping on forbidden transitions", Phys. Rev. Lett. **87**, 123002 (2001).

[Bla01] Eric D. Black, "An Introduction to Pound-Drever-Hall laser frequency stabilization", Am. J. Phys. **69**, 79 (2001).

[Boi98] C. Boisseau, E. Audouard and J. Vigué, "Quantization of the highest levels in a molecular potential", Europhys. Lett. **41**, 349 (1998).

[Bon99] K. Bongs, S. Burger, G. Birkl, K. Sengstock, W. Ertmer, K. Rzążewski, A. Sanpera and M. Lewenstein, "Coherent Evolution of Bouncing Bose-Einstein Condensates", Phys. Rev. Lett. **83**, 3577 (1999).

[Bos24] S.N. Bose, "Plancks Gesetz und Lichtquantenhypothese.", Z. Phys. **26**, 178 (1924) translated by A. Einstein.

[Bra95] C. C. Bradley, C. A. Sackett, J. J. Tollett and R. G. Hulet, "Evidence of Bose-Einstein Condensation in an Atomic Gas with Attractive Interactions", Phys. Rev. Lett. **75**, 1687 (1995) see erratum PRL **79**, 1170 (1997).

[Bri26] Léon Brillouin, "La mécanique ondulatoire de Schrödinger: une méthode générale de resolution par approximations successives", Comptes Rendus de l'Academie des Sciences **183**, 24 (1926).

[Bro24] Louis de Broglie, *Recherches sur la théorie des quanta*, PhD thesis 1924.

[Bro03] John M. Brown and Alan Carrington, *Rotational Spectroscopy of Diatomic Molecules*, (Cambridge University Press, 2003).

[Bur97] E. A. Burt, R. W. Ghrist, C. J. Myatt, M. J. Holland, E. A. Cornell and C. E. Wieman, "Coherence, Correlations, and Collisions: What One Learns about Bose-Einstein Condensates from Their Decay", Phys. Rev. Lett. **79**, 337 (1997).

[Cas89] Y. Castin, H. Wallis and J. Dalibard, "Limit of Doppler cooling", J. Opt. Soc. Am. B **6**, 2046 (1989).

[Chu85] S. Chu, L. Hollberg, J. E. Bjorkholm, A. Cable and A. Ashkin, "Three-Dimensional Viscous Confinement and Cooling of Atoms by Resonance Radiation Pressure", Phys. Rev. Lett. **55**, 48 (1985).

[Chu86] S. Chu, J. E. Bjorkholm, A. Ashkin and A. Cable, "Experimental Observation of Optically Trapped Atoms", Phys. Rev. Lett. **57**, 314 (1986).

[Ciu04] R. Ciuryło, E. Tiesinga, S. Kotochigova and P. S. Julienne, "Photoassociation spectroscopy of cold alkaline-earth-metal atoms near the intercombination line", Phys. Rev. A **70**, 062710 (2004).

[Ciu05] R. Ciuryło, E. Tiesinga and P. S. Julienne, "Optical tuning of the scattering length of cold alkaline-earth-metal atoms", Phys. Rev. A **71**, 030701 (2005).

[Com04] Daniel Comparat, "Improved LeRoy–Bernstein near-dissociation expansion formula, and prospect for photoassociation spectroscopy", J. Chem. Phys. **120**, 1318 (2004).

[Dav95] Kendall B. Davis, Marc-Oliver Mewes, Michael R. Andrews, N. J. van Druten, D. S. Durfee, D. M. Kurn and Wolfgang Ketterle, "Bose–Einstein condensation in a gas of sodium atoms", Phys. Rev. Lett. **75**, 3969 (1995).

[Deg04a] Carsten Degenhardt, *Freie und gespeicherte Calcium-Atome für ein optisches Frequenznormal*, PhD thesis Gottfried Wilhelm Leibniz Universität Hannover (2004) online available at http://www.tib.uni-hannover.de.

[Deg04b] Carsten Degenhardt, Hardo Stoehr, Uwe Sterr, Fritz Riehle and Christian Lisdat, "Wavelength dependent ac-Stark shift of the $^1S_0$-$^3P_1$ transition at 657 nm in Ca", Phys. Rev. A **70**, 023414 (2004).

[Deg05a] C. Degenhardt, T. Nazarova, C. Lisdat, H. Stoehr, U. Sterr and F. Riehle, "Influence of Chirped Excitation Pulses in an Optical Clock with Ultracold Calcium Atoms", IEEE Trans. Instrum. Meas. **54**, 771 (2005).

[Deg05b] Carsten Degenhardt, Hardo Stoehr, Christian Lisdat, Guido Wilpers, Harald Schnatz, Burghard Lipphardt, Tatiana Nazarova, Paul-Eric Pottie, Uwe Sterr, Jürgen Helmcke and Fritz Riehle, "Calcium optical frequency standard with ultracold atoms: Approaching 10^{-15} relative uncertainty", Phys. Rev. A **72**, 062111 (2005).

[Der01] Andrei Derevianko, "Feasibility of Cooling and Trapping Metastable Alkaline-Earth Atoms", Phys. Rev. Lett. **87**, 023002 (2001).

[Der03] A. Derevianko, S.G. Porsev, S. Kotochigova, E. Tiesinga and P.S. Julienne, "Ultracold Collision Properties of Metastable Alkaline-Earth Atoms", Phys. Rev. Lett. **90**, 063002 (2003).

[Dic54] R. H. Dicke, "Coherence in Spontaneous Radiation Processes", Phys. Rev. **93**, 99 (1954).

[Did04] S. A. Diddams, J. C. Bergquist, S. R. Jefferts and C. W. Oates, "Standards of Time and Frequency at the Outset of the 21st Century", Science **306**, 1318 (2004).

[Dre83] R. W. P. Drever, J. L. Hall, F. V. Kowalski, J. Hough, G. M. Ford, A. J. Munley and H. Ward, "Laser Phase and Frequency Stabilization Using an Optical Resonator", Appl. Phys. B **31**, 97 (1983).

[Ein25] A. Einstein, "Quantentheorie des einatomigen idealen Gases. Zweite Abhandlung", Sitzungsberichte der Preussischen Akademie der Wissenschaften **1**, 3 (1925).

[Eno08] K. Enomoto, K. Kasa, M. Kitagawa and Y. Takahashi, "Optical Feshbach Resonance Using the Intercombination Transition", Phys. Rev. Lett. **101**, 203201 (2008).

[Eyl07] E. E. Eyler, D. E. Chieda, M. C. Stowe, M. J. Thorpe, T. R. Schibli and J. Ye, "Prospects for precision measurements of atomic helium using direct frequency comb spectroscopy", Eur. Phys. J. D (2007).

[Fal11] St. Falke, H. Schnatz, J. S. R. Vellore Winfred, Th. Middelmann, St. Vogt, S. Weyers, B. Lipphardt, G. Grosche, F. Riehle, U. Sterr and Ch. Lisdat, "The ^{87}Sr optical frequency standard at PTB", Metrologia **48**, 399 (2011).

[Fat00] F. K. Fatemi, K. M. Jones and P. D. Lett, "Observation of Optically Induced Feshbach Resonances in Collisions of Cold Atoms", Phys. Rev. Lett. **85**, 4462 (2000).

[Fed96a] P. O. Fedichev, Yu. Kagan, G. V. Shlyapnikov and J. T. M. Walraven, "Influence of Nearly Resonant Light on the Scattering Length in Low-Temperature Atomic Gases", Phys. Rev. Lett. **77**, 2913 (1996).

[Fed96b] P. O. Fedichev, M. W. Reynolds and G. V. Shlyapnikov, "Three-Body Recombination of Ultracold Atoms to a Weakly Bound s Level", Phys. Rev. Lett. **77**, 2921 (1996).

[Fer06] G. Ferrari, R. E. Drullinger, N. Poli, F. Sorrentino and G. M. Tino, "Cooling of Sr to high phase-space density by laser and sympathetic cooling in isotopic mixtures", Phys. Rev. A **73**, 023408 (2006).

[For07] T. M. Fortier, N. Ashby, J. C. Bergquist, M. J. Delaney, S. A. Diddams, T. P. Heavner, L. Hollberg, W. M. Itano, S. R. Jefferts, K. Kim, F. Levi, L. Lorini, W. H. Oskay, T. E. Parker, J. Shirley and J. E. Stalnaker, "Precision Atomic Spectroscopy for Improved Limits on Variation of the Fine Structure Constant and Local Position Invariance", Phys. Rev. Lett. **98**, 070801 (2007).

[Fri98] Dale G. Fried, Thomas C. Killian, Lorenz Willmann, David Landhuis, Stephen C. Moss, Daniel Kleppner and Thomas J. Greytak, "Bose-Einstein Condensation of Atomic Hydrogen", Phys. Rev. Lett. **81**, 3811 (1998).

[Gio96] S. Giorgini, L. P. Pitaevskii and S. Stringari, "Condensate fraction and critical temperature of a trapped interacting Bose gas", Phys. Rev. A **54**, R4633 (1996).

[Gra02] S. R. Granade, M. E. Gehm, K. M. O'Hara and J. E. Thomas, "All-Optical Production of a Degenerate Fermi Gas", Phys. Rev. Lett. **88**, 120405 (2002).

[Gra07] Ch. Grain, T. Nazarova, C. Degenhardt, F. Vogt, Ch. Lisdat, E. Tiemann, U. Sterr and F. Riehle, "Feasibility of narrow-line cooling in optical dipole traps", Eur. Phys. J. D **42**, 317 (2007).

[Gre02] Markus Greiner, Olaf Mandel, Tilman Esslinger, Theodor W. Hänsch and Immanuel Bloch, "Quantum phase transition from a superfluid to a Mott insulator in a gas of ultracold atoms", Nature **415**, 39 (2002).

[Gri00] Rudolf Grimm, Matthias Weidemüller and Yurii B. Ovchinnikov, "Optical Dipole Traps for Neutral Atoms", Adv. At. Mol. Opt. Phys. **42**, 95 (2000).

[Gri05] A. Griesmaier, J. Werner, S. Hensler, J. Stuhler and T. Pfau, "Bose-Einstein Condensation of Chromium", Phys. Rev. Lett. **94**, 160401 (2005).

[Gro61] E. P. Gross, "Structure of a Quantized Vortex in Boson Systems", Il Nuovo Cimento **20**, 454 (1961).

[Grü01] J. Grünert and A. Hemmerich, "Optimizing the production of metastable calcium atoms in a magneto-optical trap", Appl. Phys. B **73**, 815 (2001).

[Hal12] Purbasha Halder, Chih-Yun Yang and Andreas Hemmerich, "Alternative route to Bose-Einstein condensation of two-electron atoms", Phys. Rev. A **85**, 031603 (2012).

[Hän75] T. W. Hänsch and A. L. Schawlow, "Cooling of gases by laser radiation", Opt. Commun. **13**, 68 (1975).

[Hän80] T. W. Hänsch and B. Couillaud, "Laser frequency stabilization by polarization spectroscopy of a reflecting reference cavity", Opt. Commun. **35**, 441 (1980).

[Han03] Dirk P. Hansen, Janis R. Mohr and Andreas Hemmerich, "Magnetic trapping of metastable calcium atoms", Phys. Rev. A **67**, 021401 (2003).

[Han06] Dirk Hansen and Andreas Hemmerich, "Observation of Multichannel Collisions of Cold Metastable Calcium Atoms", Phys. Rev. Lett. **96**, 073003 (2006).

[Her50] Gerhard Herzberg, *Molecular Spectra and Molecular Structure: I. Spectra of Diatomic Molecules*, (D. van Nostrand company, Inc., Toronto, New York, London, 1950) 2nd edition.

[Hoy05] C. W. Hoyt, Z. W. Barber, C. W. Oates, T. M. Fortier, S. A. Diddams and L. Hollberg, "Observation and Absolute Frequency Measurements of the $^1S_0$-$^3P_0$ Optical Clock Transition in Neutral Ytterbium", Phys. Rev. Lett. **95**, 083003 (2005).

[Ino98] S. Inouye, M. R. Andrews, J. Stenger, H.-J. Miesner, D. M. Stamper-Kurn and W. Ketterle, "Observation of Feshbach resonances in a Bose-Einstein condensate", Nature **192**, 151 (1998).

[Jav98] Juha Javanainen and Matt Mackie, "Probability of photoassociation from a quasicontinuum approach", Phys. Rev. A **58**, R789 (1998).

[Kah13] Max Kahmann, Eberhard Tiemann, Oliver Appel, Uwe Sterr and Fritz Riehle, "High accuracy photoassociation of ^{40}Ca near the $^3P_1 + {}^1S_0$ asymptote and its Zeeman effect", arXiv:1306.6473 [physics.atom-ph] (2013).

[Kai11] Alexander Kaiser, Tim-Oliver Müller and Harald Friedrich, "Influence of higher-order dispersion coefficients on near-threshold bound and continuum states: Application to $^{88}Sr_2$", J. Chem. Phys. **135**, 214302 (2011).

[Kat99] Hidetoshi Katori, Tetsuya Ido and Makoto Kuwata-Gonokami, "Optimal Design of Dipole Potentials for Efficient Loading of Sr Atoms", J. Phys. Soc. Jap. **68**, 2479 (1999).

[Ket99] W. Ketterle, D.S. Durfee and D.M. Stamper-Kurn, "Making, probing and understanding Bose-Einstein condensates", in *Proceedings Internat. School of Physics "Enrico Fermi"*, Vol.Course CXL, *Bose-Einstein condensation in atomic gases* (IOS Press, Amsterdam, Oxford, Tokyo, Washington DC, 1999) , S. 67–176.

[Köh06] Thorsten Köhler, Krzysztof Góral and Paul S. Julienne, "Production of cold molecules via magnetically tunable Feshbach resonances", Rev. Mod. Phys. **78**, 1311 (2006).

[Kno10] S. Knoop, F. Ferlaino, M. Berninger, M. Mark, H.-C. Nägerl, R. Grimm, J. P. D'Incao and B. D. Esry, "Magnetically Controlled Exchange Process in an Ultracold Atom-Dimer Mixture", Phys. Rev. Lett. **104**, 053201 (2010).

[Kno12a] S. Knoop, LaserLaB, VU University Amsterdam, private communication (2012).

[Kno12b] S. Knoop, J. S. Borbely, W. Vassen and S. J. J. M. F. Kokkelmans, "Universal three-body parameter in ultracold 4He*", Phys. Rev. A **86**, 062705 (2012).

[Kra26] H. A. Kramers, "Wellenmechanik und halbzahlige Quantisierung", Zeitschrift für Physik A Hadrons and Nuclei **39**, 828 (1926) 10.1007/BF01451751.

[Kra09] Sebastian Kraft, Felix Vogt, Oliver Appel, Fritz Riehle and Uwe Sterr, "Bose-Einstein condensation of alkaline earth atoms: ^{40}Ca", Phys. Rev. Lett. **103**, 130401 (2009).

[Ku66] H. H. Ku, "Notes on the Use of Propagation of Error Formulas", JOURNAL OF RESEARCH of the National Bureau of Standards **70C**, 263 (1966).

[Kul12] A. P. Kulosa, J. Friebe, M. P. Riedmann, A. Pape, T. W. Wübbena, D. B. Fim, S. Rühmann, K. H. Zipfel, H. Kelkar, W. Ertmer and E. M. Rasel, "An ultraviolet laser system for laser cooling and trapping of metastable magnesium", arXiv:1201.3856v1 [physics.atom-ph] (2012).

[Le 70] R. J. Le Roy and R. B. Bernstein, "Dissociation Energy and Long-range Potential of Diatomic Molecules from Vibrational Spacings of Higher Levels", J. Chem. Phys. **52**, 3869 (1970).

[Le 72] Robert J. Le Roy, "Dependence of the Diatomic Rotational Constant B_ν on the Long-Range Internuclear Potential", Canadian Journal of Physics **50**, 953 (1972).

[Le 80a] "Applications of Bohr Quantization in Diatomic Molecule Spectroscopy", edited by M. S. Child, M. S. Child, (1980).

[Le 80b] Robert J. Le Roy, "Theory of deviations from the limiting near-dissociation behavior of diatomic molecules", J. Chem. Phys. **73**, 6003 (1980).

[Lef04] Hélène Lefebvre-Brion and Robert W. Field, *The Spectra and Dynamics of Diatomic Molecules*, (Academic Press, 2004).

[Lim08] Lih-King Lim, C. Morais Smith and Andreas Hemmerich, "Staggered-Vortex Superfluid of Ultracold Bosons in an Optical Lattice", Phys. Rev. Lett. **100**, 130402 (2008).

[Liu01] Y. Liu, J. Lin, G. Huang, Y. Guo and C. Duan, "Simple empirical analytical approximation to the Voigt profile", J. Opt. Soc. Am. B **18**, 666 (2001).

[Mac00] M. Mackie, R. Kowalski and J. Javanainen, "Bose-Stimulated Raman Adiabatic Passage in Photoassociation", Phys. Rev. Lett. **84**, 3803 (2000).

[Mac01] Mette Machholm, Paul S. Julienne and Kalle-Antti Suominen, "Calculations of Collisions Between Cold Alkaline Earth Atoms in a Weak Laser Field", Phys. Rev. A **64**, 033425 (2001).

[Mar09] Y. N. Martinez de Escobar, P. G. Mickelson, M. Yan, B. J. DeSalvo, S. B. Nagel and T. C. Killian, "Bose-Einstein Condensation of ^{84}Sr", Phys. Rev. Lett. **103**, 200402 (2009).

[Mat99] M. R. Matthews, B. P. Anderson, P. C. Haljan, D. S. Hall, M. J. Holland, J. E. Williams, C. E. Wieman and E. A. Cornell, "Watching a Superfluid Untwist Itself: Recurrence of Rabi Oscillations in a Bose-Einstein Condensate", Phys. Rev. Lett. **83**, 3358 (1999).

[Meh03] T. E. Mehlstäubler, J. Keupp, A. Douillet, N. Rehbein, E. M. Rasel and W. Ertmer, "Modelling three-dimensional-quench cooling for alkaline-earth atoms", J. Opt. B: Quantum Semiclass. Opt. **5**, S183 (2003).

[Met99] Harold J. Metcalf and Peter van der Straten, *Laser Cooling and Trapping*, (Springer, New York, Berlin, Heidelberg, 1999) .

[Mey01] Pierre Meystre, *Atom Optics*, (Springer, 2001).

[Mie78] F. H. Mies, W. J. Stevens and M. Krauss, "Model calculation of the electronic structure and spectroscopy of Hg_2", J. Mol. Spec. **72**, 303 (1978).

[Mig85] Alan L. Migdall, John V. Prodan, William D. Phillips, Thomas H. Bergeman and Harold J. Metcalf, "First Observation of Magnetically Trapped Neutral Atoms", Phys. Rev. Lett. **54**, 2596 (1985).

[Mit08] J. Mitroy and J.-Y. Zhang, "Properties and long range interactions of the calcium atom", J. Chem. Phys. **128**, 134305 (2008).

[Mod01] G. Modugno, G. Ferrari, G. Roati, R. J. Brecha, A. Simoni and M. Inguscio, "Bose-Einstein Condensation of Potassium Atoms by Sympathetic Cooling", Science **294**, 1320 (2001).

[Mor96] A. Morinaga, M. Nakamura, T. Kurosu and N. Ito, "Phase shift induced from the dc Stark effect in an atom interferometer comprised of four co-propagating laser beams", Phys. Rev. A **54**, R21 (1996).

[Mér01] Mohammadou Mérawa, Claire Tendero and Michel Rérat, "Excited states dipole polarizabilities of calcium atom and long-range dispersion coefficients for the low-lying electronic states of Ca_2 and CaMg", Chem. Phys. Lett. **343**, 397 (2001).

[Naz06] T. Nazarova, F. Riehle and U. Sterr, "Vibration-insensitive reference cavity for an ultra-narrow-linewidth laser", Appl. Phys. B **83**, 531 (2006).

[Naz07] Tatiana Nazarova, *Towards the Quantum Noise Limit in Ramsey-Bordé Atom Interferometry*, PhD thesis Gottfried Wilhelm Leibniz Universität Hannover (2007) Online available at http://www.tib.uni-hannover.de.

[Nie99] Esben Nielsen and J. H. Macek, "Low-Energy Recombination of Identical Bosons by Three-Body Collisions", Phys. Rev. Lett. **83**, 1566 (1999).

[Oli77] J. J. Olivero and R. L. Lonbothum, "Empirical fits to the Voigt line width: a brief review", J. Quant. Spectrosc. Radiat. Transfer **17**, 233 (1977).

[Osp10] S. Ospelkaus, K.-K. Ni, D. Wang, M. H. G. de Miranda, B. Neyenhuis, G. Quéméner P. S. Julienne, J. L. Bohn, D. S. Jin and J. Ye, "Quantum-State Controlled Chemical Reactions of Ultracold Potassium-Rubidium Molecules", Science **327**, 853 (2010).

[Pit61] L. P. Pitaevskii, "Vortex Lines in an Imperfect Bose Gas", Soviet Physics JETP **13**, 451 (1961).

[Raa87] E. L. Raab, M. Prentiss, A. Cable, S. Chu and D. E. Pritchard, "Trapping of Neutral Sodium Atoms with Radiation Pressure", Phys. Rev. Lett. **59**, 2631 (1987).

[Raa08] P. Raab and H. Friedrich, "Quantization function for deep potentials with attractive tails", Phys. Rev. A **78**, 022707 (2008).

[Rob01] A. Robert, O. Sirjean, A. Browaeys, J. Poupard, S. Nowak, D. Boiron, C. I. Westbrook and A. Aspect, "A Bose-Einstein Condensate of Metastable Atoms", Science **292**, 461 (2001).

[Sta98] D. M. Stamper-Kurn, M. R. Andrews, A. P. Chikkatur, S. Inouye, H.-J. Miesner, J. Stenger and W. Ketterle, "Optical Confinement of a Bose-Einstein Condensate", Phys. Rev. Lett. **80**, 2027 (1998).

[Ste09] Simon Stellmer, Meng Khoon Tey, Bo Huang, Rudolf Grimm and Florian Schreck, "Bose-Einstein Condensation of Strontium", Phys. Rev. Lett. **103**, 200401 (2009).

[Ste13] Simon Stellmer, Benjamin Pasquiou, Rudolf Grimm and Florian Schreck, "Laser cooling to quantum degeneracy", arXiv:1301.4776v1 [cond-mat.quant-gas] (2013).

[Sug11] Seiji Sugawa, Rekishu Yamazaki, Shintaro Taie and Yoshiro Takahashi, "Bose-Einstein condensate in gases of rare atomic species", Phys. Rev. A **84**, 011610(R) (2011).

[Tak03] Yosuke Takasu, Kenichi Maki, Kaduki Komori, Tetsushi Takano, Kazuhito Honda, Mitsutaka Kumakura, Tsutomu Yabuzaki and Yoshiro Takahashi, "Spin-Singlet Bose–Einstein Condensation of Two-Electron Atoms", Phys. Rev. Lett. **91**, 040404 (2003).

[Tak06] Masao Takamoto, Feng-Lei Hong, Ryoichi Higashi, Yasuhisa Fujii, Michito Imae and Hidetoshi Katori, "Improved Frequency Measurement of a One-Dimensional Optical Lattice Clock with a Spin-Polarized Fermionic ^{87}Sr Isotope", J. Phys. Soc. Jap. **75**, 104302 (2006).

[The04] M. Theis, G. Thalhammer, K. Winkler, M. Hellwig, G. Ruff, R. Grimm and J. Hecker Denschlag, "Tuning the Scattering Length with an Optically Induced Feshbach Resonance", Phys. Rev. Lett. **93**, 123001 (2004).

[Tho87] H. R. Thorsheim, J. Weiner and P. S. Julienne, "Laser-Induced Photoassociation of Ultracold Sodium Atoms", Phys. Rev. Lett. **58**, 2420 (1987).

[Toj06] Satoshi Tojo, Masaaki Kitagawa, Katsunari Enomoto, Yutaka Kato, Yosuke Takasu, Mitsutaka Kumakura and Yoshiro Takahashi, "High-Resolution Photoassociation Spectroscopy of Ultracold Ytterbium Atoms by Using the Intercombination Transition", Phys. Rev. Lett. **96**, 153201 (2006).

[Tol37] John Ronald Reuel Tolkien, *The Hobbit, or There and Back Again*, (George Allen and Unwin, 1937).

[Tro97] J. Trost and H. Friedrich, "WKB and exact wave functions for inverse power-law potentials", Phys. Rev. A **228**, 127 (1997).

[Ves74] L. Veseth and A. Lofthus, "Rotational energies of Hund's case (c) $^3\Pi$ states in diatomic molecules: The a$^3\Pi$ state of InH and InD", J. Mol. Spec. **49**, 414 (1974).

[Vog07] F. Vogt, Ch. Grain, T. Nazarova, U. Sterr, F. Riehle, Ch. Lisdat and E. Tiemann, "Determination of the calcium ground state scattering length by photoassociation spectroscopy at large detunings", Eur. Phys. J. D **44**, 73 (2007) highlight paper.

[Vog09] Felix Vogt, *Creation of cold and dense ensembles of calcium atoms*, PhD thesis Gottfried Wilhelm Leibniz Universität Hannover (2009) Online available at http://www.tib.uni-hannover.de.

[Web03a] Tino Weber, Jens Herbig, Michael Mark, Hanns-Christoph Nägerl and Rudolf Grimm, "Bose–Einstein Condensation of Cesium", Science **299**, 232 (2003).

[Web03b] Tino Weber, Jens Herbig, Michael Mark, Hanns-Christoph Nägerl and Rudolf Grimm, "Three-Body Recombination at Large Scattering Lengths in an Ultracold Atomic Gas", Phys. Rev. Lett. **91**, 123201 (2003).

[Wen26] Gregor Wentzel, "Eine Verallgemeinerung der Quantenbedingungen für die Zwecke der Wellenmechanik", Zeitschrift für Physik A Hadrons and Nuclei **38**, 518 (1926).

[Wil01] Guido Wilpers, Tomas Binnewies, Carsten Degenhardt, Uwe Sterr, Jürgen Helmcke and Fritz Riehle, "An Optical Frequency Standard with Cold Calcium Atoms", Annales Françaises des Microtechniques et de Chronométrie **50**, 15 (2001).

[Xu03] Xinye Xu, Thomas H. Loftus, John L. Hall, Allan Gallagher and Jun Ye, "Cooling and trapping of atomic strontium", J. Opt. Soc. Am. B **20**, 968 (2003).

[Yam10] Rekishu Yamazaki, Shintaro Taie, Seiji Sugawa and Yoshiro Takahashi, "Submicron scale spatial modulation of an interatomic interaction in a Bose-Einstein condensate", Phys. Rev. Lett. **105**, 050405 (2010).

[Yan02] S. Yanagimachi, M. Kajiro, M. Machiya and A. Morinaga, "Direct measurement of the Aharonov-Casher phase and tensor Stark polarizability using a calcium atomic polarization interferometer", Phys. Rev. A **65**, 042104 (2002).

[Yan07] C. Y. Yang, P. Halder, O. Appel, D. Hansen and A. Hemmerich, "Continuous loading of $^1S_0$ calcium atoms into an optical dipole trap", Phys. Rev. A **76**, 033418 (2007).

[Yan13] Mi Yan, B. J. DeSalvo, B. Ramachandhran, H. Pu and T. C. Killian, "Controlling Condensate Collapse and Expansion with an Optical Feshbach Resonance", Phys. Rev. Lett. **110**, 123201 (2013).

[Zel06] T. Zelevinsky, M. M. Boyd, A. D. Ludlow, T. Ido, J. Ye, R. Ciuryło, P. Naidon and P. S. Julienne, "Narrow Line Photoassociation in an Optical Lattice", Phys. Rev. Lett. **96**, 203201 (2006).

[Zin00] G. Zinner, T. Binnewies, F. Riehle and E. Tiemann, "Photoassociation of cold Ca atoms", Phys. Rev. Lett. **85**, 2292 (2000).

Lebenslauf

Oliver Appel
geboren am 12.11.1982 in Holzminden

Bildungsweg

08/1989 – 07/1993	Grundschule Sollingstraße Holzminden
08/1993 – 07/1995	Orientierungsstufe Liebigstraße Holzminden
08/1995 – 06/2002	Campe-Gymnasium Holzminden
10/2002 – 01/2008	Studium der Physik an der Universität Hamburg Vordiplom erhalten am 30.9.2004 Diplom erhalten am 31.1.2008 Thema der Diplomarbeit: *Charakterisierung einer magneto-optischen Falle für metastabile Kalziumatome*

Beruflicher Werdegang

9/2002	Aushilfskraft bei Dragoco Gerberding & Co. AG, Holzminden in der Abteilung Forschung / Physikalische Chemie
11/2005 – 10/2006	studentische Hilfskraft, Universität Hamburg Arbeitsgruppe Sengstock, Quantengase und Spektroskopie
07/2008 – 06/2012	wissenschaftlicher Mitarbeiter mit dem Ziel der Promotion PTB Braunschweig, Arbeitsgruppe Quantenoptik mit kalten Atomen

Publikationsliste

- C. Y. Yang, P. Halder, O. Appel, D. Hansen und A. Hemmerich, *Continuous loading of $^1S_0$ calcium atoms into an optical dipole trap*, Phys. Rev. A **76**, 033418 (2007)
- S. Kraft, F. Vogt, O. Appel, F. Riehle und U. Sterr, *Bose-Einstein condensation of alkaline earth atoms: ^{40}Ca*, Phys. Rev. Lett. **103**, 130401 (2009)
- M. Kahmann, E. Tiemann, O. Appel, U. Sterr und F. Riehle, *High accuracy photoassociation of ^{40}Ca near the $^3P_1 + {}^1S_0$ asymptote and its Zeeman effect*, arXiv:1306.6473 [physics.atom-ph] (2013), eingereicht bei Phys. Rev. Lett.

Konferenzbeiträge

- C.-Y. Yang, P. Halder, O. Appel, D. Hansen und A. Hemmerich, *Continuous Loading of a Calcium Dipole Trap*, Poster, DPG Frühjahrstagung der Sektion AMOP, Düsseldorf (2007)
- O. Appel, F. Vogt, U. Sterr und F. Riehle, *Towards Bose-Einstein-Condensation of Calcium*, Poster, 17. Norddeutscher Lasertag, Hannover (2008)
- O. Appel, F. Vogt, U. Sterr und F. Riehle, *Auf dem Weg zum Calcium-BEC*, Vortrag, DPG Frühjahrstagung der Sektion AMOP, Hamburg (2009)
- S. Kraft, O. Appel, F. Vogt, F. Riehle und U. Sterr, *Bose-Einstein condensation of alkaline earth atoms: ^{40}Ca*, Vortrag, 18th International Laser Physics Workshop, Barcelona (2009)
- U. Sterr, S. Kraft, F. Vogt und O. Appel, *Ultracold earth alkaline atoms for optical clocks and BECs*, Eingeladener Vortrag, JILA Boulder (2009)
- S. Kraft, O. Appel, F. Vogt, U. Sterr und F. Riehle, *BEC of alkaline earth atoms: ^{40}Ca*, Vortrag, BEC 2009, San Feliu de Guixols (2009)
- S. Kraft, O. Appel, F. Vogt, F. Riehle und U. Sterr, *Bose-Einstein condensation of alkaline earth atoms: ^{40}Ca*, Vortrag, Alkaline Earth Workshop, University of Maryland, Washington (2009)
- O. Appel, F. Vogt, S. Kraft, U. Sterr und F. Riehle, *Bose-Einstein-Condensation of Calcium*, Poster, QUEST@PTB Seminar, Braunschweig (2009)

- S. Kraft, O. Appel, F. Vogt, U. Sterr und F. Riehle, *BEC of alkaline earth atoms: ^{40}Ca*, Vortrag, SFB/TRR 21 - Seminar, Universität Tübingen (2009)

- F. Vogt, O. Appel, S. Kraft, F. Riehle und U. Sterr, *Collisional properties of ^{40}Ca atoms*, Poster, DPG Frühjahrstagung der Sektion AMOP, Hannover (2010)

- S. Kraft, F. Vogt, O. Appel, F. Riehle und U. Sterr, *Bose-Einstein condensation of alkaline earth atoms: ^{40}Ca*, Vortrag, DPG Frühjahrstagung der Sektion AMOP, Hannover (2010)

- U. Sterr, Ch. Lisdat, J. S. R. Vellore Winfred, S. Falke, T. Middelmann, S. Kraft, F. Vogt, O. Appel und F. Riehle, *Precision Measurements with Ultracold Earth Alkaline Atoms*, Vortrag, Frontiers of Matter Wave Optics, Kreta (2010)

- S. Kraft, O. Appel, F. Vogt. S. Schulz, U. Sterr und F. Riehle, *A BEC made of Calcium*, Vortrag, QUEST Symposium Precision Matter Wave Optics, Hannover (2010)

- S. Kraft, F. Vogt, O. Appel, S. Schulz, M. Kahmann, U. Sterr und F. Riehle, *A Bose-Einstein Condensate of Calcium*, Poster, 22nd International Conference on Atomic Physics, Cairns (2010)

- M. Kahmann, S. Kraft, O. Appel, S. Schulz, F. Riehle und U. Sterr, *Using the metastable $^3P_0$-state in a BEC of ^{40}Ca*, Poster, École Prédoctorale de Physique des Houches (2010)

- S. Kraft, O. Appel, S. Schulz, M. Kahmann, F. Riehle und U. Sterr, *A Bose-Einstein Condensate of ^{40}Ca*, Poster, EMALI Conference Barcelona (2010)

- M. Kahmann, S. Kraft, O. Appel, S. Schulz, F. Riehle und U. Sterr, *Using the metastable $^3P_0$-state in a BEC of ^{40}Ca*, Poster, Young Atom Opticians Conference, Hannover (2011)

- O. Appel, M. Kahmann, S. Schulz, S. Kraft, F. Riehle und U. Sterr, *Investigation of light-assisted collisions of ^{40}Ca*, Poster, DPG Frühjahrstagung der Sektion AMOP, Dresden (2011)

- O. Appel, M. Kahmann, S. Schulz, S. Kraft, F. Riehle und U. Sterr, *Investigation of light-assisted collisions of ^{40}Ca*, Poster, DPG Physics School 2011: Quantum Gases in Dilute Atomic Vapour, Bad Honnef (2011)

- S. Kraft, O. Appel, M. Kahmann, S. Schulz, F. Riehle und U. Sterr, *The Calcium BEC at PTB*, Poster, 20th International Conference on Laser Spectroscopy, Aerzen (2011)

- S. Kraft, O. Appel, M. Kahmann, S. Schulz, F. Riehle und U. Sterr, *A quantum gas of ^{40}Ca*, Poster, BEC 2011, San Feliu de Guixols (2011)

- M. Kahmann, O. Appel, S. Kraft, F. Riehle und U. Sterr, *Photoassociation with ^{40}Ca*, Vortrag, Seminar Physikalisches Institut der Universität Tübingen, Oberjoch (2012)
- M. Kahmann, O. Appel, F. Riehle und U. Sterr, *Optical Feshbach Resonances with ^{40}Ca*, Vortrag, Research Training Group 1729, Hannover (2012)
- M. Kahmann, O. Appel, S. Kraft, D. Le Plat, F. Riehle und U. Sterr, *Enhanced Loading for Ultracold Calcium Atoms and Photoassociation at the $^1S_0 - {}^3P_1$ Asymptote*, Poster, DPG Frühjahrstagung der Sektion AMOP, Stuttgart (2012)
- M. Kahmann, O. Appel, F. Riehle und U. Sterr, *Photoassociation of Ultracold Calcium at the $^1S_0 - {}^3P_1$ Asymptote*, Poster, QUEST Convention, Hannover (2012)
- M. Kahmann, O. Appel, F. Riehle und U. Sterr, *Photoassociation at the $^1S_0 - {}^3P_1$ Asymptote*, Poster, 5th International Workshop on Ultracold Group II Atoms, Tokyo (2012)
- M. Kahmann, O. Appel, E. Pachomow, F. Riehle und U. Sterr, *Optical Feshbach Resonances with ^{40}Ca*, Vortrag, Seminar für Molekülphysik der Universität Hannover (2013)
- M. Kahmann, O. Appel, E. Pachomow, F. Riehle und U. Sterr, *Enhanced magneto-optical trapping by storing atoms in a dark triplet state*, Vortrag, Workshop Research Training Group 1729, Goslar (2013)
- M. Kahmann, O. Appel, E. Tiemann, F. Riehle und U. Sterr, *Optical Feshbach Resonances with ^{40}Ca*, Vortrag, Seminar Physikalisches Institut der Universität Tübingen, Oberjoch (2013)
- M. Kahmann, O. Appel, E. Tiemann, F. Riehle und U. Sterr, *Optical Feshbach Resonances with ^{40}Ca*, Vortrag, DPG Frühjahrstagung der Sektion AMOP, Hannover (2013)
- E. Pachomow, M. Kahmann, O. Appel, F. Riehle, U. Sterr und E. Tiemann, *Photoassociation of Ultracold Calcium at the $^1S_0 - {}^3P_1$ Asymptote*, Poster, Young Atom Opticians Conference, Birmingham (2013)
- U. Sterr, M. Kahmann, O. Appel, E. Tiemann und F. Riehle, *Photoassociation of Ultracold Calcium at the $^1S_0 - {}^3P_1$ Asymptote*, Poster, 21th International Conference on Laser Spectroscopy, Berkeley (2013)
- F. Riehle, M. Kahmann, O. Appel, U. Sterr und E. Tiemann, *Photoassociation spectroscopy of cold ^{40}Ca near the $^1S_0 - {}^3P_1$ asymptote*, Eingeladener Vortrag, 6-th International Symposium on Modern Problems of Laser Physics, Novosibirsk (2013)

Danksagung

Ich danke allen, die zum Gelingen dieser Arbeit beigetragen haben.
Insbesondere bedanken möchte ich mich bei

- meinen Eltern Annegret und Alfred Appel, deren Erziehung Neugier, Wissensdurst und selbständiges Denken begünstigt hat. Desweiteren danke ich ihnen für die stete Unterstützung während meines Studiums und meiner Doktorarbeit.
- Herrn Dir. und Prof. Dr. Fritz Riehle und Herrn Dr. Uwe Sterr für die Betreuung und theoretische sowie experimentelle Unterstützung dieser Arbeit.
- Herrn Prof. Dr. Wolfgang Ertmer für die Betreuung dieser Arbeit von Seiten der Universität Hannover sowie ihm und Herrn Prof. Dr. Ernst Rasel für die Leihgabe des Yb:YAG-Scheibenlasers.
- Herrn Dr. Felix Vogt, Herrn Dr. Sebastian Kraft und Herrn Dipl.-Phys. Max Kahmann für die angenehme Zusammenarbeit im Labor.
- Herrn Dr. Stephan Falke und Herrn Prof. Dr. Eberhard Tiemann für viele Lehrstunden und Diskussionsrunden über Molekülphysik.
- Frau Dr. Purbasha Halder für hilfreiche Diskussionen über die Eigenschaften von Calcium.
- Frau Dr. Gesine Grosche und Herrn Dr. Thomas Middelmann für viele allgemeine Diskussionen über diverse Aspekte des Experiments.
- Herrn Dipl.-Ing. Mattias Misera, Herrn Andre Uhde, Herrn Jörn Falke und Herrn Klemens Budin für die technische Unterstützung des Experiments.